HZDR-034

EXPERIMENTAL STUDY OF THE $^{22}Ne(p,\gamma)^{23}Na$ REACTION AND ITS IMPLICATIONS FOR NOVAE SCENARIOS

Marie-Luise Menzel

Wissenschaftlich-Technische Berichte
HZDR-034 · ISSN 2191-8708

WISSENSCHAFTLICH-
TECHNISCHE BERICHTE

HZDR
HELMHOLTZ
ZENTRUM DRESDEN
ROSSENDORF

Wissenschaftlich-Technische Berichte
HZDR-034

Marie-Luise Menzel

EXPERIMENTAL STUDY OF THE $^{22}NE(p,\gamma)^{23}NA$ REACTION AND ITS IMPLICATIONS FOR NOVAE SCENARIOS

HZDR

HELMHOLTZ
ZENTRUM DRESDEN
ROSSENDORF

TECHNISCHE UNIVERSITÄT DRESDEN

Experimental Study of the ^{22}Ne(p,γ)^{23}Na Reaction and its Implications for Novae Scenarios

Diplomarbeit zur Erlangung des wissenschaftlichen Grades
Diplom-Physiker

vorgelegt von

Marie-Luise Menzel

Matrikelnummer: 3294979

Institut für Kern- und Teilchenphysik
Technische Universität Dresden

Erster Gutachter: **Prof. Kai Zuber**
Institut für Kern- und Teilchenphysik, Lehrstuhl für Kernphysik
Technische Universität Dresden

Zweiter Gutachter: **PD Dr. Daniel Bemmerer**
Institut für Strahlenphysik, Abteilung Kernphysik
Helmholtz-Zentrum Dresden-Rossendorf

eingereicht in Dresden, 20.12.2012
Version 11.4.2013

Für Waldemar und Torsten.
Danke.

Abstract

The ^{22}Ne(p,γ)^{23}Na reaction belongs to the catalytic neon-sodium cycle and has an important role in the explosive hydrogen burning. The neon-sodium cycle takes place at temperatures of $T = 0.1 - 0.5\,\mathrm{GK}$ and is assumed to occur in different astrophysical systems: e.g. in novae, in super novae of type Ia and during the shell-burning of red giant branch stars.

The implications of ^{22}Ne(p,γ)^{23}Na and the neon-sodium cycle in a nova scenario have been studied by using the nuclear network code libnucnet at GSI in Darmstadt. A nova is an outburst of matter in a binary system consisting of a white dwarf and a red giant star. It is therefore a representative phenomenon for explosive hydrogen burning. For the calculation of the nucleosynthesis during the nova outburst, the code libnucnet requires the initial mass composition of the novae partners, the temperature and density profiles of the nova explosion and the thermonuclear reaction rates of the participating reactions. In the following, the code determined the flow and the final atomic abundance in the neon-sodium cycle during the entire nova process. Additionally, the influence of the temperature profile of the novae outburst as well as the thermonuclear reaction rate of the ^{22}Ne(p,γ)^{23}Na reaction on the final atomic abundance in the outburst has been studied.

A characteristic measure for the reactions in astrophysical environments is the thermonuclear reaction rate. The reaction rate of ^{22}Ne(p,γ)^{23}Na has still strong uncertainties in the temperature range of $T = 0.03 - 0.3\,\mathrm{GK}$. These uncertainties are based on insufficient upper limits of the resonance strengths as well as the possible existence of tentative states that are populated in the energy range of $E_p^{lab} = 30 - 300\,\mathrm{keV}$.

The research presented in this thesis is dedicated to the experimental study of the ^{22}Ne(p,γ)^{23}Na reaction for an improved determination of the thermonuclear reaction rate. Furthermore, the implications of ^{22}Ne(p,γ)^{23}Na and the neon-sodium-cycle in novae scenarios are discussed.

The data taking has been performed at the Laboratori Nazionali del Gran Sasso, Italy. This laboratory provides the LUNA facility (Laboratory for Underground Nuclear Astrophysics) for the measurement of small reaction cross sections. The LUNA facility includes a 400 kV ion accelerator, a windowless gas target system and a HPGe-detector. Based on the measurements of the ^{22}Ne(p,γ)^{23}Na reaction at LUNA, upper limits for the strengths of five isolated resonances in the energy range of $E_p^{lab} = 150 - 340\,\mathrm{keV}$ have been determined. For the nuclear resonance at $E_{res}^{lab} = 186\,\mathrm{keV}$, a positive resonance strength has been measured for the first time in literature.

Abstrakt

Diese Diplomarbeit umfasst die ^{22}Ne(p,γ)^{23}Na Reaktion, die ein wichtiger Teilprozess für das explosive Wasserstoff-Brennen ist. Die betrachtete Kernreaktion wird dem Neon-Natrium Zyklus zugeordnet und läuft in einem Temperaturregime von $T = 0.1 - 0.5\,\mathrm{GK}$ ab. Der Neon-Natrium Zyklus tritt in verschiedenen astrophysikalischen Prozessen auf, wie z.B. in Novae, in Supernovae (Typ Ia) und während des Schalen-Brennens in Roten Riesen.

Mit Hilfe eines nuklearen Netzwerk-Codes kann die Auswirkung von ^{22}Ne(p,γ)^{23}Na auf den Neon-Natrium Zyklus in einem Nova-Szenario analysiert werden. Die Netzwerkberechnung wurde mit dem libnucnet Code an der GSI in Darmstadt durchgeführt. Eine Nova ist ein explosiver Materieaustoß in einem Doppelsternsystem bestehend aus einem weißen Zwerg und einem roten Riesen. Dieses astrophysikalische Phänomen ist repräsentativ für das explosive Wasserstoff-Brennen. Für die Berechnung der Nukleosynthese während der Nova benötigt der libucnet code die Anfangsmassenverteilung des Doppelstern-Systems, den Temperatur- und Druckverlauf im Nova-Ausstoß und die thermonuklearen Reaktionsraten der teilnehmenden Reaktionen. Basierend auf diesen Vorraussetzungen wurde der Fluss und die finale atomare Massenverteilung im Neon-Natrium Zyklus während der Nova-Explosion berechnet. Zusätzlich wurde der Einfluss des Nova-Temperaturverlaufs und der thermonuklearen Reaktionsrate von ^{22}Ne(p,γ)^{23}Na betrachtet.

Die thermonukleare Reaktionsrate ist eine charakteristische Messgröße für astrophysikalische Szenarien. Für die Reaktionsrate von ^{22}Ne(p,γ)^{23}Na bestehen noch große Unsicherheiten im Temperaturbereich von $T = 0.03{-}0.3\,\mathrm{GK}$. Diese Unsicherheiten basieren auf den Resonanzstärken, von denen bisher nur oberen Schranken bekannt sind, und auf der bisher vermuteten Existenz weiterer Resonanzen im Energiebereich von $E_p^{lab} = 30 - 300\,\mathrm{keV}$.

Die vorgestellte Forschungsarbeit umfasst die experimentelle Untersuchung der ^{22}Ne(p,γ)^{23}Na Reaktion, um eine verbesserte Bestimmung der thermonuklearen Reaktionsrate zu erlangen. Des Weiteren werden deren Auswirkungen auf die Nukleosynthese in Novae-Szenarien analysiert.

Die experimentelle Datennahme wurde am Laboratori Nazionali del Gran Sasso, Italien durchgeführt. In diesem Labor steht LUNA (Laboratory for Underground Nuclear Astrophysics) für die Forschung an Kernreaktionen mit sehr kleinem Wechselwirkungsquerschnitt zur Verfügung. LUNA besteht aus einen 400 kV Ionen-Beschleuniger, einem fensterlosen Gastarget und einem HPGe-Detektor. Basierend auf den LUNA-Messungen der ^{22}Ne(p,γ)^{23}Na Reaktion konnten fünf isolierte Resonanzen im Energiebereich von $E_p^{lab} = 150 - 340\,\mathrm{keV}$ bestimmt werden. Für die Kernresonanz bei $E_{res}^{lab} = 186\,\mathrm{keV}$ wurde in der Literatur erstmalig eine positive Resonanzstärke berechnet.

Contents

1. General Introduction

In a first place, the neon-sodium cycle and its participating reactions are introduced. Their physical properties e.g. the Q-value and the half-life as well as the reaction rates are presented.

In the following, a special focus is set on the ^{22}Ne(p,γ)^{23}Na reaction, which is the centre of interest in this diploma project. Its energy level diagram with measured and tentative states is shown. Furthermore, the resonance strengths of ^{22}Ne(p,γ)^{23}Na, which have been obtained in former experiments are presented.

A nova outburst is a representative astrophysical phenomenon for the explosive hydrogen burning and the presence of the neon-sodium cycle. The initiation of a novae and the observational parameters e.g. luminosity are explained. Furthermore, the contribution of a novae explosion to the galactic abundance of elements is calculated.

The last paragraph focuses on the theoretical description of nuclear interactions of particles in using the compound nucleus model and a quantum mechanical description. In the following, the important nuclear physics parameters like cross-section, resonance strength and S-factor are introduced.

1.1. The Neon-Sodium-Cycle

In very hot astrophysical conditions, explosive hydrogen-burning induces many nuclear reactions cycles. Subsequent to the Bethe-Weizsäcker-cycle and the CNO-cycle is the neon-sodium-cycle which runs at higher temperatures. This cycle involves neon and sodium nuclides originating from the stable valley of medium mass elements in the nuclide chart. Because of the relatively high Coulomb barrier of the participating reaction partners, the cycle does not contribute significantly to the energy production in stars. Nevertheless, its contribution is important for nucleosynthesis of neon and sodium isotopes.

The neon-sodium-cycle is fed amongst others by the leakage products of the CNO burning phase at high temperatures. It is a catalytic cycle producing sodium isotopes by proton capture on existing neon isotopes. During this process, oxygen is transformed into other CNO nuclei ([14]). The participating neon and sodium nuclides are the fundamental elements for the production of heavier nuclei via (p,γ)- and (α,n)-reactions [13].

The isotopes in the neon-sodium-cycle interact by proton capture, β^+-decay and electron capture (EC) decay. Their reverse reaction from ^{23}Na to ^{20}Ne proceeds via a (p,α)-reaction. The total reaction equation is presented in the following, assuming the predominant β^+-decays:

$$^{20}Ne(p,\gamma)^{21}Na(e^+\nu)^{21}Ne(p,\gamma)^{22}Na(e^+\nu)^{22}Ne(p,\gamma)^{23}Na(p,\alpha)^{20}Ne.$$

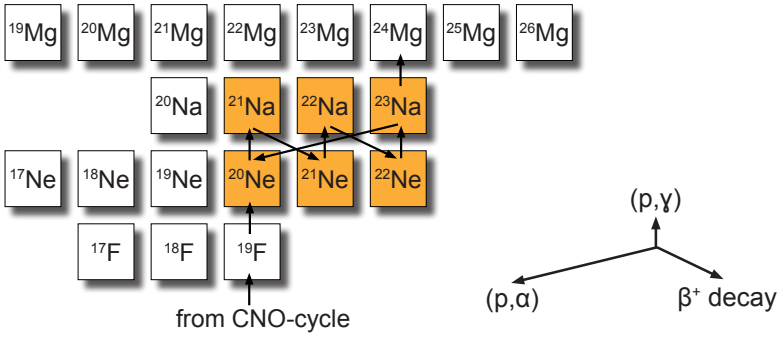

Figure 1.1.: Reactions taking place within the neon-sodium-cycle.

Reaction	Q-Value
^{20}Ne(p,γ)^{21}Na	(2431.2 ± 0.7) keV
^{21}Ne(p,γ)^{22}Na	(6739.63 ± 0.42) keV
^{22}Ne(p,γ)^{23}Na	(8794.11 ± 0.02) keV

Reaction	Terrestrial Half-life $t_{1/2}$
^{21}Na$(e^+\nu)^{21}$Ne	(22.49 ± 0.04) s
^{22}Na$(e^+\nu)^{22}$Ne	(2.6027 ± 0.001) yr

Table 1.1.: Characteristic physics parameters of the reactions in the neon-sodium-cycle [5], [6], [7].

In Table 1.1, the Q-values [5] (see paragraph 1.4.1) of the reactions belonging to the neon-sodium-cycle are listed. According to their high Q-value, the neon isotopes release a lot of energy during the (p,γ) process. The ^{22}Ne(p,γ)^{23}Na reaction contributes most to the energy release per proton capture.

The unstable sodium isotopes ^{21}Na and ^{22}Na pass via β^+-decay and electron capture decay to neon isotopes. The half-lives of the decaying sodium isotopes inside the cycle differ by a factor of $\sim 4 \cdot 10^6$ (see Table 1.1, [6, 7]). The β^+-decay and the electron capture decay of ^{22}Na with $t_{1/2} = 22.49\,\mathrm{s}$ is more favorable than the decay of ^{21}Na with $t_{1/2} = 2.6\,\mathrm{yr}$.

In Figure 1.2, one can see the thermonuclear reaction rates of the participating nuclear reactions of the neon-sodium-cycle in the temperature region of $T = 0.1 - 0.5\,\mathrm{GK}$. These rates are based on Monte-Carlo simulations of Iliadis et al. [17]. The proton capture process of ^{21}Ne has the strongest reaction rate. Furthermore, the rates of ^{23}Na(p,γ) and ^{23}Na(p,α) are competing. The rates of the proton capture processes of ^{22}Ne and ^{21}Ne are comparably weak. In the displayed temperature region, the thermonuclear reaction rates increase by a factor of $f \sim 10^6$.

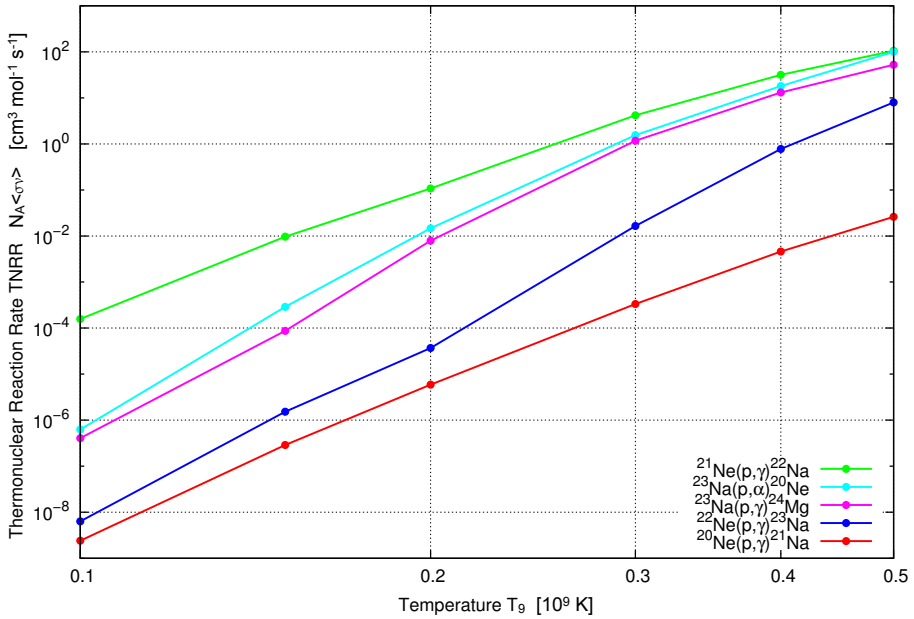

Figure 1.2.: Thermonuclear reaction rates for important reactions in the neon-sodium-cycle [17].

The temperature region of $T = 0.1 - 0.5\,\mathrm{GK}$ corresponds to the conditions occurring during novae eruptions. Paragraph 1.3 is dedicated to the astrophysical explanation of novae processes.

1.2. The Reaction ^{22}Ne(p,γ)^{23}Na

Because of its strong impact on the neon-sodium-cycle, the reaction ^{22}Ne(p,γ)^{23}Na has often been investigated. The resonance levels $E > 400\,\text{keV}$ have already been measured directly. But most of the resonances in the energy range of $E = 0 - 400\,\text{keV}$ are still determined by upper limits for the resonance strengths. Additionally, several resonances are considered as tentative. This leads to large uncertainties for the thermonuclear reaction rates (TNRR; see paragraph 1.4.6) in the corresponding temperature range.

1.2.1. Impact of Resonances of ^{22}Ne(p,γ)^{23}Na

In Figure 1.3, the energy level diagram for the ^{22}Ne(p,γ)^{23}Na reaction [8] is presented. The resonance at $E_x = 9147\,\text{keV}$ has been taken from [14]. The left part of the figure describes the energy of the incoming proton in the center-of-mass and the laboratory reference frames. The right side presents the energy levels with the spin characteristics of ^{23}Na. The sum of the center-of-mass energy of the proton E_{cm} and the Q-value Q of the observed reaction corresponds to the level energy E_x of ^{23}Na:

$$E_x = E_{cm} + Q. \tag{1.1}$$

The setup of the LUNA experiment allows for the measurement of the resonances with a proton beam in the energy range of $E = 50 - 400\,\text{keV}$. Based on the dataset of the LUNA measurements, five resonances of ^{23}Na have been in the center of interest. The energy level diagram in Figure 1.3 shows the selected resonances at $E_x = 9113\,\text{keV}$, $9103\,\text{keV}$, $9038.7\,\text{keV}$, $8972\,\text{keV}$ and $8946\,\text{keV}$.

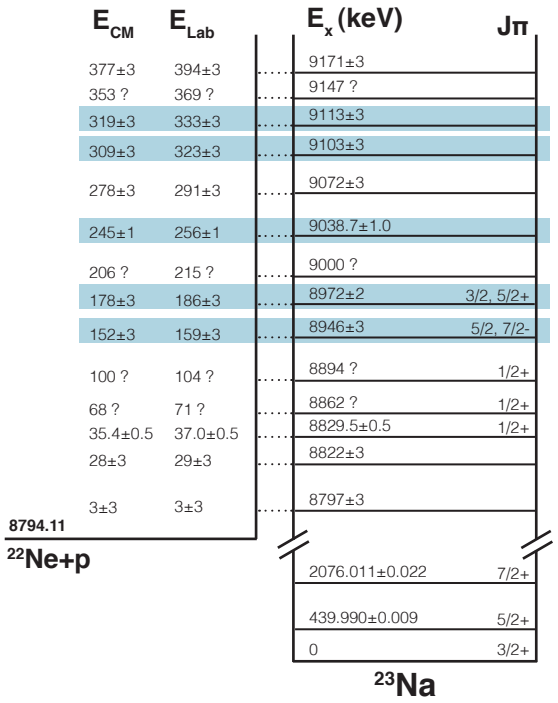

Figure 1.3.: Energy level diagram for the ^{22}Ne(p,γ)^{23}Na [8] with $E_x = 9147\,\text{keV}$ from [14].

In Figure 1.4, the influence of the most important resonances of ^{22}Ne(p,γ)^{23}Na on the thermonuclear reaction rate [14] are presented. The resonances $E_{lab} = 104 - 215\,\text{keV}$ dominate the TNRR in the temperature region of $T = 0.08 - 0.26\,\text{GK}$. The resonances for $E_{lab} = 256\,\text{keV}$, $291\,\text{keV}$, $323\,\text{keV}$, $333\,\text{keV}$, $369\,\text{keV}$ and $394\,\text{keV}$ have a negligible contribution and are not plotted in this figure. The resonances $E_{res} = 71, 215, 104\,\text{keV}$ are assumed to be tentative.

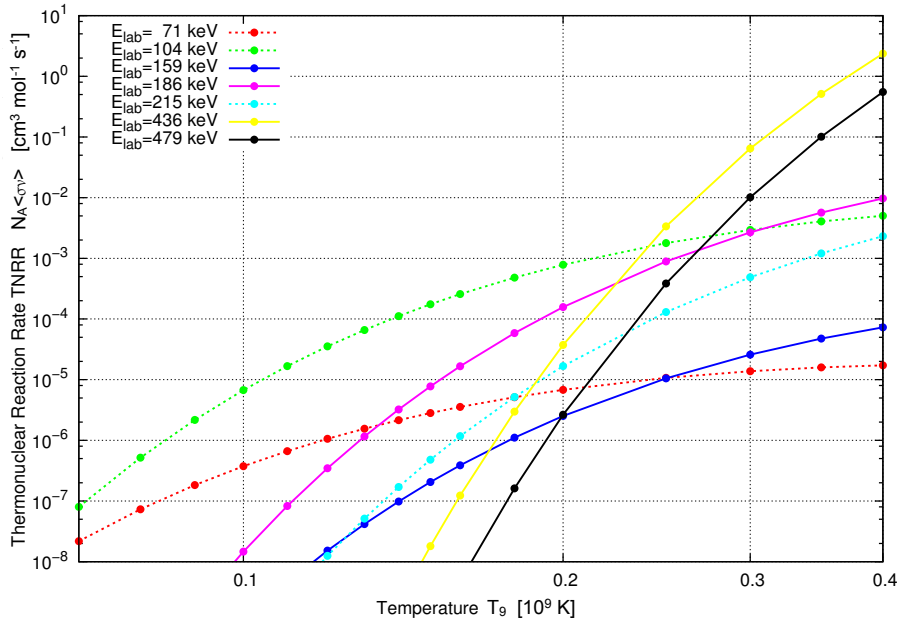

Figure 1.4.: Thermonuclear reaction rate of ^{22}Ne(p,γ)^{23}Na with the contribution of most important resonances [14]. The dashed lines designate tentative resonances.

1.2.2. Gamma-Ray Transitions

The probability of γ-ray transitions between the energy levels in nuclei depend on the characteristic quantum numbers of the energetic levels, e.g. the parity π and the total angular momentum J.

During the measurements at LUNA, only γ-ray transitions between low energy levels have been observed. The following γ-ray transitions have been in the center of interest [8]:

- $E_\gamma = 440\,\text{keV}$: 1^{st} excited state ($E_x = 440\,\text{keV}$) $\rightarrow$ ground state ($E_x = 0\,\text{keV}$)
- $E_\gamma = 1636\,\text{keV}$: 2^{nd} excited state ($E_x = 2076\,\text{keV}$) $\rightarrow$ 1^{st} excited state ($E_x = 440\,\text{keV}$)

1.2.3. Previous Measurements

The ^{22}Ne(p,γ)^{23}Na reaction has already been studied in previous experiments. Table 1.2 lists the resonance strengths which have been published by the research groups of Görres et al. (1982 and 1983) [13] [11], Hale et al. (2001) [14] and in the compilation of Iliadis et al. (2010) [17]. In the following paragraphs, further details of the measurement setups and the results of these former studies for the ^{22}Ne(p,γ)^{23}Na reaction are explained.

Energy Level	**Resonance Energy**		**Resonance Strength** $\omega\gamma$ (eV)		
E_x (keV)	E_{res}^{cm} (keV)	E_{res}^{lab} (keV)	Görres 83	Hale 01	Iliadis 10
8862	68	71	($\leq$4.2·10^{-9})	($\leq$1.9·10^{-10})	disregarded
8894	100	104	($\leq$ 6.0·10^{-7})	($\leq$ 1.4·10^{-7})	disregarded
8946 ± 3	152 ± 3	159 ± 3	= 6.5·10^{-7}	$\leq$ 9.2·10^{-9}	Hale
8972 ± 3	178 ± 3	186 ± 3	$\leq$ 2.6·10^{-6}	Görres	Görres
9000	206	215	($\leq$ 1.4·10^{-6})	Görres	disregarded
9038.7 ± 1	245 ± 1	256 ± 1	$\leq$ 2.6·10^{-6}	$\leq$ 1.3·10^{-7}	Hale
9072 ± 3	278 ± 3	291 ± 3	$\leq$ 2.2·10^{-6}	Görres	Görres
9103 ± 3	309 ± 3	323 ± 3	$\leq$ 2.2·10^{-6}	Görres	Görres
9113 ± 3	319 ± 3	333 ± 3	$\leq$ 3.0·10^{-6}	Görres	Görres
9147	353 ± 5	369 ± 5	$\leq$ 6.0·10^{-4}	Görres	Görres
9171 ± 3	377 ± 3	394 ± 3	$\leq$ 6.0·10^{-4}	Görres	Görres

Table 1.2.: Energy level with resonance strengths from Görres et al., Hale et al. and Iliadis et al. The resonance strengths in brackets indicate tentative states.

The measurement of Görres et al. 1982 [13] has been performed with a neon jet gas system and a proton beam in the energy range of $E = 70 - 355$ keV. The expected resonances in the energy range of $E_{res}^{lab} = 70 - 355$ keV have not been observed, but upper limits have been measured.

In the measurements of 1983 [11], the proton energy range covered $E_p = 300 - 1600$ keV and the resonance strengths of the resonances at $E_{res}^{lab} = 71$ keV and $E_{res}^{lab} = 159$ keV could have been deduced from direct capture processes. The upper limits of the resonance strengths for $E_{res}^{lab} = 369$ keV and 394 keV are taken from [15].

The results of Görres et al., are the reference values in the NACRE compilation (Nuclear Astrophysics Compilation of REaction Rates, 1999) [4] of the resonances $E_x = 8894 - 9171$ keV.

The measurements of Hale et al. [14] have been performed with ^{22}Ne(^{3}He,d)^{23}Na spectroscopy. Therein, a ^{22}Ne-implanted natural carbon foil has been irradiated by a 20-MeV ^{3}He^{2+} beam. In their study, new upper limits of the resonance strengths have been determined for the resonances $E_{res}^{lab} = 104$ keV, 159 keV and 256 keV. For the resonance at $E_{res}^{lab} = 159$ keV, a lower spectroscopic factor is chosen as in the publication of Görres et al. [11]. This is not contradicting because the authors caution that the result might not be reliable. The remaining resonance strengths are taken from Görres et al. [11].

Iliadis et al. [17] re-evaluated the measured values of the resonance strengths from [13, 11, 14]. The reaction rates and probability density functions based on Monte Carlo simulations. In this compilation, the tentative resonances at $E_{res}^{lab} = 71\,\text{keV}$, $104\,\text{keV}$ and $215\,\text{keV}$ have been disregarded. The other resonance strengths are still evaluated by the same upper limits from the publication of Görres et al [11].

Further experiments have been done by Longland et al (2010) [27]. In their research, they used an aluminium sheet with implanted ^{22}Ne which has been irradiated by a $E_p = 400 - 505\,\text{keV}$ proton beam. The resonance strength at $E_{res}^{lab} = 479\,\text{keV}$ has been determined with $\omega\gamma = 0.524 \pm 0.051\,\text{eV}$.

Further resonances in the range of $E_{res} = 400 - 1050\,\text{keV}$, have been measured by Piiparinen et al. (1971) [33], duToit et al. (1972) [41] and Meyer et al. (1973) [31]. Higher energetic resonances at $E_{res} \geq 800\,\text{keV}$ are reported by duToit et al. (1971) [42], Smit et al. (1979) [40] and the recent measurements of Kachan et al. (2006) [22].

1.3. Neon-Sodium-Cycle in Novae Eruptions

Novae are highly-energetic outbursts of matter in special astrophysical binary systems. The temperatures and mass abundances during novae eruptions provide good conditions for the neon-sodium-cycle.

1.3.1. Novae Explosions

Classical novae occur in binary systems consisting of a white dwarf and a massive star, which belongs to the main sequence. A white dwarf is a remnant of a main sequence star, which previously has burned all available hydrogen and helium nuclei in the CNO-cycle and finally ejected the outer shell. Due to the very high density conditions, the matter inside a white dwarf is degenerate.

The white dwarf continuously accretes hydrogen-rich matter from its companion. This matter flows from the outer Roche lobe region of the main sequence star through the Lagrange point to the white dwarf. Depending on the magnetic field of the white dwarf, the matter flows directly into the magnetic poles or in the case of a weak magnetic field it flows into an accretion disk [20].

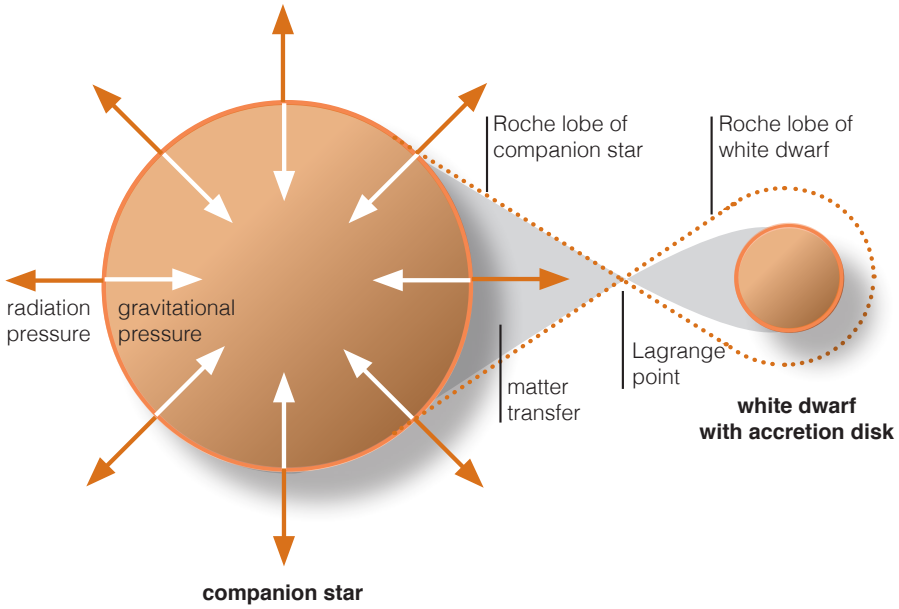

Figure 1.5.: Schematic view of the mass transfer in a binary system consisting of a white dwarf and a companion star.

Due to the strong gravitational field, the transferred mass reaches the white dwarf's surface with a very high velocity and causes the temperature to rise. At a certain temperature, the hydrogen is ignited. The surface of the white dwarf is still in a degenerate condition and cannot react smoothly by gas expansion. Meanwhile the products of the initial hydrogen burning initiate a thermonuclear runaway by a sudden increase of nuclear reactions in this environment getting hotter and denser. Finally, the energy from the nuclear reaction is released explosively. This causes an ejection of the outer layers of the white dwarf [37]. The maximum temperature during the runaway reaches up to $T_{max} = 4.5 \cdot 10^8\,\mathrm{K}$ which results in a rather complicated sequence of nuclear reactions. One assumes, that during the eruption a mass of around $\sim 10^{-4} - 10^{-5} M_\odot$ (solar masses) with $v \sim 10^2 - 10^3\,\mathrm{km/s}$ is ejected into space [20].

1.3.2. Observation of Novae

Binary systems which can create novae eruptions belong to the group of cataclysmic variables. This group of objects is classified by a change in the luminosity due to explosive processes, which follow a mass transfer between the binary partners.

Novae eruptions in binary systems can be observed in the light curves, which display the time evolution of the luminosity. The optical light curves show a fast rise in luminosity by a factor of $f \sim 10^4$ to a maximal luminosity of $L_{max} \sim 10^{37} - 10^{38}\,\mathrm{erg/s}$ in several days. The decreasing time of the optical luminosity depends on the type of novae and can happen in as few as 10 days or can continue up to 250 days [20].

The observations of novae light curves in non-optical wavelengths regimes show a different behavior. The bolometric luminosity (i.e. the luminosity integrated over all wavelengths) decreases more slowly when compared to the optical luminosity only. The maximum of the luminosity after the nova explosion is shifted towards higher wavelengths. This is explained by hydrogen burning re-started in the outer photosphere of the white dwarf after the nova eruption. The photosphere enters the inner shells and increases its blackbody temperature. This can be observed in a progressive hardening of the spectra from optical via UV to X-ray [20].

The infrared energy range also shows an increase in luminosity soon after the nova explosion. This can be explained by the re-radiation of UV by excited dust grains in the novae environment. Thus, the UV radiation causes a time-shifted "feedback" in the infrared range.

The analysis of the high energy radiation from novae gives also an inside look into the chemical abundance of the ejected matter. But unfortunately, the data sets do not provide yet a precise mass composition of novae. Presently, an enhancement in CNO elements and the presence of intermediate mass elements has been proven in all novae types that have been simulated [20].

1.3.3. Contribution to the Galactic Abundance

Depending on the the white dwarf composition, one can divide novae into two types with different initial atomic abundances: CO and ONe novae. Starrfield et al. predicted that CO-dwarfs are formed by intermediate-mass stars ($\sim 1-8$ $M_\odot$) and ONe-dwarfs are formed by more massive stars ($\sim 8-12$ $M_\odot$) because of different evolutionary phases. When the progenitors are more massive, the non-degenerate carbon ignition causes the formation of a degenerate core which mainly contains oxygen and neon, with traces of magnesium and sodium. ONe novae are characterized by a lower amount of material being ejected with higher velocity [38].

According to José et al., novae outbursts contribute with $\sim 6 \cdot 10^6$ $M_\odot$ to only 1/3000 of the Galactic disk's gas. This fraction it based on the following assumptions: a) ~ 30 novae events per year in a galaxy, b) a galaxy life time of $\sim 10^{10}$ years and c) an average ejected mass of $2 \cdot 10^{-5} M_\odot$. Therefore, novae do not contribute significantly to the Galaxy's metallicity but they might account for the abundance of special nuclei such as ^{13}C, ^{15}N and ^{17}O [20].

1.4. Reaction Theory with the Compound Nucleus Model

This chapter focuses on the theoretical description of nuclear interactions of two particles. After a general introduction of nuclear physical terms, the compound nucleus theory is presented. In the following, the nuclear reactions are described by quantum mechanics and the nuclear cross-section is introduced. Finally, the resonant and non-resonant interactions with charged particle interactions are presented. This paragraph is based on the explanations of Rolfs [37] and Iliadis [16].

1.4.1. General Introduction

In a nuclear reaction, the initial participating particles can be described as projectile j and target i. During the collision process, they are strongly interacting and transfer energy and momentum between each other. The outgoing particles after the collision process are named daughter m and ejectile o. There are two common nomenclatures in nuclear physics to describe a reaction:

$$i + j \rightarrow o + m \tag{1.2}$$

$$i(j, o)m \tag{1.3}$$

The emitted energy of a nuclear reaction corresponds to the energy difference of the initial and final particles. The energy of every particle $E_{particle}$ is defined by the sum of the rest mass energy $E_a^0 = m_a$ and the kinetic energy E_{kin} (with c =1).

$$E_{particle} = E_a^0 + E_{kin} \tag{1.4}$$

The nuclear mass m_{nucl} corresponds to the sum of all nucleon masses.

$$m_{nucl} = Z \cdot m_{proton} + (A - Z) \cdot m_{neutron} \tag{1.5}$$

For every nuclear reaction process, there is the characteristic Q-value which corresponds to the difference of the nuclear masses between the initial nuclei and final nuclei:

$$Q = (m_{nucl,j} + m_{nucl,i}) - (m_{nucl,o} + m_{nucl,m}). \tag{1.6}$$

The Q-value is therefor the amount of binding energy, that is released or consumed during a nuclear reaction. Depending on the different binding energy per nucleon in the nuclei, the reaction can proceed exothermally (positive Q-value) or endothermally (negative Q-value). The observed fusion reactions of the hydrogen burning processes have positive Q-values.

1.4.2. Compound Nucleus

The compound nucleus theory describes the physics happening during nuclear collision processes. This theory introduces a so-called "compound state" after the fusion of projectile and target. After the fusion, the compound nucleus a) emits light particles, b) evaporates photons or c) decomposes into other particles. Figure 1.6 shows a sketch of a reaction according to the compound-model with a gamma emission corresponding to the studied ^{22}Ne(p,γ)^{23}Na reaction.

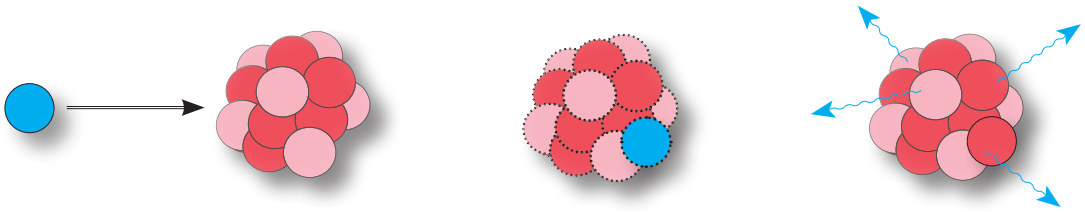

Figure 1.6.: The plot shows the nuclear reaction with the initial state, the compound state and the final state evaporating photons.

The quantum numbers (e.g. spin, parity) of the compound nucleus depend on the mass ratio and the excitation energy of the interacting partners. The compound nucleus is a model for a nuclear state whose formation and decay are not depending on each other. During the (for nuclear time scale) long life time of the compound nucleus, the system is equilibrated and not influenced by the formation process anymore [26]. In physical terms, one speaks about the independency of the entrance and exit channel.

1.4.3. Quantum Mechanical Description

With the tools of quantum mechanics, particles are described as de-Broglie waves. The wavelength λ_B corresponds to :

$$\lambda_B = \frac{2\pi}{\tilde{k}} \tag{1.7}$$

with the wavenumber $\tilde{k}$. The target nucleus is described by an effective nuclear potential $V(\vec{r})$ which is based on the characteristics of the nucleus. The projectile is described as a one dimensional plane matter wave $\Psi(\vec{r})$. The physical process of a scattering particle $\Psi(\vec{r})$ on a nuclear potential $V(\vec{r})$ is described by the time-independent Schrödinger equation:

$$E\psi(\vec{r}) = \left(-\frac{\hbar^2}{2m} + V(\vec{r})\right)\Psi(\vec{r}). \tag{1.8}$$

The wave function is a superposition of an incoming plane wave and a scattered radial wave:

$$\Psi(\vec{r}) = N\left(e^{i\vec{k}\vec{r}} + f(\Theta)\frac{e^{i\vec{k}\vec{r}}}{r}\right) \tag{1.9}$$

with the normalization factor N, the term $e^{i\vec{k}\vec{r}}$ for the projectile wave and the scattering amplitude $f(\Theta)$. The differential cross-section corresponds to the quadratic scattering amplitude $\frac{\mathrm{d}\sigma}{\mathrm{d}\Omega} = |f(\Theta)|^2$.

Assuming the projectile and target to have a charge, an additional contribution to the potential has to be considered: the Coulomb-potential. The incoming projectile wave has to pass the Coulomb barrier to interact with the nucleons in the potential.

The transmission coefficient describes the tunneling of the projectile through the Coulomb-Potential of the target nuclei. The leading term of the transmission coefficient for s-waves is the called Gamov-factor $\overline{T}$ and depends on the Sommerfeld-Parameter η:

$$\overline{T} = e^{-2\pi\eta} \tag{1.10}$$

$$\text{with } \eta = Z_1 Z_2 \cdot \alpha \cdot \sqrt{\frac{\mu c^2}{2E}} = Z_1 Z_2 \cdot \frac{e^2}{\hbar c}\sqrt{\frac{\mu c^2}{2E}}. \tag{1.11}$$

with the projectile charge Z_1, the target charge Z_2, the reduced mass μ, the fine structure constant α and the elementary charge e. The resonances of nuclei occur at specific projectile energies, when the projectile wave successfully passes the Coulomb-barrier and matches the boundary conditions at the potential wall. The depth V_0 of the potential has an impact on the wavelength of the particle inside the potential. For the first resonance, the nodes of the projectile wave match only the boundaries of the potential wall and for higher order resonances further nodes occur inside the potential.

1.4.4. Cross-Section

The cross-section is a measure for the probability that a reaction will occur for a pair of interacting nuclei. It is defined as the ratio of the rate of interactions $N_{interaction}/t$ and the rate of the incident particles N_{beam}/t per area A and per target nuclei N_{target}.

$$\sigma(E_p^{cm}) = \frac{N_{interaction}}{t} \cdot \left(\frac{N_{beam}}{t \cdot A} \cdot N_{target}\right)^{-1} \tag{1.12}$$

In a stellar environment, the projectiles and targets move with a relative velocity v which follows a probability distribution $P(v)$. The reaction rate $< \sigma v >$ takes into account both the velocity distribution as well as the velocity dependent cross-section

$$< \sigma v >= \int_0^\infty P(v) \cdot v \cdot \sigma(v)\ \mathrm{d}v \tag{1.13}$$

Assuming a non-degenerate environment, the particles move in a non-relativistic gas which is in a thermodynamic equilibrium. Under these conditions, the velocity probability can be expressed with the Maxwell-Boltzmann distribution:

$$P(v)\mathrm{d}\mu = 4\pi \cdot v^2 \left(\frac{\mu}{2\pi \cdot k \cdot T}\right)^{3/2} \cdot \exp\left(-\frac{\mu \cdot v^2}{2k \cdot T}\right) \mathrm{d}\mu \tag{1.14}$$

$$\text{or } P(E)\mathrm{d}E = \frac{2}{\pi}\frac{1}{(kT)^{3/2}}\sqrt{E}\, e^{-E/kT}\mathrm{d}E \tag{1.15}$$

with the temperature T and the Boltzmann constant k. The conversion from velocity dependence to the energy dependence has been performed with $\nu = \sqrt{\frac{2E}{\mu}}$.

Now, one obtains for the energy dependent reaction rate per particle pair:

$$< \sigma\nu > = \int_0^\infty \nu\sigma(E)P(E)dE \tag{1.16}$$

$$= \sqrt{\frac{8}{\pi\mu}}\frac{1}{(kT)^{3/2}}\int_0^\infty E\sigma(E)\, e^{-E/kT}dE. \tag{1.17}$$

The thermonuclear reaction rate for charged particle-induced reactions in the stellar gas is calculated as follows:

$$N_A < \sigma\nu > = \sqrt{\frac{8}{\pi\mu}}\frac{N_A}{(kT)^{3/2}}\int_0^\infty E\sigma(E)\, e^{-E/kT}dE \tag{1.18}$$

including the Avogadro constant N_A.

1.4.5. Charged Particle-Induced Non-Resonant Reaction

The cross-section of the particle induced reaction strongly increases in the low energy range and varies rather smoothly at high energies. One can introduce the so-called astrophysical S-factor $S(E)$ to obtain a less varying energy dependent measure:

$$\sigma(E) = \frac{1}{E}\cdot e^{-2\pi\eta}\cdot S(E) \tag{1.19}$$

The S-factor is often used for extrapolating cross-sections to astrophysical energies because of its smooth behavior. Assuming the S-factor to be constant $S(E) = \tilde{S}$, the reaction rate can be expressed as follows:

$$N_A < \sigma\nu > = \sqrt{\frac{8}{\pi\mu}}\frac{N_A}{(kT)^{3/2}}\cdot\tilde{S}\int_0^\infty e^{-2\pi\eta}\cdot e^{-E/kT}dE. \tag{1.20}$$

The term $e^{-E/kT}$ originates from the Maxwell-Distribution and approaches zero at large energies. The Gamov-factor $e^{-2\pi\eta} \sim e^{1/E}$ is an approximation for the probability of projectiles to tunnel trough the Coulomb barrier, assuming $l = 0$. The integrand of the product $e^{-2\pi\eta}\cdot e^{-E/kT}$ is referred to as Gamov peak and represents the energy range over which the majority of nuclear reactions are taking place in the stellar plasma. The maximum of the Gamov peak for a specific temperature is calculated as the following:

$$E_0 = \left(\left(\frac{\pi}{\hbar}\right)^2(Z_1Z_2e^2)^2\left(\frac{\mu}{2}\right)(kT)^2\right)^{1/3} \tag{1.21}$$

with the elementary charge e.

1.4.6. Charged Particle-Induced Resonant Reaction

In the energy region of nuclear resonances, the S-factor is varying strongly. For the following calculations, the resonances are assumed to be narrow and isolated. Being isolated means that neighboring resonances do not overlap significantly. Furthermore, the resonances are narrow, if the partial width Γ_i of the channel partners is approximately constant over the resonance width Γ. In this case, the cross-section can be described with the Breit-Wigner formula:

$$\sigma_{BW}(E) = \frac{\lambda^2}{4\pi}\frac{(2J+1)(1+\delta_{01})}{(2j_1+1)(2j_2+1)}\frac{\Gamma_a\Gamma_b}{(E_r-E)^2+\Gamma^2/4} \tag{1.22}$$

$$= \frac{\lambda^2}{4\pi}\cdot\omega\cdot\frac{\Gamma_a\Gamma_b}{(E_r-E)^2+\Gamma^2/4}, \tag{1.23}$$

with the spin of the resonance J, the spin of the target j_1 and projectile j_2, the total energetic width $\Gamma = \Gamma_a + \Gamma_b$ and the partial energetic widths of the entrance Γ_a and exit channel Γ_b. The parameter ω contains all spin dependent measures.

The thermonuclear reaction rate with the Breit-Wigner cross-section is introduced in the following:

$$N_A < \sigma\nu > = N_A\sqrt{\frac{8}{\pi\mu}}\frac{1}{(kT)^{3/2}}\int_0^\infty E\sigma_{BW}(E)e^{-E/kT}dE \tag{1.24}$$

$$= N_A\frac{\sqrt{2\pi}\hbar^2}{(\mu kT)^{3/2}}\cdot\omega\int_0^\infty\frac{\Gamma_a\Gamma_b}{(E_r-E)^2+\Gamma^2/4}e^{-E/kT}dE. \tag{1.25}$$

Assuming a narrow and isolated resonance, the partial widths and the Maxwell-Boltzmann term $e^{-E/kT}$ stay constant over the total width of the resonance at E_{res}:

$$N_A < \sigma\nu > = N_A\left(\frac{2\pi}{\mu kT}\right)^{3/2}\hbar^2 e^{-E_{res}/kT}\cdot\omega\frac{\Gamma_a\Gamma_b}{\Gamma} \tag{1.26}$$

$$= N_A\left(\frac{2\pi}{\mu kT}\right)^{3/2}\hbar^2 e^{-E_{res}/kT}\cdot\omega\gamma. \tag{1.27}$$

The parameter γ represent the width dependent measures.

The so called resonance strength $\omega\gamma$ corresponds to the product of the spin and width dependent measures and is a characteristic value for nuclear resonances:

$$\omega\gamma = \frac{(2J+1)(1+\delta_{01})}{(2j_1+1)(2j_2+1)}\cdot\frac{\Gamma_a\Gamma_b}{\Gamma}. \tag{1.28}$$

In the reaction ^{22}Ne(p,γ)^{23}Na, the target spin is $j_{^{22}Ne} = 0$ and the projectile spin is $j_p = 1/2$, assuming an incident s-wave proton at low energy.

2. Nuclear Network Calculation for Novae

In the following chapter, a nuclear network calculation has been performed in order to understand the processes taking place in the neon-sodium-cycle under novae conditions.

In the first part, the nuclear network code used and the necessary physics input parameters are presented. In the second part, the results for the evolution of the neon-sodium-cycle during the novae eruption and the final mass abundance in respect to different novae scenarios are shown. Furthermore, the influence of the thermonuclear reaction rate of ^{22}Ne(p,γ)^{23}Na on the final mass abundance is analyzed.

2.1. Physics Input

For the nuclear network calculation of the the neon-sodium-cycle in novae, the public domain libnucnet code from B. S. Meyer [30] has been used. It is a freely available code to compute yields from nuclear reaction networks for different astrophysical scenarios.

This code requires information about the stellar environment to calculate the atomic abundances for a given astrophysical scenario. The stellar environment is defined by the initial atomic abundance and the astrophysical trajectory. The astrophysical trajectory contains the temperature and density information in the binary system during the novae outburst. In the code used, a set of coupled differential equations determines the evolution of the isotope abundances of as a function of temperature and density. An additional fundamental input for these calculations are the reaction rates for the different reactions that occur during novae nucleosynthesis.

The network calculation which has been performed in this work, includes all nuclei up to germanium (Z=32). Furthermore, the final abundances take the β-decay of unstable isotopes into account. For the calculations of the entire network, the neutrino interactions are assumed to be negligible, because in novae outbursts the densities are too small for this interaction.

2.1.1. Initial Mass Composition

The initial mass composition of the binary system is based on the publication of Ritossa et al [35]. In this publication, the authors adopt a white dwarf with the mass of $M_{\mathrm{WD}} = 1.26\,\mathrm{M}_{\odot}$ and a companion with solar composition. The matter of the white dwarf involved in the novae process mainly originates in the CO-layer on top of the ONe core and the outer helium layer. Nevertheless, the lower regions also contribute to the mass abundance via convection [35]. The highlighted area in Figure 2.1 marks the surface of the white dwarf, which contributes to the initial abundance of the dwarf partner in the binary system.

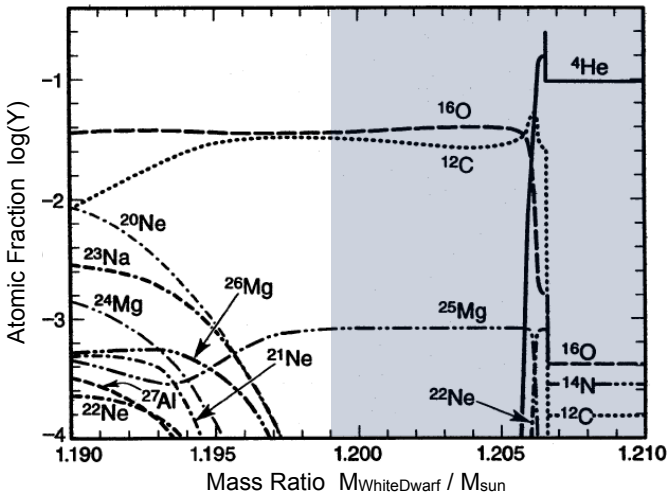

Figure 2.1.: Initial atomic fractions Y of several isotopes in a section of the white dwarf's surface [35].

Because of the mass transfer from the companion star to the surface of the white dwarf, the initial abundance has to take into account the contributing partner. In this work, a 50:50 mixing of the dwarf surface composition and the atmosphere of the companion star has been assumed. For the companion star, one uses the solar abundance from the Lodders [25] which is based on the measurements of meteoritic chondrite abundance and the solar photosphere. The calculated initial mass abundance is shown in Table 2.1.

Element	**Mass Abundance $\mathbf{X}_i$**		
	white dwarf	solar companion	50:50
$^{1}_{1}$H	0.000	0.711	0.355
$^{4}_{2}$He	0.339	0.274	0.307
$^{12}_{6}$C	0.306	0.002	0.154
$^{16}_{8}$O	0.343	0.006	0.175
$^{14}_{7}$N	0.002	0.001	0.002
$^{22}_{10}$Ne	0.002	0.000	0.001
$^{25}_{12}$Mg	0.007	0.000	0.003

Table 2.1.: Normalized initial mass abundances of the white dwarf, the companion star and the assumed 50:50 mixing state. Data taken from [25] and [35].

2.1.2. Temperature and Density Profile

For the nuclear network calculation, a characteristic nova temperature and density profile based on Starrfield et al. has been implemented [39]. This profile describes a nova eruption in the time range of 300 seconds and assumes a novae peak temperature of $T = 0.43\,\mathrm{GK}$.

In Figure 2.2, the time evolution of the temperature and density conditions are plotted. Before the novae eruption takes place, the temperature is around 0.1 GK. In the following nova outburst, the temperature increases by a factor of $f \sim 4$ within $\sim 5\,\mathrm{s}$. After the ejection of the outer envelope, the entire system is cooling down. The temperature decrease can be roughly fitted with an exponential function $T = T_0 \cdot e^{-t/\tau}$ ($\tau \sim 30\,\mathrm{s}$).

Based on the temperature profile of Starrfield et al. [39], the temperature profiles for the peak temperatures $T_{max} = 0.20, 0.25, 0.30$ and 0.35 GK have been modeled. It is assumed that density of the stellar environment has only a very small astrophysical impact on the nuclear reactions because of the degenerate conditions. Therefore, the density profiles have not been changed for the different peak temperatures.

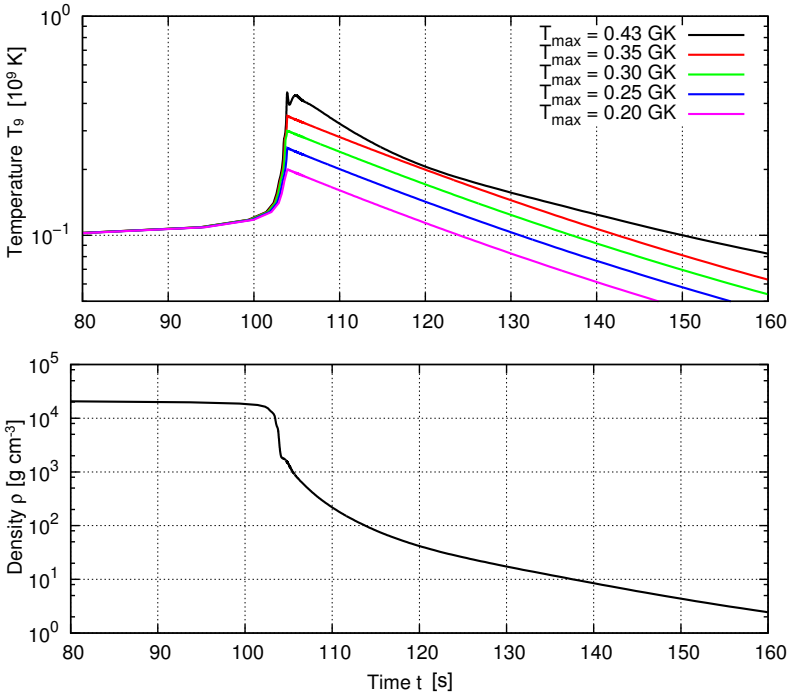

Figure 2.2.: Astrophysical trajectory for novae outburst with temperature and density profile for different peak temperatures based on the model of [39].

2.1.3. Thermonuclear Reaction Rates

The network calculations presented in the following paragraphs are based on the thermonuclear reaction rates (TNRR) of the JINA REACLIB [34] database. The TNRR of the reactions, which are participating in the neon-sodium-cycle, are taken from the recommended median rates from Iliadis et al. [17] as presented in Paragraph 1.1.

2.2. Results of Network Calculation

2.2.1. Evolution of Neon-Sodium-Cycle in Novae Eruption

With the help of the nuclear network code libnucnet [30], the fluxes of the nuclear reactions in the neon-sodium-cycle can be observed at every time step in the nova scenario. The nuclear reactions which are taking place in this scenario depend on the abundance of the involved isotopes and the temperature of the environment which has an impact on the thermonuclear reaction rate.

In the scenario presented in Figure 2.4, a nova explosion with a peak temperature of $T = 0.43\,\mathrm{GK}$ has been modeled with the nuclear network code. The fluxes of the nuclear reaction participating in the neon-sodium-cycle are plotted for six characteristic time steps before, during and after the nova explosion. A color scale and the arrow widths indicate the strengths of the fluxes. In the following, six characteristic time steps are explained in detail:

a) In the state before the nova eruption, the white dwarf has a temperature of around $T = 0.1\,\mathrm{GK}$. At this temperature, the neon-sodium-cycle is fed by the products of the CNO cycle (^{19}F(p,γ)^{20}Ne). The sodium isotopes ^{21}Na and ^{22}Na already process into the magnesium isotopes ^{22}Mg and ^{23}Mg by proton capture. The flux of the β^+-decay of ^{22}Na is too weak to be plotted.

b) With rising temperature of the starting nova explosion, the flux of the ^{22}Ne(p, γ)^{23}Na process increases and feeds the main decay reaction ^{23}Na(p,α)^{20}Ne. During the temperature rising time of about $t \sim 10\,\mathrm{s}$, the entire ^{22}Ne supply is processed into ^{23}Na.

c) At the peak temperature of $T = 0.43\,\mathrm{GK}$, a lot of processes are taking place at the same time. The isotope ^{20}Ne is preferably fed by ^{17}F(α,p)^{20}Ne, the β^+-decay of ^{20}Na, the α-capture of ^{16}O, the main destruction reaction ^{23}Na(p,α)^{20}Ne and the CNO-cycle. At this high temperature, the production of the magnesium isotopes ^{22}Mg and ^{23}Mg by proton capture of sodium isotopes is pushed forward. Furthermore, ^{24}Mg is created by α-capture of ^{20}Ne.

d.) At a temperature of $T = 0.2\,\mathrm{GK}$, the production of ^{20}Ne depends mainly on the reverse reaction ^{23}Na(p,α)^{20}Ne, the products of the CNO-cycle and the β^+-decaying ^{20}Na. In addition, the β^+-decay of ^{22}Na becomes relevant again.

e) Reaching the temperature of $T \sim 0.1\,\mathrm{GK}$, the neon-sodium-cycle runs at the initial temperature conditions. Because of the lower abundance of the neon and sodium isotopes, the production of magnesium isotopes is much weaker.

f) At the very low temperatures of $T < 0.05\,\mathrm{GK}$, the fluxes of the nuclear reactions in the neon-sodium-cycle are too weak and no more cycling can be observed. The β^+-decays of ^{21}Na and ^{22}Na are the two dominant processes taking place at this time step.

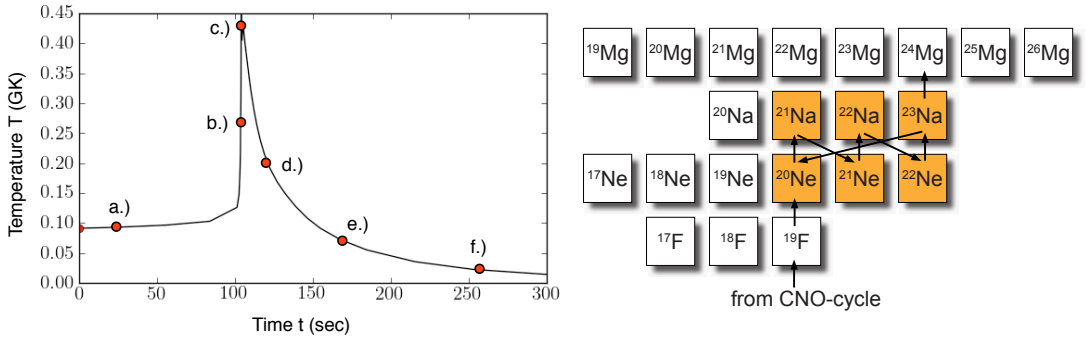

Figure 2.3.: **Left panel:** Temperature profile of nova eruption with time steps marked. **Right panel**: Reactions within the neon-sodium-cycle.

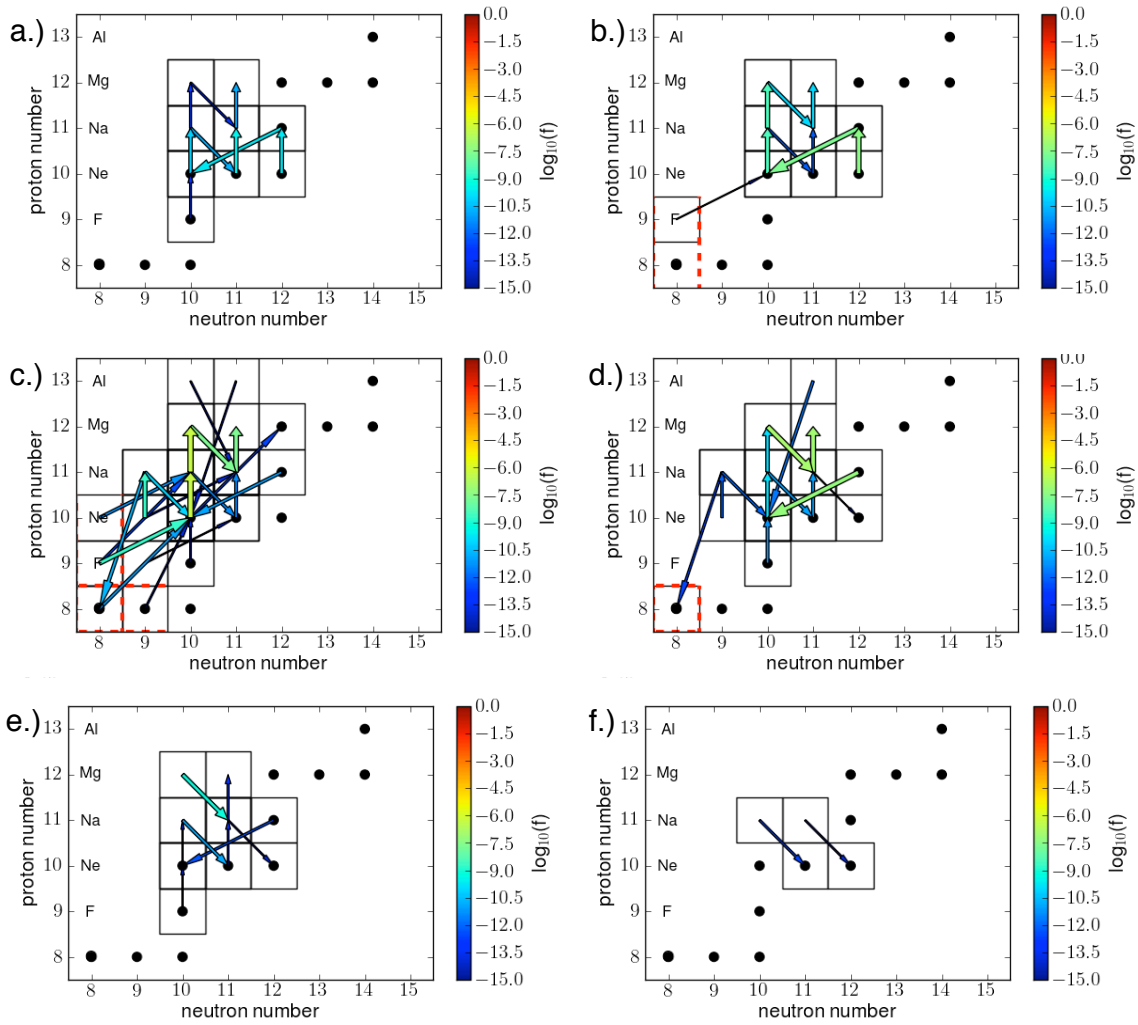

Figure 2.4.: Time evolution of neon-sodium-cycle for a nova with a peak temperature of $T_{max} = 0.43\,\mathrm{GK}$.

2.2.2. Influence of the Temperature Profile on the Nuclear Network

After implementing temperature profiles from section 2.1.2 in the network code, the abundances of the participating nuclei after the nova explosion can be calculated. Figure 2.5 shows the final abundances by number for the different novae scenarios with peak temperatures of $T_{max} = 0.2,\ 0.3,\ 0.43\,\mathrm{GK}$. The isotopes belonging to the same element are connected by a line.

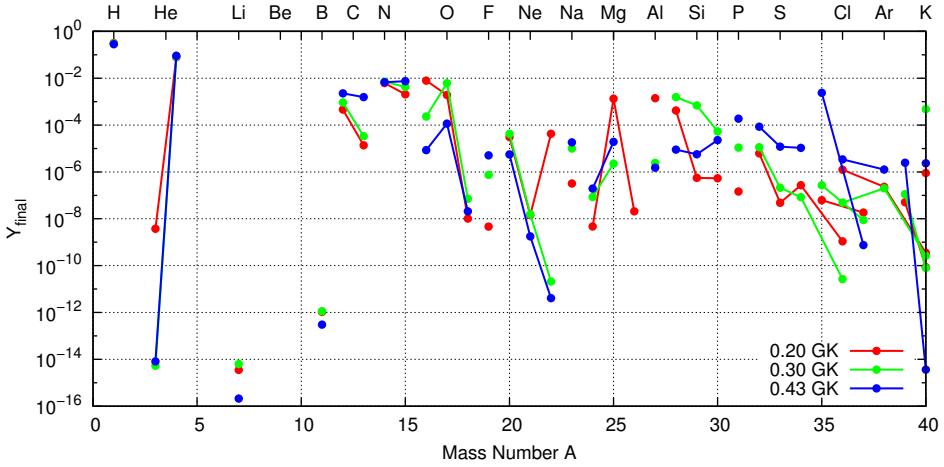

Figure 2.5.: Final abundance by number of the isotopes for different temperature profiles.

According to Figure 2.5, heavier elements are produced at higher novae peak temperatures due to the stronger processing of low mass elements. In contrast to this trend, the abundances of carbon and nitrogen also increase at higher temperatures. This can be explained by increasing photodissociation processes at higher temperatures.

In order to analyze the production rate of elements within the galaxy, one can determine the ratio of the final nova abundance X_{final} to the solar abundance X_{solar} (see Figure 2.6). It is assumed, that the galactic abundance is comparable to the solar abundance.

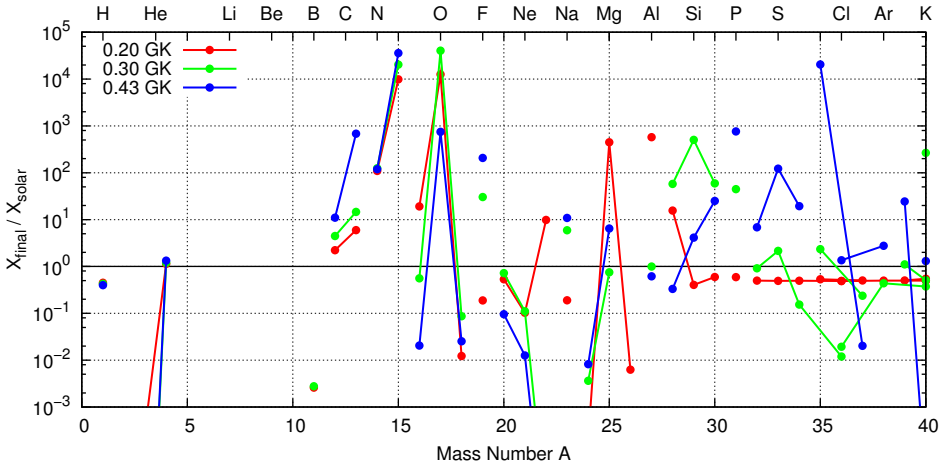

Figure 2.6.: Final abundance by mass number normalized to solar abundance for different temperature profiles.

The results from the network calculation confirm several observations of nova ejecta, which show a significant enhancement of intermediate mass elements [20]. From Figure 2.6, one can determine a strong overproduction (overproduction factor f) of the elements ^{13}C ($f = 10$), ^{15}N ($f = 10^4$) and ^{17}O ($f = 10^4$). In this case, one has to consider their dominant contribution in the initial abundances. For higher nova peak temperatures, more neon isotopes and light elements (e.g. He, Li, B) are destroyed in favor of the production of new intermediate nuclei. Depending on the increasing novae peak temperature, the production rate of heavier elements e.g. Al, Si, P, S, Cl and Ar increases as well.

It can be confirmed that the atomic number of the heaviest nuclei created (the so-called endpoint element) corresponds to $A < 40$. According to (José et al. [21]) this relation is valid for white dwarf masses near the Chandrasekhar limit ($M_{Ch} \sim 1.4\,\mathrm{M}_\odot$). This limit describes the maximal mass of a stable white dwarf when the electron degeneracy pressure can still resist the gravitational collapse.

2.2.3. Neon-Sodium-Cycle for Different Peak Temperature Profiles

The evolution of atomic abundances during the nova explosion strongly depends on the peak temperature assumed for the nova scenario. In Figure 2.7, the atomic abundances Y are shown for the nova peak temperature of a) $T = 0.2\,\mathrm{GK}$, b) $T = 0.3\,\mathrm{GK}$ and c) $T = 0.43\,\mathrm{GK}$ in the time range of $t = 90 - 130\,\mathrm{s}$ during the nova outburst.

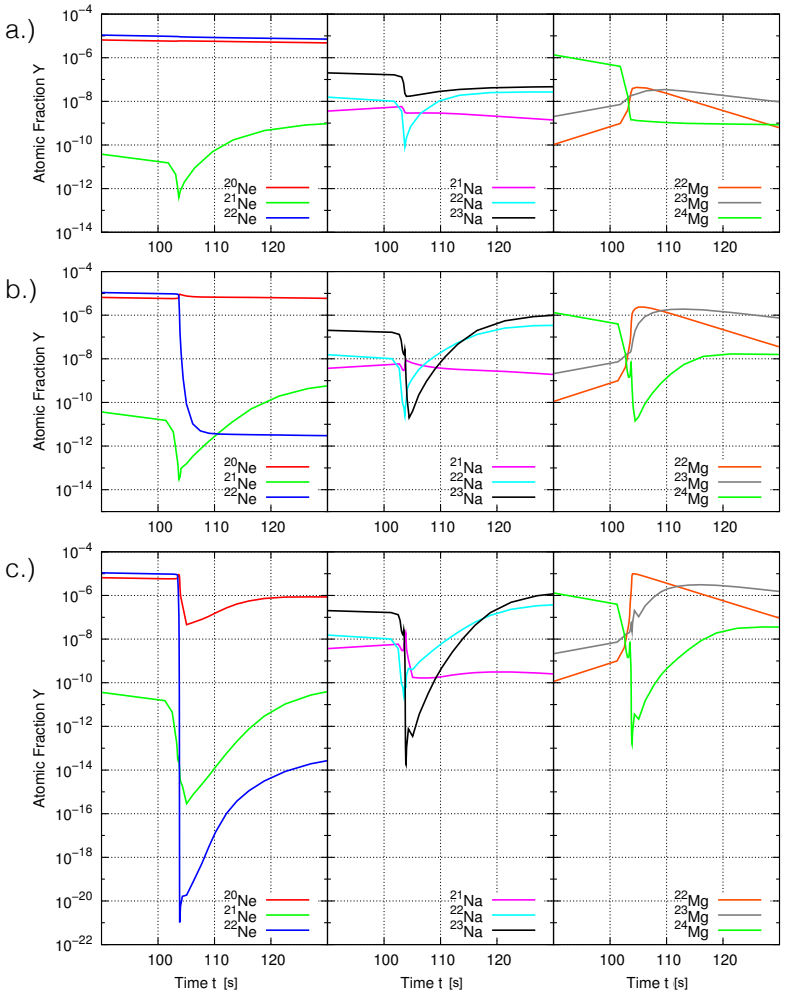

Figure 2.7.: Atomic fraction by number for reaction of the neon-sodium-cycle for novae peak temperatures at a) $T = 0.2\,\mathrm{GK}$, b) $T = 0.3\,\mathrm{GK}$ and c) $T = 0.43\,\mathrm{GK}$.

In Figure 2.7 a), the nova peak temperature is set to $T = 0.2\,\mathrm{GK}$. The isotope ^{20}Ne is constantly fed by the CNO cycle or ^{23}Ne(p,α)^{20}Ne and is then processed by proton capture: ^{20}Ne$\rightarrow{}^{21}$Na$\rightarrow{}^{22}$Mg. Consequently, no strong change in the ^{20}Ne abundance can be observed.
The second neon isotope ^{21}Ne is fed by the comparably slow β^+-decay of ^{21}Na. But the processing reactions ^{21}Ne$\rightarrow{}^{22}$Na$\rightarrow{}^{23}$Mg by proton capture are similar to the ^{20}Ne-isotope. The third neon isotope ^{22}Ne does not show a strong change in abundance due to the low temperature. As the ^{23}Ne(p,α)^{20}Ne reaction is more favored than ^{23}Na(p,γ)^{24}Mg, no increase in abundance of ^{24}Mg can be observed. The decrease of the magnesium isotopes ^{22}Mg and ^{23}Mg after the nova can be explained by the photodissociation and further processing.

In Figure 2.7 b) and c) it is clearly obvious, that at higher peak temperatures the neon isotopes - preferably ^{22}Ne and ^{21}Ne - are processed much more strongly into sodium and magnesium isotopes. One can see a steep abundance decrease for ^{22}Ne producing ^{23}Na. This isotope supports the reaction process: ^{23}Na$\rightarrow^{20}$Ne$\rightarrow^{21}$Na$\rightarrow^{22}$Mg as well as ^{23}Na$\rightarrow^{24}$Mg. The abundance of ^{24}Mg is also influenced by the β^+ decay of ^{24}Al.

2.2.4. Influence of the TNRR of ^{22}Ne(p,γ)^{23}Na

The last part of the nuclear network analysis focuses on the influence of the thermonuclear reaction rate of ^{22}Ne(p,γ)^{23}Na-reaction on the neon-sodium cycle. Therefore, the reaction rates have been multiplied by the factors of $f(\text{TNRR}) \sim 0$, $f(\text{TNRR}) = 1$ and $f(\text{TNRR}) = 1000$. Based on this changed reaction rates, the final abundances after the nova eruption have been calculated.

In Figure 2.8, the abundances over mass number Y are shown for different TNRR of ^{22}Ne(p,γ)^{23}Na. Comparing the disabled reaction ($f(\text{TNRR}) = 0$) with the normal reaction rate ($f(\text{TNRR}) = 1$), nearly no ^{22}Ne is processed and a decrease of intermediate mass elements (e.g. Na, Mg, Si, Cl) is obvious. On the basis of the strongly increased reaction rate ($f(\text{TNRR}) = 1000$), more intermediate elements could be produced by the processing of ^{22}Ne due to the stronger break-out of the neon-sodium-cycle.

In general, one can expect that new results of the TNRR for ^{22}Ne(p,γ)^{23}Na will not differ by the assumed factors. But these extreme conditions show the range of the impact of ^{22}Ne(p,γ)^{23}Na. Changes in its TNRR would influence the nucleosynthesis of the element abundance in the mass range of $A = 12 - 36$.

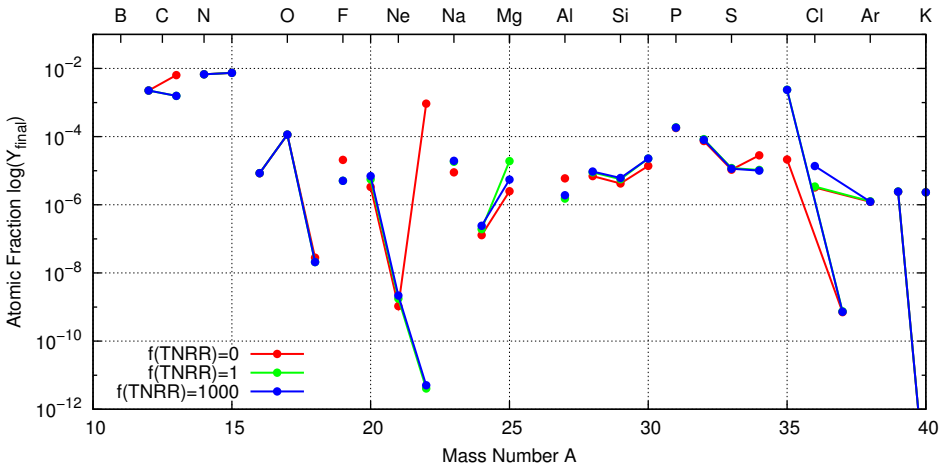

Figure 2.8.: Final abundance over mass number for different thermonuclear reaction rates of ^{22}Ne(p,γ)^{23}Na.

3. The LUNA Facility

The LUNA facility (Laboratory Underground for Nuclear Astrophysics) belongs to the Laboratori Nazionali del Gran Sasso (LNGS) Italy, which is situated in the underground of the Gran Sasso d'Italia. Its shield from the cosmic-ray induced background corresponds to 3400 m of water equivalent.

The LUNA apparatus measures astrophysically relevant reactions with low cross-section and benefits from the low background in the Gran Sasso Underground Laboratory. LUNA operates with a 400 kV accelerator and two beam lines for solid and gaseous targets, respectively.

The data of the ^{22}Ne(p,γ)^{23}Na reaction, which are analyzed in this diploma thesis have been measured with the LUNA apparatus in March 2012.

3.1. The LUNA Accelerator

The LUNA accelerator consists of a radio-frequency ion source, electrostatic lensing system and an inline Cockroft-Walton Generator. It can provide a proton beam or an α-beam in the energy range of $50 - 400$ keV. For the measurement of ^{22}Ne(p,γ)^{23}Na, a proton beam in the energy range of $E_{lab} = 100 - 400$ keV and a current of $I_{beam} = 110 - 125\,\mu$A have been used.

Inside the ion source, the radio frequency field ionizes neutral gas atoms. Due to the potential difference between the probe electrode (U_{probe}) and the extraction electrode ($U_{extraction}$) the positive ions leave the source and pass the extraction channel.

After leaving the ion source, the proton beam is accelerated and then guided to the gas target beam line by a bending magnet. Automatic feedbacks monitor and control the pressure in the gas target beam line and the cooling mechanism of the calorimeter.

The energy of the protons in the beam has been calibrated with the non-resonant radiative capture reaction ^{12}C(p,γ)^{13}N which is suitable for a wide energy range. According to Formicola et al. [9], one obtains:

$$E_p^{lab} = (U_{terminal} + U_{probe}) \cdot (0.9933 \pm 0.0002)\frac{\text{keV}}{\text{kV}} - (0.41 \pm 0.05)\,\text{keV}. \qquad (3.1)$$

Furthermore, the uncertainty of the beam energy comprises the error of the Q-value for ^{12}C(p,γ)^{13}N ($\Delta Q = 300\,\text{eV}$) and the error caused by the Doppler-shift correction ($\Delta x = 100\,\text{eV}$):

$$\Delta E_p^{lab} = \sqrt{(\Delta Q)^2 + (\Delta x)^2 + (\Delta x_{calib})^2} \tag{3.2}$$

Thus, the error of the beam energy is $\Delta E_p^{lab} = 0.37\,\text{keV}$. In Table 3.1, the technical information of the LUNA accelerator are summarized. Figure 3.1 shows the plasma ion source during the maintenance of the accelerator, and the second photo shows the accelerator tank in the experimental hall.

Technical Accelerator Information:	
energy spread	$\Delta E \leq 0.1$ keV
beam energy stability	$S \leq 5\ \frac{\text{eV}}{\text{h}}$
isolating gas composition	70% N_2, 20% CO_2, 10% SF_6
isolating gas pressure	$p = 20\,\text{bar}$
hydrogen beam current	$I(p) = 0.5$ mA
helium beam current	$I(\alpha) \leq 0.4$ mA

Table 3.1.: Technical information about the LUNA accelerator.

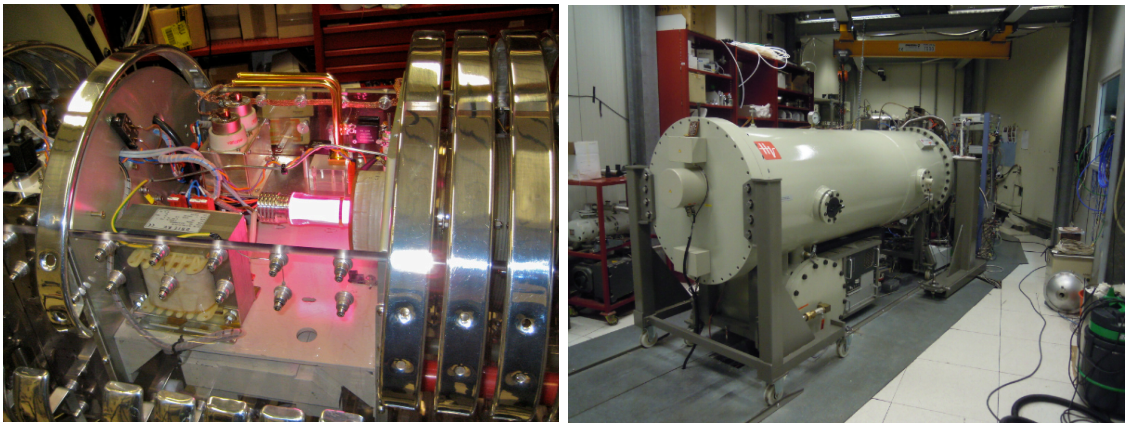

Figure 3.1.: **Left Panel:** The ion plasma chamber in the LUNA accelerator (credits to Michael Anders). **Right Panel:** The LUNA accelerator tank in the experimental hall.

3.2. Gas Target Setup

The gas target setup consists of a pumping system, a windowless gas target chamber, a calorimeter, the HPGe detector and the lead shield. After leaving the accelerator, the beam enters the gas target chamber and collides with the target gas atoms. The emitted photons are measured by the high purity germanium (HPGe) detector which is positioned underneath the reaction region. At the end of the target chamber, the beam intensity is measured by a calorimeter.

3.2.1. Windowless Gas Target Chamber

The measurement at LUNA has been performed with the setup of the former $^{2}H(\alpha,\gamma)^{6}Li$-experiment [3]. This target chamber contains a special tube ("Tubetto") along the beam axis which stops the deuterons from interacting with the target walls and prevents the production of neutrons. For our experiment, this tube has no physical impact.

The target chamber is constructed as a rectangular stainless steel box with an inlet for the beam, a flange for the calorimeter and an indentation for the HPGe-detector. It has to be pointed out that the gas target chamber is designed to be windowless. This is related to the fact that no window material fulfills the conditions of low energy straggling of the beam. Furthermore, the window material should be highly stable towards the big pressure difference between target chamber gas and the vacuum in the beam line.

In consequence, the target gas is introduced into the target chamber, reacts with the proton beam and leaves the chamber trough the beam collimators. Afterwards, it is pumped into a gas circuit by three separate pumping stages along the beam line, cleaned in the purifier by passing a chemical getter and finally restored in the buffer.

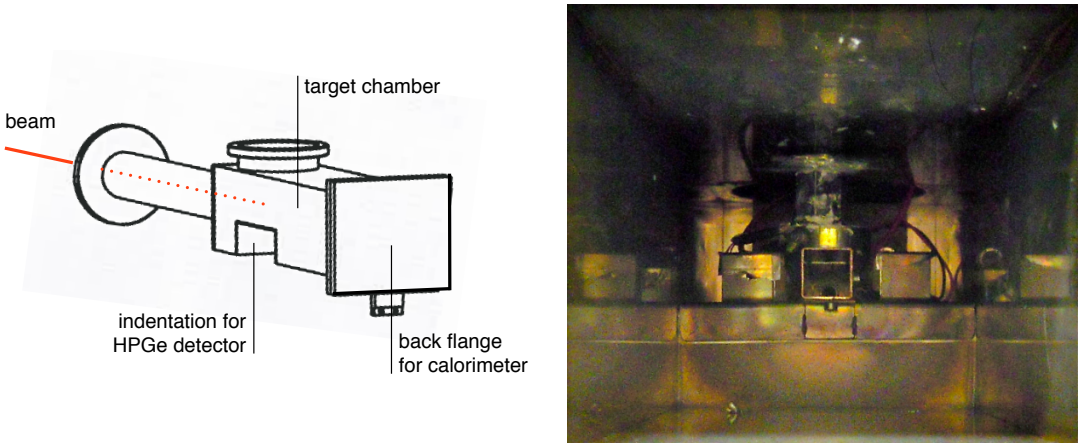

Figure 3.2.: **Left Panel:** Sketch of the target chamber (courtesy of LNGS).
Right Panel: Target chamber in beam axis in direction of the beam.

3.2.2. Pumping System

The pumping system consists of three stages with different pumps to maintain the accelerator vacuum. With the help of several valves, one can control the correct gas flow inside the setup.

After the target gas passes the three pumping stages, it is guided into the purifier. Inside the purifier it is cleaned and will then be pumped into the buffer. In the following, either the recirculated gas of the buffer or the target gas from the gas bottle enters the target chamber again. In Figure 3.3, the pumping process is shown in a schematic plot. The technical plot of the setup is attached in Figure 3.4.

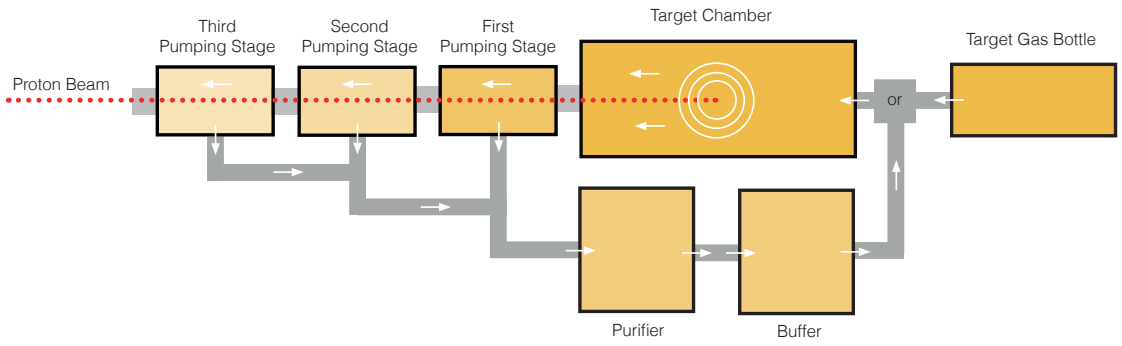

Figure 3.3.: Schematic plot of the gas target setup with the pumping system.

In Table 3.2, the pressure ranges and corresponding pumps in the different parts of the setup are presented. The target pressure is assumed to be about $p_{target} \sim 1\,\text{mbar}$. One has to note that the pressure inside each of the pumping stages depends on the pressure inside the target chamber.

Stage	Pressure	Pump	Operating Principle	Pumping Speed
1	$\sim 10^{-3}$ mbar	Ruvac WS 2001 Leybold	roots pump	2050 m^3/h
		Ruvac WS 501 Leybold	roots pump	500 m^3/h
		Ecodry Leybold	dry forepump	40 m^3/h
2	$\sim 10^{-7}$ mbar	2x Turbovac 1000 Leybold	turbomolecular pump	1000 l/s
		1x Turbovac 1500 Leybold	turbomolecular pump	1500 l/s
3	$\sim 10^{-7}$ mbar	Turbovac Pfeiffer	turbomolecular pump	360 l/s

Table 3.2.: Pumps of the gas target system and their properties.

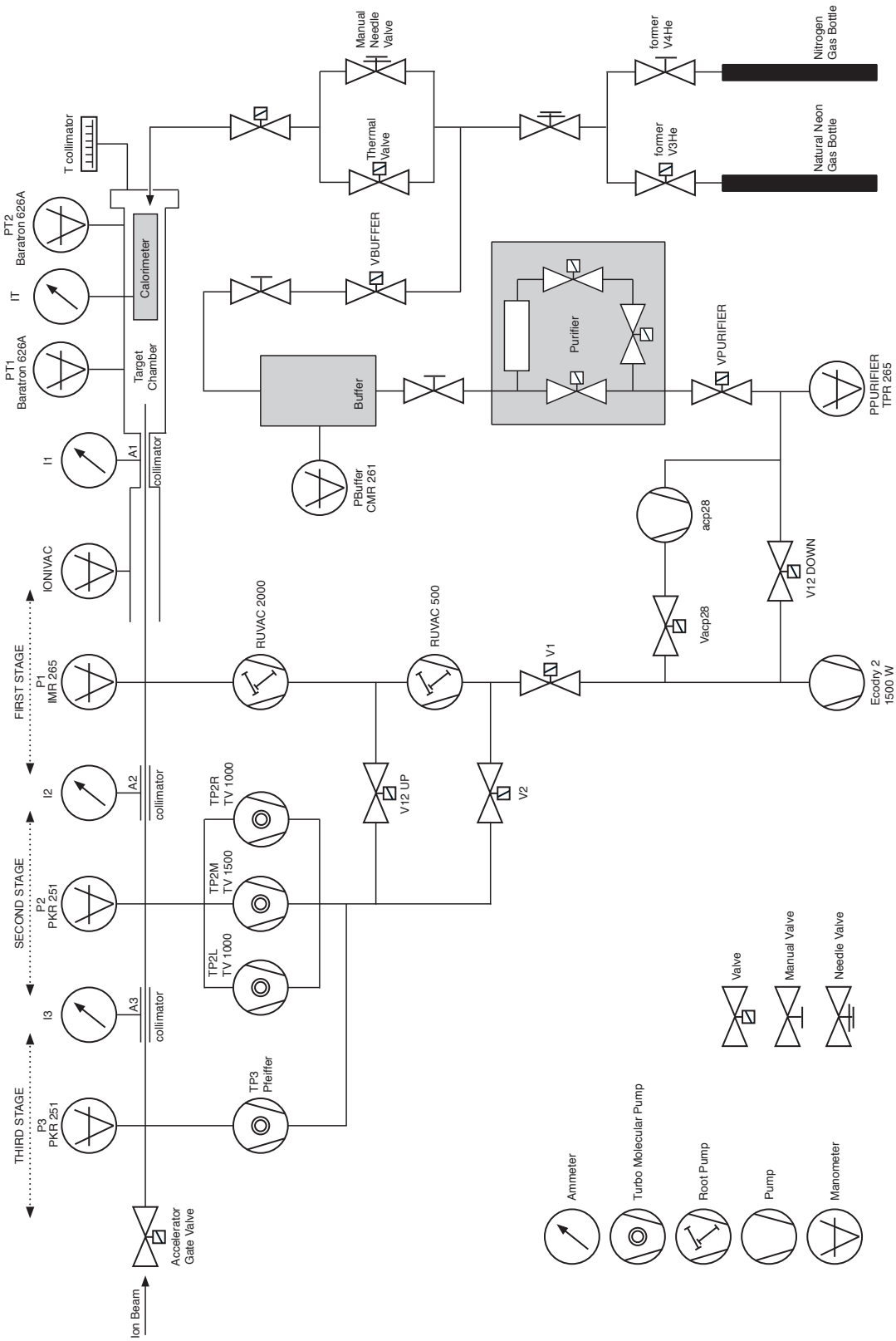

Figure 3.4.: Pumping scheme of the gas target setup with the pumping system

3.2.3. Target Gas for ^{22}Ne(p,γ)^{23}Na

The target gas used for the measurements at LUNA has been delivered by Linde. It is Neon 5.0 gas, which contains natural neon gas with 99.999% chemical purity. The fractions of the impurities O_2, N_2, H_2O, C_nH_m and He are listed in Table 3.3.

Element	Mole Fraction	Atomic mass
O_2	≤ 1 ppm	15.994 u
N_2	≤ 2 ppm	14.003 u
H_2O	≤ 2 ppm	18.015 u
CnHm	≤ 0.1 ppm	
He	≤ 5 ppm	4.003 u

Table 3.3.: Impurities in Neon 5.0 gas from Linde.

According to the manufacturer instruction of Linde, the target gas Neon 5.0 has been extracted from air. In order to be very conservative and as the geographical position of the originating air is not known, the variation of neon isotopes in all natural sites has to be taken into account. Table 3.4 shows the mole fractions of the neon isotopes in natural variation, the best measured composition from a single terrestrial source and the adopted composition. The values are taken from the Atomic Weights of the Elements Database of the International Union of pure and applied chemistry [1].

Element	Natural Variation	Best Measured	Adopted	Atomic mass
^{20}Ne	$88.47\% - 90.51\%$	$(90.4838 \pm 0.0090)\%$	$(90.48 \pm 2.01)\%$	19.992 u
^{21}Ne	$0.27\% - 1.71\%$	$(0.2696 \pm 0.0005)\%$	$(0.27 \pm 1.44)\%$	20.994 u
^{22}Ne	$9.20\% - 9.96\%$	$(9.24565 \pm 0.0090)\%$	$(9.25 \pm 0.72)\%$	21.991 u

Table 3.4.: Composition of neon isotopes in the target gas.

3.3. Calorimeter

The calorimeter measures the beam intensity at the end of the target chamber. The front part of the calorimeter, which is in direct contact with the beam, is heated by resistors to a temperature of 70 °C. The cold side of the calorimeter has a temperature of 0.3 °C. Inside the calorimeter, there is an electrically insulating cooling liquid at 0 °C which cools down the cold sections.

The resistors inside the calorimeter dissipate a beam energy dependent power to maintain the set point temperature of the calorimeter at 70 °C. The so called zero-power P_0 is measured during the absence of the beam. If the beam enters and heats the calorimeter, the resistors deliver a lower power of P_{run} to reach 70 °C. The beam power P_{beam} is calculated in the following way:

$$P_{beam} = P_0 - P_{run}. \tag{3.3}$$

For the power of the resistor, one can assume an upper limit for the error of $\Delta P = 0.3\,\mathrm{W}$. The target current I_{target} is calculated as follows:

$$I_{target} = \frac{P_{beam}}{E_{calo}} \cdot e = \frac{P_0 - P_{run}}{E_p^{lab} - E_p^{loss}} \cdot e \tag{3.4}$$

including the beam energy E_{calo} at the calorimeter and the energy loss E_{loss} of the beam in the target gas (see paragraph 4.1.2). Due to the calibration error of the calorimeter, one assumes a relative error of $\Delta I/I = 1.5 - 3\%$ for the target current.

The calorimeter temperature is controlled by LabView. Furthermore, an automatic interlock system prevents the calorimeter from overheating.

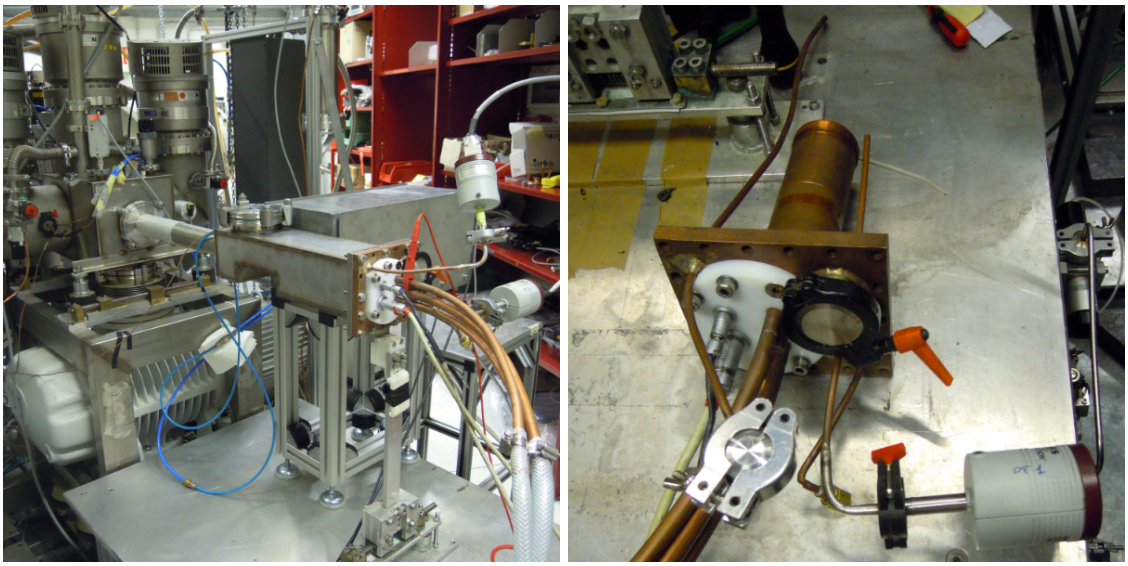

Figure 3.5.: Back end of the target chamber with calorimeter.

3.4. High-Purity Germanium Detector

The high-purity germanium (HPGe) detector was fabricated by Canberra and measures the γ-rays from the nuclear reaction in the target chamber. It contains a cylindric germanium crystal with a diameter of $d_{crystal} = 86\,\text{mm}$ and a length of $l_{crystal} = 85\,\text{mm}$. The HPGe detector is cooled with liquid nitrogen ($T \sim 80\,\text{K}$) (see Figure 3.8). The signals measured by the detector are processed by two independent data acquisition chains. In the first chain, the signals are digitized in a CAEN N1728B digitizer and then read out with the TNT2 software. In the second chain, the signals are amplified in a spectroscopic amplifier, digitized in an Ortec 919E unit and finally read out with the Maestro software.

3.4.1. Energy Calibration

The energy calibration of the channels is based on the γ-lines of the isotopes ^{214}Pb, ^{208}Tl, ^{214}Bi, ^{228}Ac, ^{60}Co, ^{40}K, ^{16}O and the 511 keV line (of the positron-electron annihilation) of the laboratory background radiation. The isotope ^{16}O originates from the proton capture of ^{19}F. For the calibration relation of the TNT2 software with the energy E and the channel number x_{ch}, one obtains:

$$E = (2.768 \pm 1.082) + (0.989 \pm 0.001) \cdot x_{ch} + (2.8 \pm 0.2) \cdot 10^{-6} \cdot x_{ch}^2. \quad (3.5)$$

In Figure 3.6, the calibration data and the determined calibration function are shown.

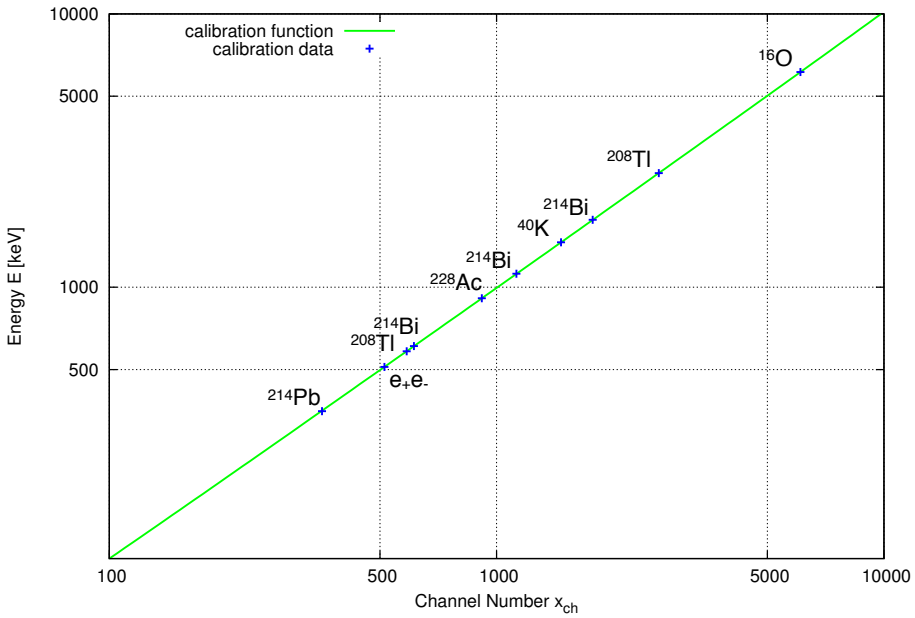

Figure 3.6.: Data of calibration sources and the determined calibration curve of the HPGe-detector with the TNT2 software.

3.4.2. Detection Efficiency

The detection efficiency μ_{det} corresponds to the full energy peak efficiency [23] and depends on the γ-energy of the emitted photon and the position of the emission inside the target chamber. The determination of the efficiency for LUNA is based on the measurements from Anders et al. using ^{88}Y ($E_\gamma = 898, 1836\,\text{keV}$), ^{60}Co ($E_\gamma = 1173, 1333\,\text{keV}$) and ^{137}Cs ($E_\gamma = 662\,\text{keV}$) sources. The efficiency curves are assumed to have a relative error of $\Delta x/x = 2.2\%$ [3].

Figure 3.7 shows the efficiency curves for $E_\gamma = 440\,\text{keV}$, which has been obtained by extrapolation, and for $E_\gamma = 1626\,\text{keV}$, which has been obtained by interpolation of the measured data. One has to note, that the position x starts at the end of the collimator. The efficiency for every γ-energy depends on the position of interaction and can be finally determined by linear approximation. For the observed γ-energies, the average detection efficiency is $\mu_{det}(440\,\text{keV}) = 0.0261 \pm 0.0028$ and $\mu_{det}(1636\,\text{keV}) = 0.0159 \pm 0.0014$.

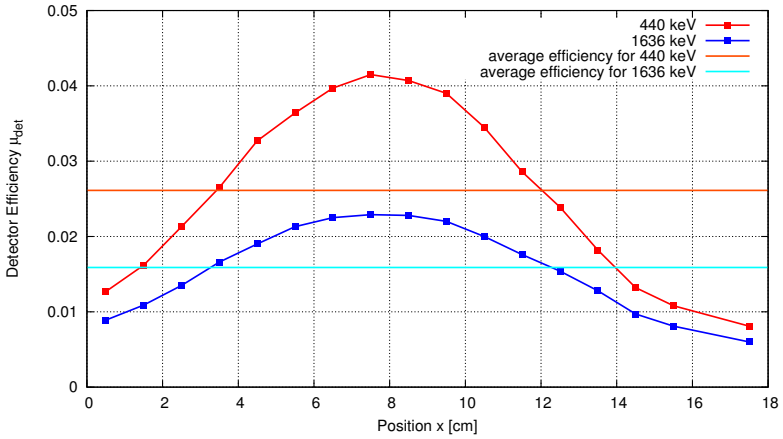

Figure 3.7.: Efficiency curve and average detection efficiency of the HPGe detector for $E_\gamma = 441\,\text{keV}$ and $1636\,\text{keV}$.

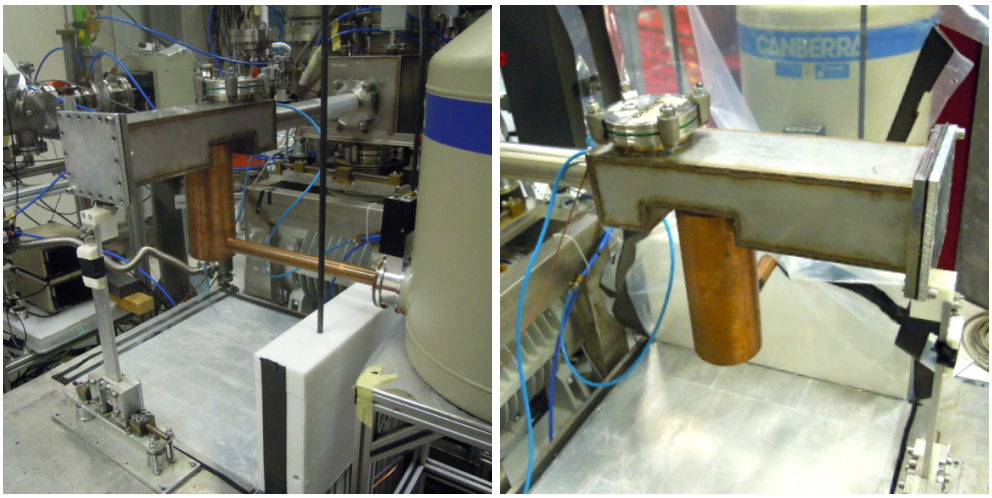

Figure 3.8.: Target chamber and HPGe detector with liquid nitrogen vessel.

3.5. Lead Shielding

The Gran Sasso Laboratory is one of the facilities with the lowest laboratory background radiation in Europe. But also in this facility, the target chamber and the HPGe-detector still have to be shielded from the natural radioactivity inside the tunnel.

The radiation shield of LUNA consists of a lead layer with a minimum thickness of $d_{lead} = 20\,\text{cm}$ against γ-radiation. The lead shield is additionally covered by a layer of polyethylene with an average thickness of $d_{PE} = 10\,\text{cm}$ to shield from neutrons. On the back end of the setup, there is a second shield to cover the service connections of the calorimeter and protect the backside of the target chamber.

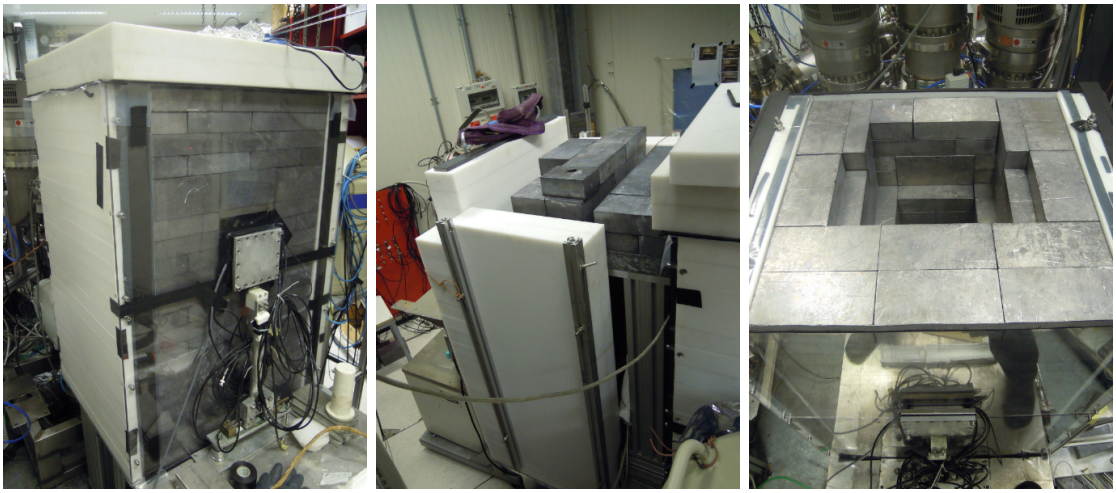

Figure 3.9.: **Left Panel:** Lead shield around the target chamber without the back shield. **Central Panel:** Back shield for protection of the back side of the chamber. **Right Panel:** View inside the partly dismounted lead castle.

3.6. Beam Heating Setup

For the study of the beam heating (see paragraph 4.1.3) inside the target chamber, a measuring facility has been developed. It consists of a 2 inch NaI-detector which is positioned inside a lead castle. The entire setup is placed next to the target chamber and can be moved horizontally. According to the resonance scan method presented by Görres et al. in 1980 [12], this facility will measure the beam heating effect in future. A figure of the setup is attached in the Appendix (see Figure A.8).

The photon signal measured by the NaI-detector passes a preamplifier and an ORTEC Amplifier 671 unit. Afterwards, it is converted in a ORTEC EtherNIM 919E Multichannel ADC and read out by the Maestro Software. Table 3.5 lists important setup parameters.

High-Voltage Supply for PMT	
High Voltage U_{HV}	-1300V
Scintillation Preamplifier ORTEC 113	
Capacity C	1000 pF
Spectroscopy Amplifier ORTEC 671	
Coarse gain	5
Fine gain	0.5
Shaping time t	0.5 μs
Mode	gauss
BLR	auto
Polarity	positive

Table 3.5.: Parameters for the instruments used for the beam heating study.

The lead castle surrounding the NaI-detector has a thickness of 5 cm and shields from background radiation. It includes a collimator with a thickness of 5 cm and a hole diameter of $\varnothing = 2$ cm. The outer dimensions of the lead castle are 20 cm × 20 cm × 50 cm. The entire setup is fixed on a Bosch-profile frame and is situated directly next to the target chamber (see Figure 3.10). The distance between the NaI-crystal and the position of interaction inside the target chamber is $\sim$ 13.3 cm. The design of the beam heating setup provides appropriate conditions in terms of detection efficiency, shielding from radiation and weight for the moving of the entire setup.

For the measurement at LUNA, the resonance at $E_{res}^{lab} = 272$ keV of the ^{21}Ne(p,γ)^{22}Na reaction and the resonance at $E_{res}^{lab} = 385$ keV of the ^{20}Ne(p,γ)^{21}Na reaction have been selected. Due to beam time constraints, these measurements will be performed by members of the LUNA collaboration in near future, probably in 2013.

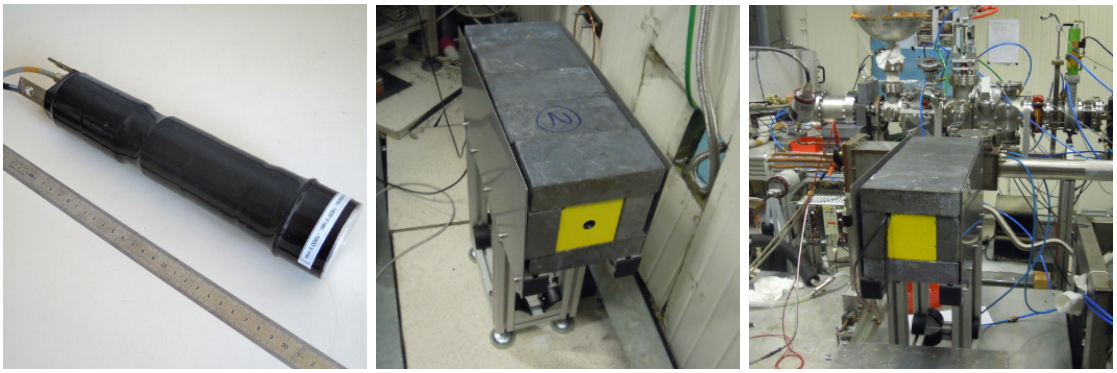

Figure 3.10.: **Left Panel:** The 2 inch NaI-detector. **Central Panel:** Front view of lead castle with collimator. **Right Panel:** Back view of lead castle next to target chamber.

3.7. Data-Taking Procedure

The data analyzed for this diploma thesis have been taken in March 2012 at LUNA with the setup described in the previous sections. The objective of this test phase was the preparation of the setup, the data-taking and finally the analysis of the data quality and the evaluation of possible external influences on the measurement.

Before starting the measurements, the pumps and the gas target valves have been tested. After reaching an appropriate vacuum state inside the setup, the target chamber has been filled with the neon target gas. Further checks were performed with the germanium detector and the calorimeter. The accelerator has been set to provide a proton beam in the energy range of $E_p^{cm} = 100 - 400\,\text{keV}$.

For obtaining the right position of the resonance reaction directly above the HPGe-detector, the target pressure had to be adapted to the designated energy loss of the proton beam. The measurements have been performed with the proton beam in the energy range of $E_p = 122 - 400\,\text{keV}$ with 10 keV steps. The target gas has been irradiated for about $t \sim 15\,\text{min}$ per run. Additionally, long over-night runs ($t \sim 12\,\text{h}$) have been performed at energies of $E_p = 162\,\text{keV}, 191\,\text{keV}$ and 258 keV. These proton energies correspond to the energies of promising resonances of the $^{22}\text{Ne}(\text{p},\gamma)^{23}\text{Na}$-reaction.

4. Data Analysis

In this chapter, the analysis methods of the data taken during the measurements at LUNA are described. At first, the beam energy loss processes in the target gas and the applied correction methods for the analysis are introduced. Then, the analysis of the γ-ray spectra taken by the HPGe detector at LUNA is presented. In this respect, the background in the laboratory and the background caused by beam interactions with the target gas are evaluated. To this end, the statistic methods for the determination of the photo peaks are explained.

4.1. Beam Energy Loss in Target Gas

While passing through the target gas, the beam protons are slowed down by collisions with the target atoms. This stopping process has a strong influence on the measurements at LUNA because the beam energy decreases due to the energy loss. Furthermore, the target gas is heated up by the collisions of beam protons and target nuclei.

4.1.1. Stopping Power

The beam-proton collisions can be divided into two categories: electronic and nuclear collisions. The dominant electronic stopping is caused by inelastic collisions between bound electrons of the target atoms and the beam protons. The second and much weaker process is the stopping of the beam projectiles by elastic collisions with the target nuclei themselves. At low beam energies, the stopping power is influenced by the nuclear component, but in the intermediate energy range it is rather negligible ($E_p > 30\,\mathrm{keV}$), and the stopping power can be described by the Lindhard-Scharf-Schiott theory and the Bethe-Bloch formula [16].

The stopping power is defined by the ratio of the differential energy loss $\mathrm{d}E_{loss}$ and the differential path length $\mathrm{d}x$ per number density N in the absorber material:

$$\epsilon = -\frac{\mathrm{d}E_p^{loss}}{N \cdot \mathrm{d}x} \quad (\text{in eV} \cdot \text{cm}^2/\text{atom}). \tag{4.1}$$

As shown in Figure 4.1, the total stopping power has been calculated for a gas-like neon target using the SRIM Code (version 2008.04) [43]. The SRIM Code assumes an error of $\Delta\epsilon/\epsilon = 1.7\%$ for the stopping power of protons in neon.

In the experiment at LUNA, the target gas is a composition of different isotopes. The different isotope fractions have to be considered to calculate the effective stopping power for the isotope of interest which is related to the reaction. The molar fractions are based on the adopted values in paragraph 3.2.3.

For the effective stopping power ϵ_{eff} per active ^{22}Ne-atom, one obtains ϵ_{eff}^{lab} for the laboratory frame and ϵ_{eff}^{cm} for the center-of-mass frame :

$$\epsilon_{eff}^{lab}(E_p^{lab}) = \epsilon_{tot}^{lab}(E_p^{lab}) \cdot \left(1 + \frac{\tilde{N}(^{21,20}\mathrm{Ne})}{\tilde{N}(^{22}\mathrm{Ne})}\right) = \epsilon_{tot}^{lab}(E_p^{lab}) \cdot \left(\frac{1}{\tilde{N}(^{22}\mathrm{Ne})}\right) \tag{4.2}$$

$$= \epsilon_{tot}^{lab}(E_p^{lab}) \cdot \left(\frac{1}{(0.0925 \pm 0.0072)}\right) \tag{4.3}$$

$$\tag{4.4}$$

$$\epsilon_{eff}^{cm}(E_p^{cm}) = \epsilon_{eff}^{lab}(E_p^{cm}) \cdot \frac{m_{target}}{m_{target} + m_p} \tag{4.5}$$

$$= \epsilon_{eff}^{lab}(E_p^{cm}) \cdot 0.95618 \tag{4.6}$$

Based on the natural variation of neon, the fraction of ^{22}Ne has been adopted to $(9.25 \pm 0.72)\%$. This results in a relative error for the effective stopping power of $\Delta\epsilon_{eff}/\epsilon_{eff} = 8\%$.

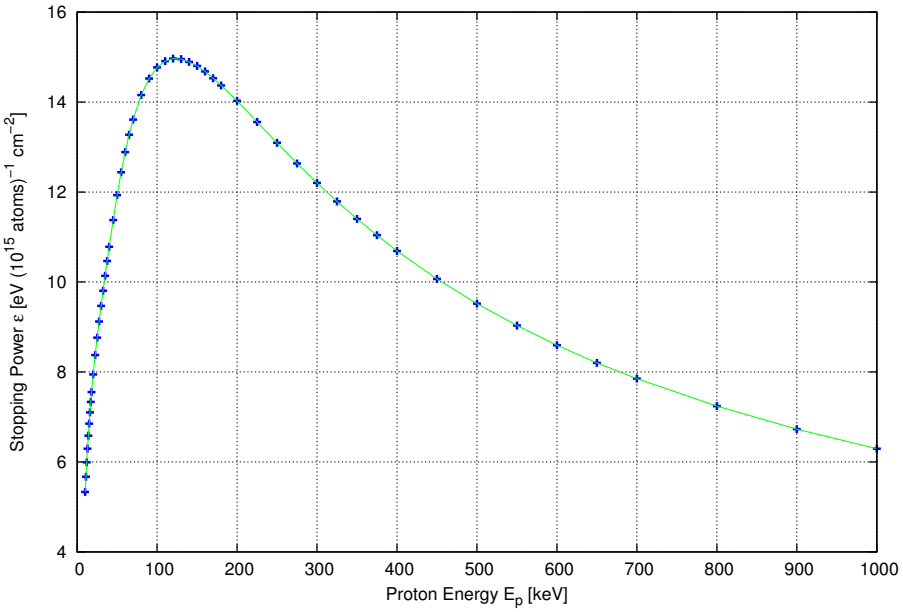

Figure 4.1.: Stopping power for protons in neon gas [43].

4.1.2. Energy Loss

The energy loss E_p^{loss} of the beam at a certain position inside the target chamber depends on the beam energy depending stopping power $\epsilon(E)$, the distance of travel l and the target gas number density n. It is expressed as the following:

$$E_p^{loss} = \epsilon(E_p) \cdot l \cdot n. \tag{4.7}$$

Target Length

As shown in Figure 4.2, the proton beam enters the LUNA target chamber through a collimator, interacts with the target gas and finally hits the calorimeter at the end of the chamber. The distance from the collimator to the endcap of the calorimeter is $l = 17.7$ cm. Inside the collimator ($l = 4.0\,\text{cm}$), the target gas pressure decreases remarkably. Therefore, the collimator acts like an additional gas volume with an effective length of $l_{coll}^{eff} = (2.5 \pm 0.5)\,\text{cm}$. In total, the effective target length is estimated to be $l_{target} = (20.2 \pm 0.5)\,\text{cm}$ with a relative error of $\Delta l_{target}/l_{target} = 2.5\%$.

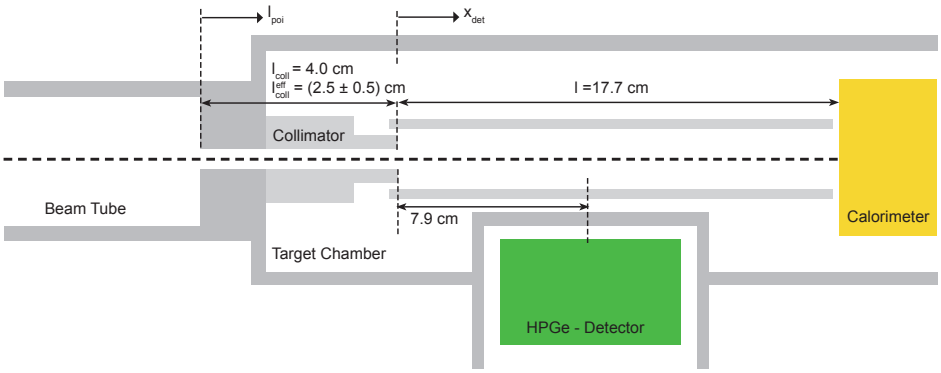

Figure 4.2.: Schematic sketch of LUNA chamber in side view.

Target Density

The target gas is considered to be an ideal gas and therefore the number density n only depends on the pressure p and the temperature T in the gas. Without any beam current, the target density is described by the ideal gas law:

$$n = \frac{N}{V} = \frac{p}{k_B \cdot T}, \tag{4.8}$$

which includes the Boltzmann constant of $k_B = 1.380648 \cdot 10^{-23}\,\frac{\text{J}}{\text{K}}$. For the target temperature, one assumes $T = (308 \pm 15)\,\text{K}$ with a relative error of $\Delta T/T = 5\%$ (presented by A. Formicola for the d-α-setup at the LUNA Collaboration Meeting 2011). The pressure has been measured with an error of $\Delta p/p = 0.25\%$ (Baratron 626ax). With these initial conditions, the target number density is assumed to be $n = (2.35 \pm 0.12) \cdot 10^{16}\,\frac{1}{\text{cm}^3}$ at a pressure of $p = 1\,\text{mbar}$. The relative error of $\Delta n/n = 5\%$ is dominated by the temperature uncertainty.

Mean Energy Loss

Due to the energy loss, the beam energy constantly decreases with every infinitesimal distance step: $E'_p = E_p - \mathrm{d}E_{loss}$. Therefore, the stopping power $\epsilon_{tot}(E_p)$ is also changing due to its energy dependence (see Figure 4.1).

In a first step, the energy loss at the beam entrance E_p^{loss} and at the calorimeter E_{calo}^{loss} is calculated as follows:

$$\begin{aligned} E_p^{loss} &= \epsilon_{tot}^{lab}(E_p) \cdot l_{target} \cdot n & (4.9)\\ E_{calo} &\approx E_p - E_p^{loss} & (4.10)\\ E_{calo}^{loss} &= \epsilon_{tot}^{lab}(E_{calo}) \cdot l_{target} \cdot n. & (4.11)\\ & & (4.12) \end{aligned}$$

The average energy loss E_{mean}^{loss} in the target chamber is calculated as the arithmetric average of the energy losses:

$$E_{mean}^{loss} = \frac{E_p^{loss} + E_{calo}^{loss}}{2} \tag{4.13}$$

The relative error of the proton beam energy loss $\Delta E_p^{loss}/E_p^{loss} = 6\%$ is dominated by the error of the density Δn and the target length $\Delta l/l$. The relative error of the average energy loss is $\Delta E_{mean}^{loss}/E_{mean}^{loss} = 6\%$.

4.1.3. Beam Heating

Caused by stopping processes of elastic and inelastic collisions on the target atoms, the projectiles in the beam increase the target temperature. This process is called beam heating. Assuming a cylindrical shape of the target chamber, the temperature increase T^{bh} can be approximated as follows [32]:

$$T^{bh} = \frac{I \cdot E_p^{loss}}{l_{target} \cdot 2\pi \cdot \lambda_{heat}} \cdot \ln\left(\frac{d_{chamber}}{d_{beam}}\right) \tag{4.14}$$

with the beam current I, the thermal conductivity $\lambda_{heat}^{Ne} = 0.0493\,\mathrm{W/(m\,K)}$ [24], the target length $l_{target} = (20.2 \pm 0.5)\,\mathrm{cm}$, the chamber diameter $d_{chamber} = (1.8 \pm 0.7)\,\mathrm{cm}$ and beam diameter $d_{beam} = (0.7 \pm 0.3)\,\mathrm{cm}$. In that experiment, the maximal beam heating temperature reached $T^{bh} \approx 23\,\mathrm{K}$. The main uncertainty is the beam heating temperature difference T^{bh}, which has an error of $\frac{\Delta T^{bh}}{T^{bh}} = 40\%$ taken from M. Marta et al. [29]. For the future, there are beam heating measurements planned to obtain a more precise value for the neon target gas and an optimized setup.

After including the beam heating effect, one obtains a slightly lower target density $\tilde{n}$:

$$\tilde{n} = \frac{N}{V} = \frac{p}{k_B \cdot (T + T^{bh})} \tag{4.15}$$

with $\tilde{n}/n \approx 0.93$. The relative error of the number density $\Delta\tilde{n}/\tilde{n} = 5\%$ is still dominated by the error of the temperature sum $\Delta(T + T^{bh})/(T + T^{bh}) = 5\%$.

The beam heating has again an impact on the target number density n and the energy loss E_p^{loss}. The corrections of the beam heating process for these parameters are implemented by iteration of the calculations.

In the following, two iterations have been applied to obtain the correct measurements which take the beam heating effects into account:

$$\begin{array}{lll} \text{Initial parameters:} & n(T) \rightarrow E_p^{loss}(n) \rightarrow I(E_p^{loss}) \rightarrow T^{bh} \rightarrow ... \\ \text{First iteration:} & ... \rightarrow \tilde{n}(T+T^{bh}) \rightarrow \tilde{E}_p^{loss}(\tilde{n}) \rightarrow \tilde{I}(\tilde{E}_p^{loss}) \rightarrow \tilde{T}^{bh} \rightarrow ... \\ \text{Second iteration:} & ... \rightarrow \tilde{\tilde{n}}(T+\tilde{T}^{bh}) \rightarrow \tilde{\tilde{E}}^{loss}(\tilde{\tilde{n}}) \ . \end{array}$$

The corrected parameters change by less than 1% after the second iteration.

4.1.4. Position of Interaction for Narrow Resonances

For the determination of the detection efficiency, the position of interaction has to be known. Approximately, the reactions happen when the beam energy corresponds to the resonance energy. Assuming a linear energy loss, one obtains for the position of interaction:

$$l_{poi} = \frac{l_{target}}{\tilde{\tilde{E}}_{mean}^{loss}} \cdot (E_p^{lab} - E_{res}^{lab}). \tag{4.16}$$

For this position, the detection efficiency can be calculated for the determination of the resonance strength. One has to note the different lengths scale in respect to the effective length of the collimator l_{coll}^{eff} (see Figure 4.2):

$$\mu_{det} = \mu_{det}(x_{det}) \tag{4.17}$$

$$x_{det} = l_{poi} - l_{coll}^{eff} = l_{poi} - (2.5 \pm 0.5)\,\text{cm} \tag{4.18}$$

The big error of the position of interaction has a strong impact on the error of the detection efficiency.

4.2. Spectral Analysis

This section focuses on the analysis of the experimental γ-ray spectra taken from the ^{22}Ne(p,γ)^{23}Na-reaction. In the first place, the contributing laboratory and beam-induced background is evaluated. Afterwards, the statistical methods for the spectral analysis are introduced.

4.2.1. Evaluation of Laboratory Background

For the analysis of the laboratory background, a measurement has been performed for over $t = 168\,\text{ks}$ on 11th March 2012. The laboratory background contains radiation from ^{40}K and the isotopes of the 232-thorium chain and of the 238-uranium chain. There are further isotopes like ^{60}Co and ^{7}Be which can be considered as contaminants in the detector chamber introduced by former experiments. The isotope ^{207}Bi is assumed to originate from the lead castle. In Tables 4.1 - 4.3, all the determined γ-lines, the decay probabilities and the counting rates for the most dominant lines are listed. In Figure 4.3, the γ-ray peaks of the laboratory background are marked in the background spectrum. The physical properties of the isotopes are based on the Evaluated Nuclear Structure Data File (ENSDF) [2].

As one can see in Figure 4.3, the energy range from $E_\gamma = 0\,\text{keV}$ to $220\,\text{keV}$ is not available for the detection of photons due to properties of the HPGe detector. It is a p-type doped germanium crystal which has a relatively thick dead layer. This leads to the missing detection of low energy γ-rays which have already been strongly attenuated in the dead layer.

In the energy region above $220\,\text{keV}$, one sustains a relatively low laboratory background radiation and this range is well suited for the detection of photons from the ^{22}Ne(p,γ)^{23}Na reaction at $E_\gamma = 440\,\text{keV}$ and $1636\,\text{keV}$.

Isotope / Decay Process	Half-life $T_{1/2}$	E$_\gamma$ (keV) / Decay Probability	Rate (cps)
^{228}Ac (β^--decay to ^{228}Th)	6.15 h	338.320 (11.27 %) 911.204 (25.8 %) 964.766 (4.99 %)[1] 968.971 (15.8 %) 1588.20 (3.22 %)[1]	$1.9 \cdot 10^{-3}$
^{224}Ra (α-decay to ^{220}Rn)	3.66 s	240.986 keV (4.1 %)[1]	
^{212}Pb (β^--decay to ^{212}Bi)	10.6 h	238.632 keV (43.6 %)	$3.5 \cdot 10^{-2}$
^{208}Tl (β^--decay to ^{208}Pb)	3.05 min	510.77 keV (22.60 %)[1] 583.187 keV (85.0%) 860.557 keV (12.50 %) 2614.511 keV (99.754 %)	$2.2 \cdot 10^{-3}$ $1.5 \cdot 10^{-3}$

Table 4.1.: Laboratory background by the 232-thorium chain

Isotope / Decay Process	Half-life $T_{1/2}$	E_γ (keV) / Decay Probability	Rate (cps)
^{226}Ra (α-decay to ^{222}Rn)	1600 a	186.211 keV (3.64 %)	
^{214}Pb (β^--decay to ^{214}Bi)	26.8 min	241.995 (7.251 %)[1]	
		295.2228 keV (18.42 %)	$4.2 \cdot 10^{-3}$
		351.9321 keV (35.60 %)	$7.4 \cdot 10^{-3}$
		785.96 keV (1.06 %)	
^{214}Bi (β^--decay to ^{214}Po)	19.9 min	609.320 keV (45.49 %)	$7.3 \cdot 10^{-3}$
		768.35 keV (4.894 %)	
		934.056 keV (3.107 %)	
		1120.294 keV (14.92 %)	$2.1 \cdot 10^{-3}$
		1155.210 keV (1.633 %)	
		1238.122 keV (5.834 %)	
		1280.976 keV (1.434 %)	
		1377.669 keV (3.988 %)	
		1401.515 keV (1.33 %)	
		1407.988 keV (2.394 %)	
		1509.210 keV (2.130 %)	
		1661.274 keV (1.047 %)	
		1729.595 keV (2.878 %)	
		1764.491 keV (15.30 %)	$2.0 \cdot 10^{-3}$
		1847.429 keV (2.025 %)	
		2118.514 keV (1.160 %)	
		2204.059 keV (4.924 %)	
		2447.70 keV (1.548 %)	

Table 4.2.: Laboratory background by the 238-uranium chain

Isotope / Decay Process	Half-life $T_{1/2}$	E_γ (keV) / Decay Probability	Rate (cps)
^{7}Be (β^+-decay to ^{7}Li)	53.22 d	477.6035 keV (10.44 %)	$1.3 \cdot 10^{-3}$
^{60}Co (β^--decay to ^{60}Ni)	1925.28 d	1173.228 keV (99.85 %)	$0.5 \cdot 10^{-3}$
		1332.492 keV (99.9826 %)	$0.5 \cdot 10^{-3}$
^{40}K (β^+-decay to ^{40}Ar)	$1.248 \cdot 10^9$ a	1460.822 keV (10.66 %)	$2.2 \cdot 10^{-3}$
^{207}Bi (β^+-decay to ^{207}Pb)	31.55 a	1063.656 keV (74.5 %)	$0.2 \cdot 10^{-3}$
e+e-		511 keV	$5.9 \cdot 10^{-3}$

Table 4.3.: Laboratory background of other contributors

[1] contribution in the spectrum tentative, because of super-imposed photo peaks

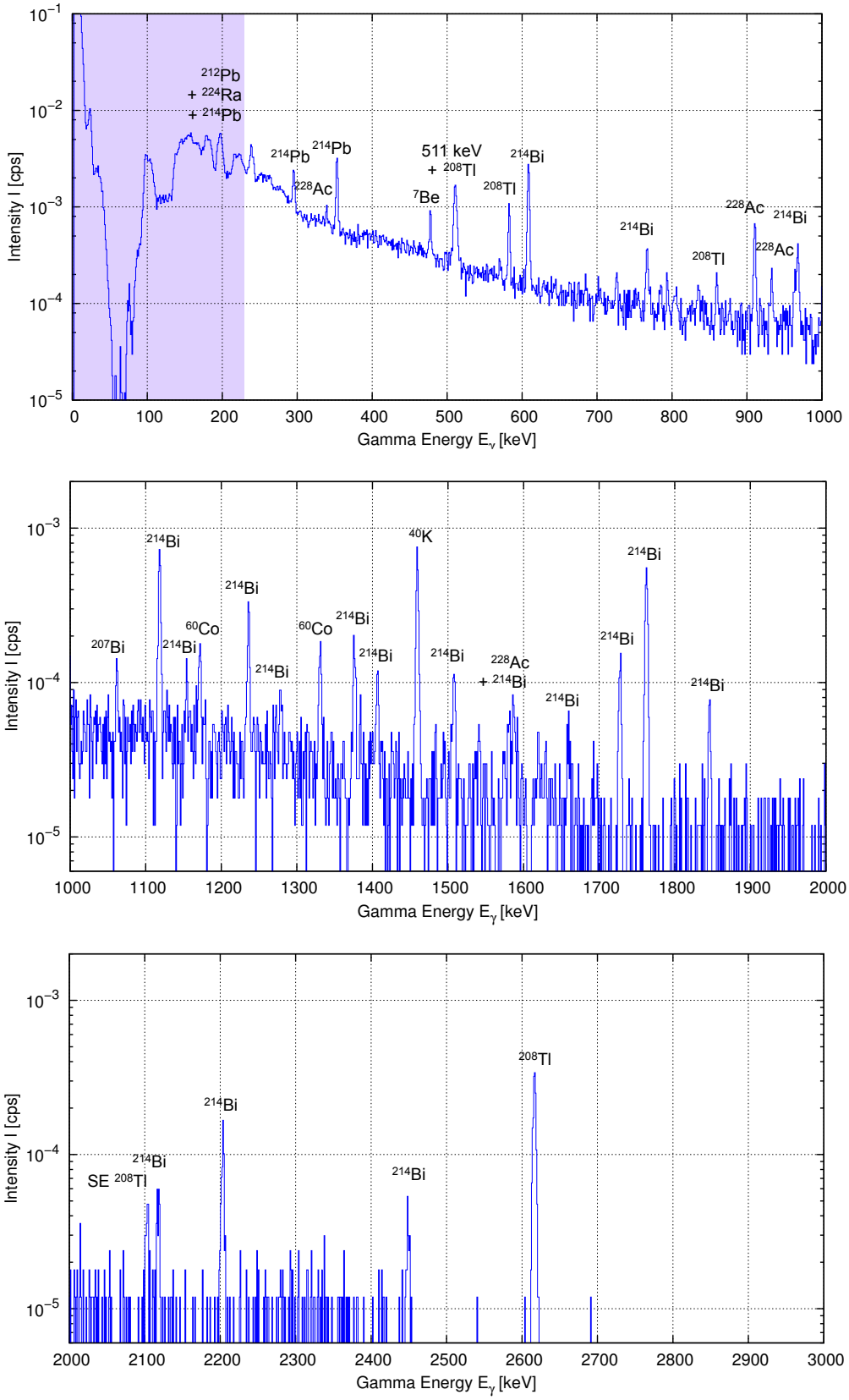

Figure 4.3.: Intensity of laboratory background radiation inside the lead castle. SE stands for single escape.

4.2.2. Evaluation of Beam-Induced Background

The proton beam also causes reactions with nuclei in the target chamber which do not belong to the isotopes of interest. Their gamma ray emissions create the beam-induced background. These nuclei may originate from impurities in the target gas, the oil of the pumps and the heat conducting paste for affixing the calorimeter end cap. In the following, the isotopes from the beam induced background reactions with the most dominant gamma emissions [16] and a representative spectrum in Figure 4.4 are presented:

- The isotope ^{17}F emits $E_\gamma = 495\,\text{keV}$. ^{17}F is created by ^{16}O(p,γ)^{17}F ($Q = 600.27 \pm 0.25\,\text{keV}$). The oxygen is assumed to enter by vacuum leaks.
- The direct capture component DC→0 of ^{12}C(p,γ)^{13}N ($Q = (1943.49 \pm 0.27)\,\text{keV}$) leads to the γ-ray at $E_\gamma = E_p^{lab} + 1944\,\text{keV}$. The oil in the pumping system and the ^{12}C producing reactions are possibly responsible for ^{12}C nuclei in the target gas.
- The isotope ^{12}C emits $E_\gamma = 4439\,\text{keV}$. The ^{12}C isotope is supposed to originate from ^{11}B(p,γ)^{12}C (with $Q = (15956.9 \pm 0.42)\,\text{keV}$) or ^{15}N(p,$\alpha\gamma$)^{12}C ($Q = (4965.493 \pm 0.007)\,\text{keV}$). Boron is an already known contaminant at LUNA and nitrogen might originate from air entering through leaks into the target chamber.
- The direct capture component DC→0 of ^{2}H(p,γ)^{3}He ($Q = 5493.48\,\text{keV}$) emits $E_\gamma = E_p^{lab} + 5494\,\text{keV}$. The ^{2}H nuclei are implanted target gas nuclei from the previous ^{2}H(α,γ)^{6}Li experiment performed in the same setup.
- The isotope ^{16}O emits $E_\gamma = 6130\,\text{keV}$. The ^{16}O nuclei are produced in ^{19}F(p,$\alpha\gamma$)^{16}O ($Q = (12843.52 \pm 0.07)\,\text{keV}$). One assumes fluorine to be an ingredient in the heat conducting paste.

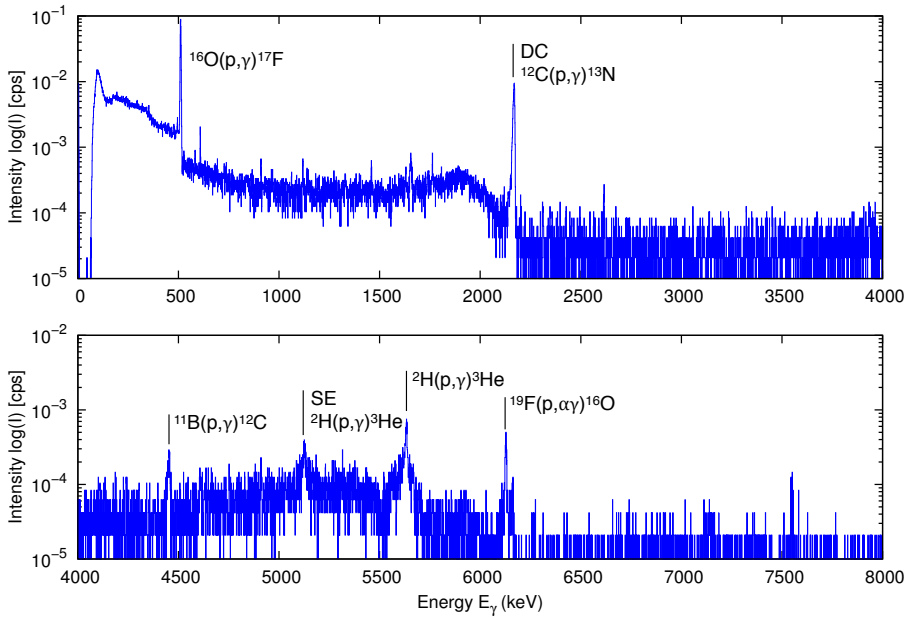

Figure 4.4.: Beam-induced background of the $E_p^{lab} = 258\,\text{keV}$ spectrum. DC stands for direct capture and SE stands for single escape.

4.2.3. Statistical Methods

The statistical analysis of the photon spectra is based on the textbook of Gilmore [10]. The analysis methods take into account the contributions of the laboratory and the beam induced backgrounds.

Figure 4.5 shows an artificial gamma ray spectrum, as it might have been obtained in the previous measurements. It is divided into the signal part and two background parts. The signal region area comprises N_{signal} counts within n_{signal} channels:

$$N_{signal} = \sum_{i=1}^{n_{signal}} N^i_{signal}. \tag{4.19}$$

The background part includes two representative regions in a distance of n_{dist} above and below the signal region. The distance to the signal region should rather be small and the background regions have to be representative without any apparent photon peaks. For every background region, one obtains N_{highBG} counts and N_{lowBG} counts in the same range of n_{BG} channels:

$$N_{highBG} = \sum_{i=1}^{n_{BG}} N^i_{highBG} \quad \text{and} \quad N_{lowBG} = \sum_{i=1}^{n_{BG}} N^i_{lowBG}. \tag{4.20}$$

For a spectrum with significant laboratory and beam-induced background, the spectral analysis takes both contributions into account. In the first step, the corresponding laboratory background is subtracted from the signal N_{signal} and the background regions N_{lowBG} and N_{highBG}.

$$\tilde{N}_{signal} = N_{signal} - N_{labBG,signal} \tag{4.21}$$
$$\tilde{N}_{lowBG} = N_{lowBG} - N_{labBG,lowBG} \tag{4.22}$$
$$\tilde{N}_{highBG} = N_{highBG} - N_{labBG,highBG}. \tag{4.23}$$

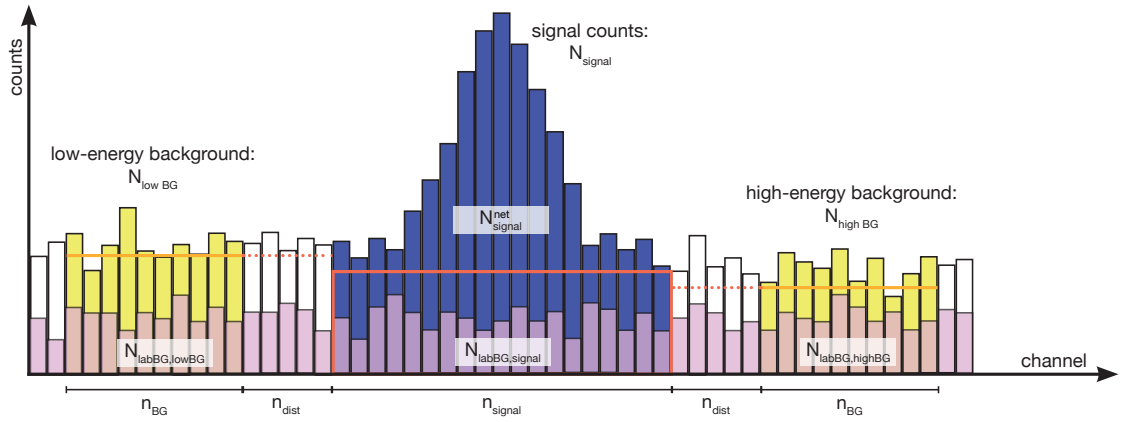

Figure 4.5.: Artificial γ-ray spectrum with the signal and background regions.

The laboratory background and the corresponding errors belong to the long background measurement for $t = 168\,\text{ks}$ on 11th March 2012. Therefore, the laboratory background error has a better statistic than the beam-induced background. Furthermore, any activation during the experiment are assumed to have a negligible impact on the γ-ray spectral regions considered here. In special, the Compton background of the decaying ^{7}Be can be assumed as negligible for the transition at $E_\gamma = 440\,\text{keV}$. The error bars from both background contributions are summed up quadratically.

The average background N_{BGtot} is calculated by the arithmetic average of $\tilde{N}_{lowBG}$ and $\tilde{N}_{highBG}$. The net signal N^{net}_{signal} is obtained by the subtraction of the background contribution $N_{BG,tot}$ from the peak area $\tilde{N}_{signal}$:

$$N_{BGtot} = \frac{n_{signal}}{2 \cdot n_{BG}} \cdot (\tilde{N}_{lowBG} + \tilde{N}_{highBG}) \tag{4.24}$$

$$N^{net}_{signal} = \tilde{N}_{signal} - N_{BGtot}. \tag{4.25}$$

including the signal channels n_{signal} and background channels n_{BG}.

Furthermore, the 2σ-critical limit l_{crit} is introduced [10]. All signals above this threshold are significant with 95% confidence.

$$l_{crit} = 1.645 \cdot \sqrt{N_{BGtot} \cdot \left(1 + \frac{n_{signal}}{2 \cdot n_{BG}}\right)} \tag{4.26}$$

If the net count area is lower than l_{crit}, the upper limit l_{up} for N^{net}_{signal} is derived as follows:

$$l_{up} = \begin{cases} N^{net}_{signal} + 1.645 \cdot \sqrt{N^{net}_{signal} + N_{BGtot} \cdot \left(1 + \frac{n_{signal}}{2 \cdot n_{BG}}\right)} & \text{for } N^{net}_{signal} \geq 0 \\ 1.645 \cdot \sqrt{N_{BGtot} \cdot \left(1 + \frac{n_{signal}}{2 \cdot n_{BG}}\right)} = l_{crit} & \text{for } N^{net}_{signal} < 0. \end{cases} \tag{4.27}$$

Based on the critical limit, one determines the rate R and the experimental yield Y^{exp} similar to their upper limits R_{up} and Y^{exp}_{up} as the following:

$$R = \frac{N^{net}_{signal}}{t} \text{ for } N^{net}_{signal} \geq l_{crit} \tag{4.28}$$

$$R_{up} = \frac{l_{up}}{t} \text{ for } N^{net}_{signal} < l_{crit} \tag{4.29}$$

$$Y^{exp} = \frac{N^{net}_{signal} \cdot e}{t \cdot I} \text{ for } N^{net}_{signal} \geq l_{crit} \tag{4.30}$$

$$Y^{exp}_{up} = \frac{l_{up} \cdot e}{t \cdot I} \text{ for } N^{net}_{signal} < l_{crit} \tag{4.31}$$

including the measuring time t, the current I and the elementary charge e.

5. Results

In this section the characteristic parameters for the observed resonances and the non-resonant part of the ^{22}Ne(p,γ)^{23}Na-reaction are determined. To this end, the yields have to be extracted from the spectra and the setup parameters have to be corrected for beam heating effects. In the following, resonance strengths or their upper limits and the thermonuclear reaction rate are calculated for the nuclear resonances. Furthermore, the S-factor is calculated for one beam energy.

5.1. Resonant Contribution in $^{22}\mathrm{Ne}(\mathrm{p},\gamma)^{23}\mathrm{Na}$

Five nuclear resonances have been analyzed in this paragraph. In the following, the gamma ray spectra are evaluated. Based on these results, the resonance strengths and the thermonuclear reaction rate have been determined.

5.1.1. Analysis of Resonances in the Spectrum

For the spectral analysis of the ^{22}Ne(p,γ)^{23}Na reaction, the signature of two photon transitions of ^{23}Na (Figure 5.1) at $E_\gamma = 440\,\mathrm{keV}$ and $1636\,\mathrm{keV}$ has been observed.

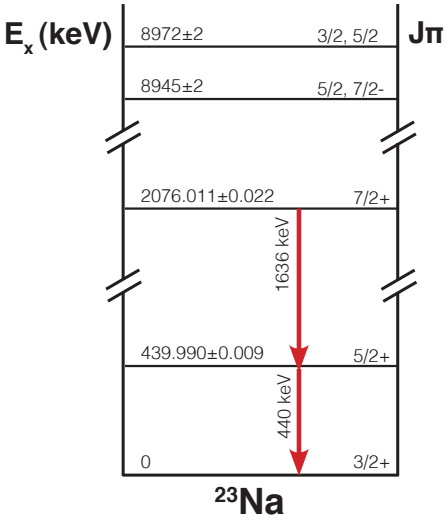

Figure 5.1.: Energy level of ^{23}Na with the photon transition.

- $E_\gamma = 440\,\mathrm{keV}$: 1^{st} excited state $E_x = 440\,\mathrm{keV} \rightarrow$ ground state $E_x = 0\,\mathrm{keV}$
- $E_\gamma = 1636\,\mathrm{keV}$: 2^{nd} excited state $E_x = 2076\,\mathrm{keV} \rightarrow 1^{\mathrm{st}}$ excited state $E_x = 440\,\mathrm{keV}$

Transition at $E_\gamma = 440\,\mathrm{keV}$

The chosen energy ranges of the signal and background regions have to be free of any photon peaks. The upper background region of $E_\gamma = 440\,\mathrm{keV}$ is close to the photon peak of ^{7}Be at $E_\gamma = 477.6\,\mathrm{keV}$, which limits the chosen energy range. In Table 5.1, the regions of interest (ROI) for the signal and the background areas are listed. The distance between background and signal areas is $n_{dist} = 5\,\mathrm{ch}$.

	Low Background	Signal	High Background
ROI (channel number)	401 - 421	437 - 447	453 - 472
n (ch)	20	11	20

Table 5.1.: Region of interest (ROI) and amount of channels in the γ-ray spectrum.

It can be observed, that for higher proton beam energies the photon spectrum is strongly dominated by the beam background. Table 5.2 lists the contribution of the background components and the net signal. The negative fractions for the signal are obtained after applying the analysis methods (paragraph 4.2). They do not have any physical significance.

E_p^{lab}	Beam BG	Laboratory BG	Net Signal
338.83 ± 0.37	95 %	1 %	3 %
329.47 ± 0.37	87 %	2 %	11 %
257.87 ± 0.37	89 %	13 %	-2 %
191.06 ± 0.37	35 %	47 %	17 %
161.89 ± 0.37	41 %	57 %	2 %

Table 5.2.: Contribution of laboratory and beam-induced backgrounds (BG) and the net signal at different proton beam energies E_p^{lab} for $E_\gamma = 440\,\mathrm{keV}$ yield.

After applying background corrections, as presented in paragraph 1.4, the counts in the signal region can be determined as shown in Table 5.3. The upper limits correspond to 2σ confidence. One has to note, that for $E_{res}^{lab} = 323$, a background peak at $E_{gamma}^{lab} = 438\,\mathrm{keV}$, which might originate from statistics is inside the signal area. Consequently, the upper limit for the yield for this resonances is overestimated.

E_p^{lab} (keV)	E_{res}^{lab} (keV)	t (s)	N_{signal}^{net} (cts)	Y
338.83 ± 0.37	334 ± 3	11215.12	≤ 157	$2.0{\cdot}10^{-17}$
329.47 ± 0.37	323 ± 3	3142.03	≤ 70	$3.3{\cdot}10^{-17}$
257.87 ± 0.37	256 ± 1	47974.66	≤ 54	$1.5{\cdot}10^{-18}$
191.06 ± 0.37	186 ± 3	45685.48	44 ± 18	$(1.4 \pm 0.6)\cdot10^{-18}$
161.89 ± 0.37	159 ± 3	48847.14	≤ 23	$6.8{\cdot}10^{-19}$

Table 5.3.: Runs of different proton beam energies E_p^{lab} with the populated resonance E_{res}^{lab}, the measuring time t, the signal counts N_{signal}^{net} and the yield Y for $E_\gamma = 440\,\mathrm{keV}$ transition.

In the following figures, representative spectra parts for selected resonances of the ^{22}Ne(p,γ)^{23}Na reaction are shown. The signal originates from the transition emitting a photon at $E_\gamma = 440\,\text{keV}$. Furthermore, the lower and upper background regions as well as the laboratory background contribution are marked.

The nuclear resonance at $E_{res}^{lab} = 186\,\text{keV}$ (populated by a beam energy of $E_p^{lab} = 191\,\text{keV}$) has a significant signal for the transition of the first excited state to ground state with a confidence of $> 95\%$. The spectra of this resonance in the region of the gamma ray emission is shown in Figure 5.2.

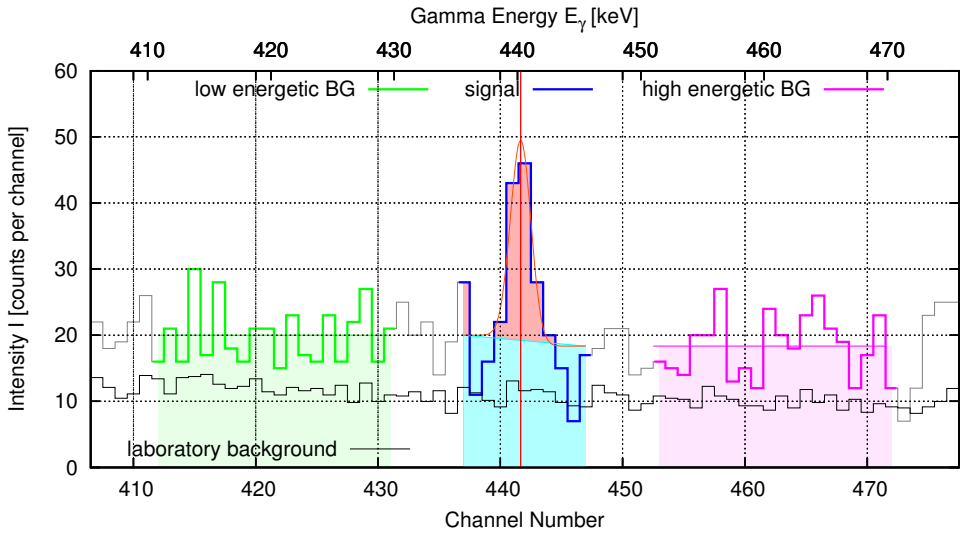

Figure 5.2.: γ-spectrum of $E_{res}^{lab} = 186\,\text{keV}$ with ROI centered at $E_\gamma = 440\,\text{keV}$.

The signal from the $E_\gamma = 440\,\text{keV}$-line (see Figure 5.2) of the resonance at $E_{res}^{lab} = 334\,\text{keV}$ (populated by a beam energy of $E_p^{lab} = 339\,\text{keV}$) can not be detected due to the large beam induced background.

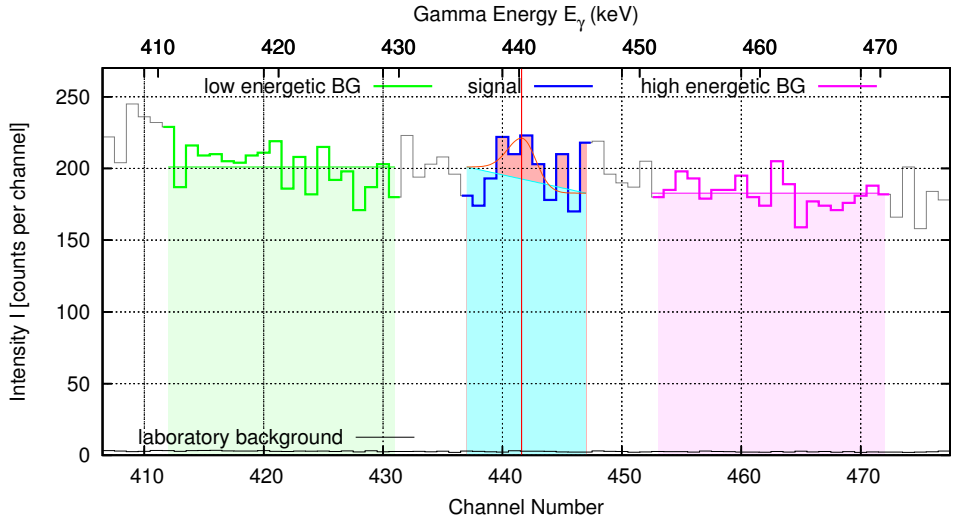

Figure 5.3.: γ-spectrum of $E_{res}^{lab} = 334\,\text{keV}$ with ROI centered at $E_\gamma = 440\,\text{keV}$.

Transition at $E_\gamma = 1636\,\text{keV}$

The chosen regions of interest for the $E_\gamma = 1636\,\text{keV}$ transition are listed in Table 5.4. There is a background peak caused by $^{19}\text{F(p,}\gamma)^{20}\text{Ne}$ at $E_\gamma = 1633\,\text{keV}$. Consequently, the region of interest has been adapted. The distance between signal and peak regions is $n_{dist} = 6\,\text{ch}$.

	Low Background	Signal	High Background
ROI (channel number)	1617 - 1631	1639 - 1646	1652 - 1666
n (ch)	15	8	15

Table 5.4.: Region of interest (ROI) and amount of channels in the γ-ray spectrum.

One has to note, that for $E_{res}^{lab} = 258\,\text{keV}$ a strong background at $E_\gamma = 1664\,\text{keV}$ (probably from the single escape of $^{12}\text{C(p,}\gamma)$) dominates the spectra. Consequently, the distance to the upper and lower background region has been set to $n_{dist} = 25\,\text{ch}$.

As one can see in Table 5.5, the laboratory background dominates at low beam energies, whereas the beam-induced background dominates at high beam energies.

E_p^{lab}	Beam BG	Laboratory BG	Net Signal
338.83 ± 0.37	86 %	1 %	13 %
329.47 ± 0.37	86 %	2 %	12 %
257.87 ± 0.37	82 %	7 %	11 %
191.06 ± 0.37	17 %	16 %	67 %
161.89 ± 0.37	32 %	33 %	34 %

Table 5.5.: Contribution of backgrounds (BG) and the net signal area (Net Signal) at the $E_\gamma = 1636\,\text{keV}$ peak for different proton beam energies E_p^{lab}.

For the observed transition from the second excited state to first excited state, the final counts in the net signal area are listed in the following table. The spectra for $E_{res}^{lab} = 159\,\text{keV}$ is attached in the Appendix (see Figure A.7).

E_p^{lab} (keV)	E_{res}^{lab} (keV)	t (s)	N_{signal}^{net} (cts)	Y
338.83 ± 0.37	334 ± 3	11215.12	≤ 48	$\leq 6.1{\cdot}10^{-18}$
329.47 ± 0.37	323 ± 3	3142.03	≤ 8	$\leq 4.0{\cdot}10^{-18}$
257.87 ± 0.37	256 ± 1	47974.66	≤ 17	$\leq 4.5{\cdot}10^{-19}$
191.06 ± 0.37	186 ± 3	45685.48	26 ± 7	$(8.0 \pm 2.0){\cdot}10^{-19}$
161.89 ± 0.37	159 ± 3	48847.14	7 ± 5	$(2.0 \pm 1.4){\cdot}10^{-19}$

Table 5.6.: Runs of different proton beam energies E_p^{lab} with the populated resonance E_{res}^{lab}, the measuring time t, the signal counts N_{signal}^{net} and the yield Y for $E_\gamma = 1636\,\text{keV}$ transition.

The following tables present characteristic spectra for the transition at $E_\gamma = 1636\,\text{keV}$. In the γ-ray spectra of the resonance $E_{res}^{lab} = 191\,\text{keV}$ (see Figure 5.4), the signal for the γ-ray transition can be determined with a confidence level of 95%.

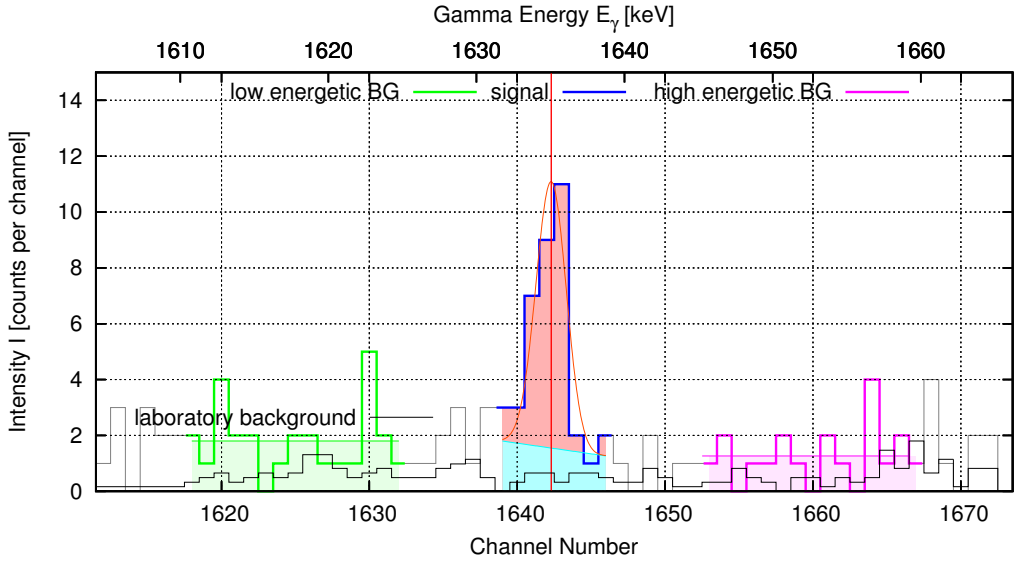

Figure 5.4.: γ-spectrum of $E_{res}^{lab} = 186\,\text{keV}$ with ROI centered at $E_\gamma = 1636\,\text{keV}$.

The γ-ray spectrum for the resonance $E_{res}^{lab} = 334\,\text{keV}$, shows no significant signal. Furthermore, there is a background at channel 1640, which might be caused by statistics. Only an upper limit which probably overestimate the true yield can be derived for the net counts in the signal area.

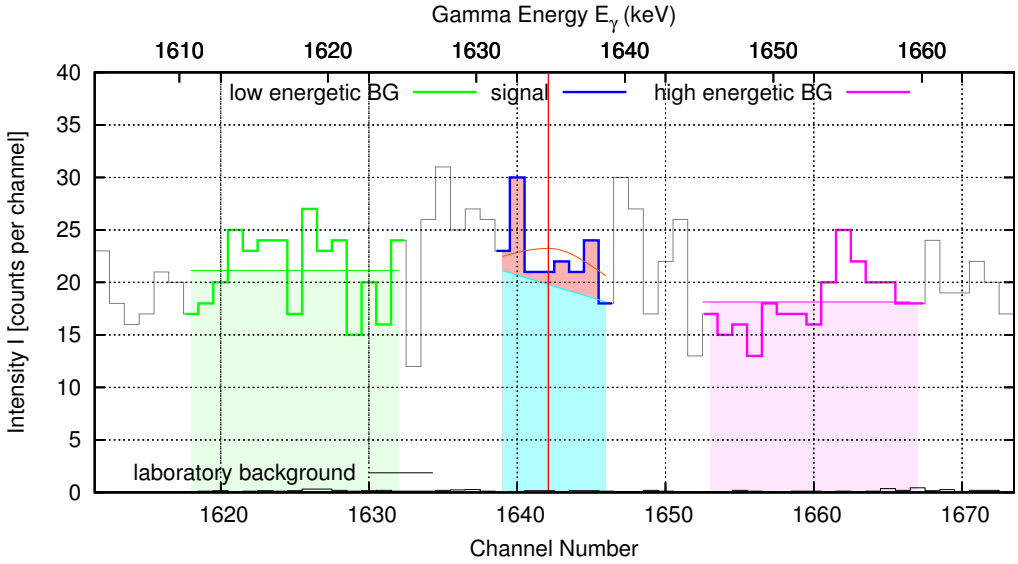

Figure 5.5.: γ-spectrum of $E_{res}^{lab} = 334\,\text{keV}$ with ROI centered at $E_\gamma = 1636\,\text{keV}$.

5.1.2. Resonance Strengths

The resonance strength $\omega\gamma$ is a characteristic parameter of nuclear resonances (see paragraph 1.4.6). It contains the information of the spins of the contributing particles and the widths of the reaction channels.

For the following considerations, the resonance strength $\omega\gamma^{E_\gamma}$ is introduced. It represents the resonance strength which has been calculated by using the experimental yield of a special γ-ray energy ($E_\gamma = 440\,\mathrm{keV}$ or $E_\gamma = 1636\,\mathrm{keV}$). One obtains:

$$\omega\gamma^{E_\gamma} = \frac{\omega\gamma}{M_{dec}(E_\gamma)} = \frac{2 \cdot Y^{E_\gamma} \cdot \epsilon_{eff}^{cm}}{\lambda_B^2 \cdot \mu_{det}}. \tag{5.1}$$

including the branching ratio $M_{dec}(E_\gamma)$, the de-Broglie wavelength $\lambda_B(E_{res}^{cm})$, the experimental yield Y^{E_γ}, the effective stopping ϵ_{eff}^{cm} and the detection efficiency μ_{det}.

For obtaining the real resonance strength which does not depend on a single photon transition yield, the decay probability μ_{dec} of the observed excited states has to be considered. This measure describes the probability that the transition cascade of a higher energetic state will also include the transition between two energy levels at an energy of E_γ. The resonance strength $\omega\gamma$ for a nuclear resonance is calculated as follows:

$$\omega\gamma = \frac{\omega\gamma^{E_\gamma}}{\mu_{dec}}. \tag{5.2}$$

The decay probability for the transition of $E_\gamma = 440\,\mathrm{keV}$ is assumed to be $\mu_{dec} = 1$. According to [8], the known decay probabilities of neighboring resonances are also in the range of $\mu_{dec} = 0.97 - 1$. The decay probability for the transition of $E_\gamma = 1636\,\mathrm{keV}$ is not known. Based on this assumptions, the "real" resonance strengths used for following calculations are calculated with $\omega\gamma^{440}$ and $\mu_{dec} = 1$.

The relative error of the resonance strength is given by:

$$\frac{\Delta\omega\gamma}{\omega\gamma} = \sqrt{\left(\frac{\Delta E_{res}^{cm}}{E_{res}^{cm}}\right)^2 + \left(\frac{\Delta\epsilon_{eff}^{cm}}{\epsilon_{eff}^{cm}}\right)^2 + \left(\frac{\Delta\mu_{det}}{\mu_{det}}\right)^2 + \left(\frac{\Delta Y}{Y}\right)^2 + \left(\frac{\Delta\mu_{dec}}{\mu_{dec}}\right)^2}. \tag{5.3}$$

The dominant error is caused by the error of the detection efficiency $\Delta\mu_{det}$ due to the big error of the position of interaction Δl_{poi} (see paragraph 3.4.2 and 4.1.4). Furthermore, the yield Y also has a big uncertainty for resonances with a significant signal for E_γ. The decay probability is assumed to have no error.

In Table 5.7, the resonance strengths for the transitions at $E_\gamma = 440\,\text{keV}$ and $E_\gamma = 1636\,\text{keV}$ are listed. For the resonances at $E_{res}^{lab} = 186\,\text{keV}$ and $E_{res}^{lab} = 323\,\text{keV}$ a significant signal could be obtained at the transition energy of $E_\gamma = 440\,\text{keV}$. For the transition at $E_\gamma = 1636\,\text{keV}$, a significant signal has been determined for $E_{res}^{lab} = 159\,\text{keV}$ and $E_{res}^{lab} = 186\,\text{keV}$. For all the other resonances, only upper limits for the resonance strength could be evaluated from the data.

E_p^{lab} (keV)	E_{res}^{lab} (keV)	$\omega\gamma^{440}$ (eV)	$\omega\gamma^{1636}$ (eV)
338.8 ± 3.0	333.5 ± 3.1	$\leq 9{\cdot}10^{-6}$	$\leq 3{\cdot}10^{-6}$
329.5 ± 3.0	323.0 ± 3.1	$\leq 1.1 \cdot 10^{-5}$	$\leq 1.3{\cdot}10^{-6}$
257.9 ± 1.0	255.8 ± 1.0	$\leq 5 \cdot 10^{-7}$	$\leq 1.5{\cdot}10^{-7}$
191.1 ± 3.0	186.0 ± 3.1	$(2.0\ ^{+1.6}_{-0.9}) \cdot 10^{-7}$	$(1.2\ ^{+0.9}_{-0.3}) \cdot 10^{-7}$
161.9 ± 3.0	158.9 ± 3.1	$\leq 1.7{\cdot}10^{-7}$	$(2.9\ ^{+0.3}_{-0.2}) \cdot 10^{-8}$

Table 5.7.: Runs at proton beam energies E_p^{lab} with the populated resonances E_{res}^{lab} and the resonance strengths $\omega\gamma$ for the $E_\gamma = 440\,\text{keV}$ and $E_\gamma = 1636\,\text{keV}$ transition.

5.1.3. Thermonuclear Reaction Rate of Resonances

Based on the resonance strengths, one can calculate the thermonuclear reaction rate (TNRR) $N_A < \sigma\nu >_{res}$ for the resonances of the ^{22}Ne(p,γ)^{23}Na reaction [16]:

$$N_A < \sigma\nu >_{res} = \frac{1.5399 \cdot 10^{11}}{\left(\frac{\tilde{M}_T + \tilde{M}_P}{\tilde{M}_T \cdot \tilde{M}_P} \cdot \tilde{T}_9\right)^{3/2}} \cdot \Sigma_i(\widetilde{\omega\gamma})_i \cdot e^{-11.605 \cdot \tilde{E}^{cm}_{res}/\tilde{T}_9} \text{ (in cm}^3\,\text{mol}^{-1}\,\text{s}^{-1}\text{)} \quad (5.4)$$

including the temperature $\tilde{T}_9$ in GK, the resonance energy $\tilde{E}^{cm}_{res}$ in MeV, the masses $\tilde{M}$ in u and the resonance strength $\widetilde{\omega\gamma}$ in MeV.

In Table 5.6, the TNRR of the resonances has been determined with the resonance strengths for the transition at $E_\gamma = 440\,\text{keV}$ assuming a decay probability of $\mu_{dec} = 1$. According to the measured data, upper limits have been determined for $E^{lab}_{res} = 158\,\text{keV}$, 255 keV, 323 keV and 333 keV. Furthermore, a significant TNRR with error bars has been calculated for $E^{lab}_{res} = 186\,\text{keV}$. As the decay probability of the $E_\gamma = 1636\,\text{keV}$ transition is not known, the TNRR of the resonance cannot be calculated based on their resonance strength.

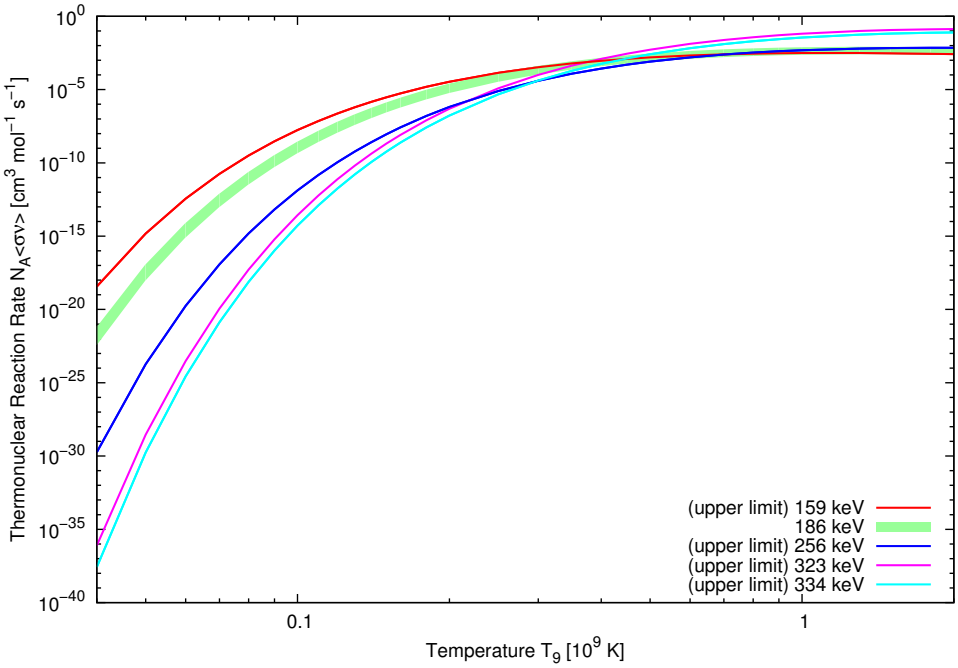

Figure 5.6.: Thermonuclear reaction rates for the analyzed resonances.

One has to note, that the calculated TNRR only includes the contribution of the resonant part $N_A < \sigma\nu >$. The tail distribution as presented in [4] has a negligible impact on the total thermonuclear reaction rate.

5.2. Non-Resonant Contribution in ^{22}Ne(p,γ)^{23}Na

The cross-section of charged particle induced reactions can be expressed by the astrophysical S-Factor (see paragraph 1.4.5). For the determination of a non-resonant S-factor component, the direct capture process DC $\rightarrow$ 440 of the run at $E_p^{lab} = 360\,\text{keV}$ has been selected. No resonances of ^{23}Na are assumed to be situated in the energy range corresponding to the proton beam energy of $E_p^{lab} = 360\,\text{keV}$ and the associated energy loss $[E_p^{lab} - E_{mean}^{loss};\, E_p^{lab}]$.

For the calculation of the cross-section of the DC $\rightarrow$ 440 process, one assumes a proton of an arbitrary energy to populate the first energetic level at $E_x = 440\,\text{keV}$ of ^{23}Na. This population is followed by a transition to the ground state and a photon emission at $E_\gamma = 440\,\text{keV}$. The determination of the effective cross-section for DC $\rightarrow$ 440 is based on the yield of the $E_\gamma = 440\,\text{keV}$ peak, which corresponds to the transition from the first excited level to the ground state:

$$\tilde{\sigma} = \frac{Y^{440}}{\mu_{det}} \tag{5.5}$$

including the detection efficiency μ_{det} of the HPGe-detector.

Due to the fact that the contribution of higher energetic state to the 440 $\rightarrow$ 0 transition is unknown (see Figure 5.7), the S-factor measured at LUNA will overestimate the S-factor for the single DC $\rightarrow$ 440 process.

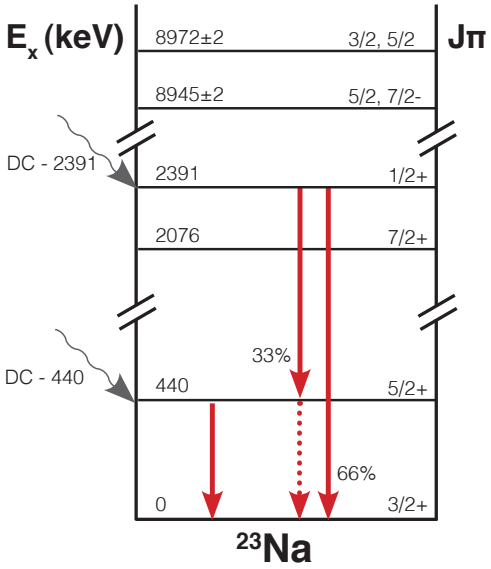

Figure 5.7.: Direct capture processes and transitions between the levels [8]. Additional contribution to DC $\rightarrow$ 440 by higher energetic level cascades (dashed lines).

Based on the cross-section σ for the $E_\gamma = 440\,\mathrm{keV}$ transition, one can calculate the S-factor:

$$\tilde{S}^{440}_{E_p^{lab}} = \tilde{\sigma} \cdot \epsilon_{eff} \cdot \frac{m_{^{22}Ne}}{m_{^{22}Ne} \cdot m_p} \cdot \left(\int_{E_p^{lab}-E_{loss}}^{E_p^{lab}} \frac{e^{-31.29 \cdot Z_{^{22}Ne} \cdot \sqrt{m_p / E_p^{lab}}}}{E_p^{lab}} \, \mathrm{d}E \right)^{-1} \tag{5.6}$$

including the effective stopping ϵ_{eff}, the proton energy E_p^{lab}, the beam energy loss E_{loss} and the atomic masses m.

Based on the measured parameters listed in Table 5.8, an upper limit for the S-factor of the DC $\rightarrow$ 440 process has been determined at a proton energy of $E_p^{lab} = 360\,\mathrm{keV}$:

$$\tilde{S}^{440}_{360\,\mathrm{keV}} \quad = \quad \leq 33\,\mathrm{keV\,barn}. \tag{5.7}$$

E_p^{lab} (keV)	t (s)	Y	ϵ ($\mathrm{keV\,cm^{-2}}$)	E_{mean}^{loss} (keV)
359.97 ± 0.37	1242	$\leq 1.25 \cdot 10^{-16}$	$(1.2 \pm 0.1) \cdot 10^{-17}$	14.31 ± 0.43

Table 5.8.: Measurement parameters (yield Y and energy loss E_{mean}^{loss}) for the determination of the S-factor.

6. Discussion

In this section, the results of the nuclear network calculation in novae are presented. Furthermore, the outcome of the experiments performed at LUNA II are compared with previous research experiments on the ^{22}Ne(p,γ)^{23}Na reaction. Finally, the uncertainties of the results and possible future improvements are evaluated.

6.1. Nuclear Network Calculations for Novae

The performed network calculation with the libnucnet code in novae show the importance of the ^{22}Ne(p,γ)^{23}Na reaction in the first part of the nova outburst. During the rise of temperature, the entire ^{22}Ne is processed via proton capture and contributes most to the abundance of ^{20}Ne via ^{23}Na(p,α)^{20}Ne. Consequently, the production of ^{22}Mg and ^{23}Mg is supported. As the entire ^{22}Ne cannot be reproduced sufficiently fast by the slow β^+-decay of ^{22}Na, its contribution to the nucleosynthesis is rather negligible after reaching the peak temperature of the nova. It is the one of the first reactions breaking down within the neon-sodium cycle in a nova environment.

Furthermore, the calculations show a strong temperature dependence of the ^{22}Ne(p,γ)^{23}Na reaction in regard to the processing of ^{22}Ne. For the calculation with a nova peak temperature of $T = 0.2\,\mathrm{GK}$ nearly no change in abundance of ^{22}Ne is obvious, whereas at higher temperatures the processing evolves quite strongly.

The final abundances of the nova elements show a significant enhancement of intermediate mass elements. One has calculated, that changes in the thermonuclear reaction rate (TNRR) of ^{22}Ne(p,γ)^{23}Na influence the abundances of elements in the mass range of $A = 12 - 36$. As the TNRR of ^{22}Ne(p,γ)^{23}Na still has strong uncertainties in the temperature range of $0.03 - 0.3\,\mathrm{GK}$, one can assume that improvements of the resonance strengths in the corresponding energy range might have a strong impact on the final element abundance.

6.2. Resonance Strength

The resonance strengths obtained by the measurements at LUNA and previous measurements of Görres et al. [13, 11], Hale et al. [14] and Iliadis et al. [17] are listed in Table 6.1. The strengths of LUNA are based on the transition of $E_\gamma = 440$ assuming a decay probability of $\mu_{dec} = 1$ (see paragraph 5.1.2).

E_{res}^{lab} (keV)	$\omega\gamma^{440}$ (eV)	$\omega\gamma^{1636}$ (eV)	$\omega\gamma_{Goerres}$ (eV)	$\omega\gamma_{Hale}$ (eV)	$\omega\gamma_{Iliadis}$ (eV)
333.5 ± 3.1	$\leq 9 \cdot 10^{-6}$	$\leq 3 \cdot 10^{-6}$	$\leq 3.00 \cdot 10^{-6}$	Görres	Görres
323.0 ± 3.1	$\leq 1.1 \cdot 10^{-5}$	$\leq 1.3 \cdot 10^{-6}$	$\leq 2.20 \cdot 10^{-6}$	Görres	Görres
255.8 ± 1.0	$\leq 5 \cdot 10^{-7}$	$\leq 1.5 \cdot 10^{-7}$	$\leq 2.60 \cdot 10^{-6}$	$\leq 1.30 \cdot 10^{-7}$	Hale
186.0 ± 3.1	$(2.0^{+1.6}_{-0.9}) \cdot 10^{-7}$	$(1.2^{+0.9}_{-0.3}) \cdot 10^{-7}$	$\leq 2.60 \cdot 10^{-6}$	Görres	Görres
158.9 ± 3.1	$\leq 1.7 \cdot 10^{-7}$	$(2.9^{+0.3}_{-0.2}) \cdot 10^{-8}$	$6.50 \cdot 10^{-7}$	$\leq 9.20 \cdot 10^{-9}$	Hale

Table 6.1.: Resonances of ^{22}Ne(p,γ)^{23}Na with resonance strengths from LUNA, Görres [13], Hale [14] and Iliadis [17].

For the resonances at $E_{res}^{lab} = 333.5\,\text{keV}$ and $E_{res}^{lab} = 323\,\text{keV}$, the upper limits of LUNA do not go below the upper limit of Görres et al. due to the beam induced background. This is consistent with previous publications.

The resonances at $E_{res}^{lab} = 255.8\,\text{keV}$ has been measured with a lower upper limit compared to Görres. But these upper limit still exceeds the indirect upper limit of the evaluation of Hale et al. The result is consistent with previous papers and represents the lowest resonance strength in a direct measurement until now.

The γ-ray transitions in the nuclear resonance at 186 keV has been determined with a significant signal. One obtains a resonance strength of $\omega\gamma = (2.0\,^{+1.6}_{-0.9}) \cdot 10^{-7}$. One has to point out, that this resonance has not been measured directly before and this is the first significant signal observed. The result is consistent with previous publications.

For the resonance at $E_{res}^{lab} = 158.9\,\text{keV}$, the LUNA data show an upper limit which is below the signal of [11], but still above the measurements of [14]. Taking into account the resonance strength $\omega\gamma^{1636}$, the limit of [14] might be set too low.

6.3. Thermonuclear Reaction Rate of Resonances

The values for the resonance strengths obtained by LUNA have been used for the calculation of the thermonuclear reaction rate of ^{22}Ne(p,γ)^{23}Na. For the resonances which have not been studied, the values of a) the European Compilation of Reaction Rates for Astrophysics (NACRE) [4] b) Hale et al. [14] and c) the compilation of Iliadis et al. [17] have been used.

6.3.1. NACRE Compilation

The NACRE Compilation [4] lists 55 resonances in the range of $E_{res}^{lab} = 36 - 1822\,\mathrm{keV}$. The upper limits for the two tentative state at $E_{res}^{lab} = 71\,\mathrm{keV}$ and $E_{res}^{lab} = 104\,\mathrm{keV}$ are included as values multiplied by a factor 0.1. The resonance strengths presented in this work have been inserted in the resonances at $E_{res}^{lab} = 159\,\mathrm{keV}, 186\,\mathrm{keV}$ and $256\,\mathrm{keV}$.

In Figure 6.1, the adopted reaction rate of the NACRE compilation and the new calculated reaction rate with the LUNA resonances are plotted. The rate with the implemented LUNA measurement shows a different behavior in the temperature region of $T \approx 0.1 - 0.3\,\mathrm{GK}$ due to the preciously listed resonances.

6.3.2. Hale

For the recommended rate of Hale et al. [14], the contribution from the direct-capture, the resonance $E_{res}^{lab} = 36\,\mathrm{keV}$ and all resonances for $E_{res}^{lab} \geq 436\,\mathrm{keV}$ have been considered. Furthermore, the upper limits for the resonance strengths for the resonances $E_{res}^{lab} = 159\,\mathrm{keV}$ and $186\,\mathrm{keV}$ are used as values, weighted by a factor 0.1. The tentative resonances at $E_{res}^{lab} = 71\,\mathrm{keV}$ and $104\,\mathrm{keV}$ have been disregarded.

For the new calculation of the reaction rate, only the resonance strength for $E_{res}^{lab} = 186\,\mathrm{keV}$ from LUNA has been implemented. For the other resonances lower upper limits have been determined by [14] in comparison to LUNA. Figure 6.1 shows the adopted rate from the Hale publication as well as the rate with implemented resonance strength from LUNA. One can see a deviation of the LUNA based rate in the temperature range of $T = 0.09 - 0.25\,\mathrm{K}$.

6.3.3. Iliadis Compilation

The physics input data in the Iliadis compilation [17] contains the re-evaluated resonance strengths from previous experiments as mentioned in paragraph 1.2.3. In this compilation, 47 resonances are determined by significant resonance strengths and 8 resonances have upper limits. Based on this input data, the thermonuclear reaction rates are calculated by Monte-Carlo simulations [28, 18].

For the new calculation of the reaction rate with the starlib Nucleosynthesis Simulator [19], the resonance at $E_{res}^{lab} = 186$ measured at LUNA has been newly implemented in the physics input data. In the previous dataset, its resonance strength has been evaluated by an upper limit. All the other resonances observed by LUNA have been measured with a lower upper limit by [17]. In Figure 6.2, the previous and the new calculated reaction

rate are presented. One can see the lowered reaction rate in the temperature scale of $T \approx 0.1 - 0.2\,\mathrm{GK}$.

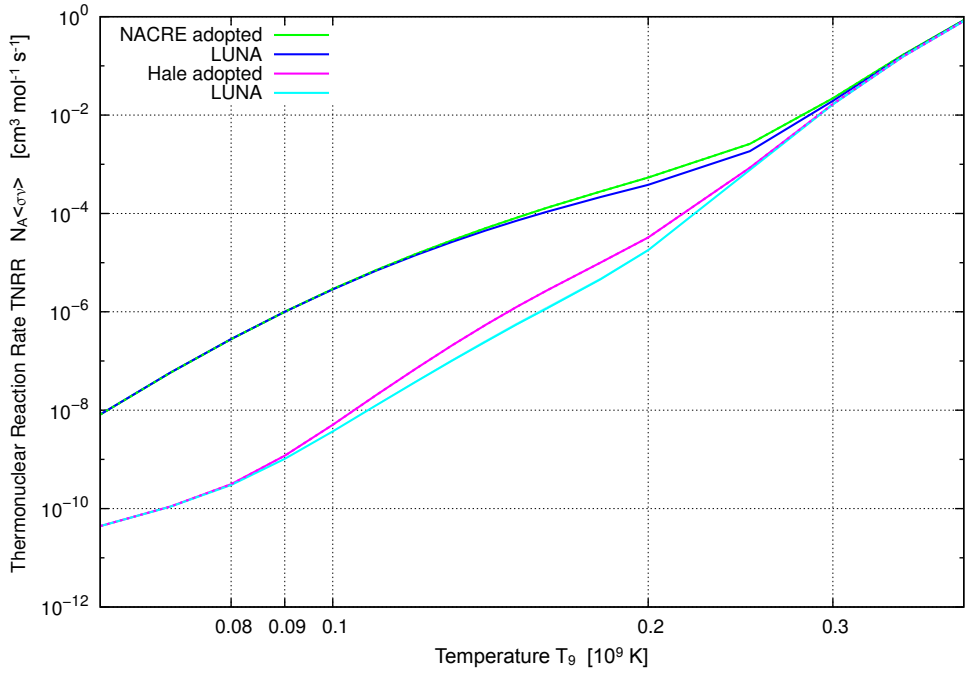

Figure 6.1.: Adopted thermonuclear reaction rate of NACRE [4] and Hale et al. [14] and the implemented resonance strengths from the measurements at LUNA.

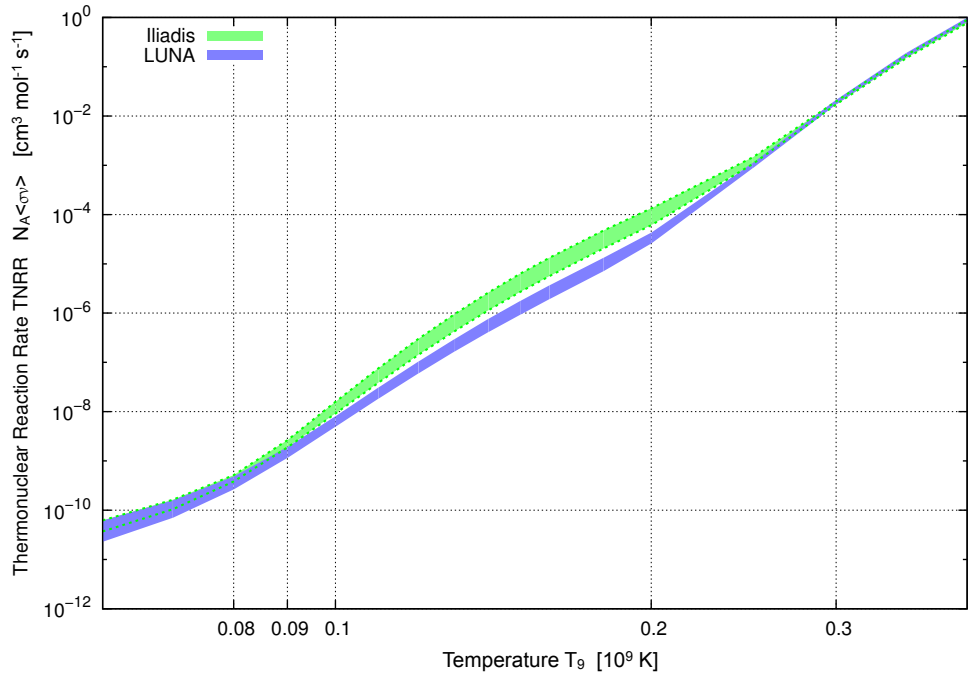

Figure 6.2.: Thermonuclear reaction rate (with error region) of Iliadis [19] with implemented resonance strengths from measurements at LUNA.

6.3.4. Comparison

For a better visualization of the impact of the LUNA measurements, Figure 6.3 shows the ratio of the new calculated thermonuclear reaction rates of Hale or Iliadis, respectively and the NACRE compilation.

In the temperature range of $T = 0.03 - 0.3\,\mathrm{GK}$, which corresponds to the resonances at $E_{res}^{lab} = 71 - 256\,\mathrm{keV}$, the thermonuclear reaction rates of Hale and Iliadis show a strong difference to the NACRE compilation. At $T = 0.09\,\mathrm{GK}$, the reaction rates differ by a factor of $f \sim 100$.

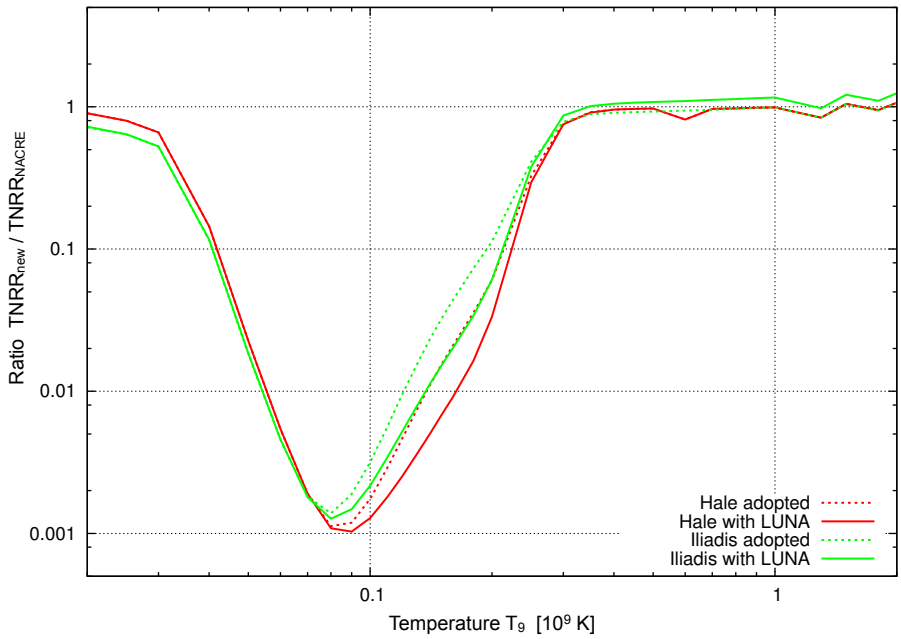

Figure 6.3.: Ratio of thermonuclear reaction with implemented resonance strengths from LUNA and the NACRE compilation as baseline.

This can be explained by the measured upper limits of resonance strengths and the existence of tentative states which create a strong uncertainty of the ^{22}Ne(p,γ)^{23}Na-rate in a resonance energy range of $E_{res}^{lab} = 71 - 256\,\mathrm{keV}$.

One has to note, that for the calculation of the thermonuclear reaction rate of Hale et al. and Iliadis et al. the contributions of the resonance strengths have been newly evaluated. In contrast to NACRE, only the contributions from $E_{res}^{lab} = 37, 71, 104\,\mathrm{keV}$ and $E_{res}^{lab} \geq 436\,\mathrm{keV}$ are taken into account by Hale. Additionally, the values of the upper limits for the resonance strengths for the resonances $E_{res}^{lab} = 158$ and $186\,\mathrm{keV}$ are multiplied by a factor of 0.1. Iliadis even disregards the resonances at $E_{res}^{lab} = 71$ and $104\,\mathrm{keV}$.

Table 6.2 lists selected resonances of ^{23}Na with their Gamov energy and the resonance strengths measured in the current and previous experiments. These resonances belong to the temperature range which shows a strong uncertainty in the reaction rate. For future measurements, one should amongst others determine significant values for the resonance strength of $E_{res}^{lab} = 159$ and 256 keV, which are still measured by upper values. Furthermore, it is important to clarify the presence of the resonances $E_{res}^{lab} = 71, 104$ and 215 keV which are still considered as tentative by [17].

E_{res}^{lab} (keV)	T_{Gamov} (10^9 K)	$\omega\gamma_{Goerres}$ (eV)	$\omega\gamma_{Hale}$ (eV)	$\omega\gamma_{Iliadis}$ (eV)	$\omega\gamma_{LUNA}$ (eV)
71	0.04	$(\leq 4.2 \cdot 10^{-9})$	$(\leq 1.9 \cdot 10^{-10})$	disregarded	-
104	0.08	$(\leq 6.0{\cdot}10^{-7})$	$(\leq 1.4{\cdot}10^{-7})$	disregarded	-
159 ± 3	0.14	$6.5{\cdot}10^{-7}$	$\leq 9.2{\cdot}10^{-9}$	Hale	$\leq 1.7 \cdot 10^{-7}$
186 ± 3	0.18	$\leq 2.6{\cdot}10^{-6}$	Görres	Görres	$2.0 \cdot 10^{-7}$
215	0.22	$(\leq 1.4{\cdot}10^{-6})$	Görres	disregarded	-
256 ± 1	0.30	$\leq 2.6{\cdot}10^{-6}$	$\leq 1.3{\cdot}10^{-7}$	Hale	$\leq 5 \cdot 10^{-7}$

Table 6.2.: Energy level with resonance strengths from Görres et al., Hale et al. and Iliadis et al. The resonance strengths in brackets indicate tentative states.

According to the proton beam energy range of LUNA, the resonances within $E_{res}^{lab} = 100 - 400$ keV (see paragraph 3.1) can be populated. But some of the present upper limits at $\omega\gamma \sim 10^{-10}$ eV already predict a very low yield for the detection of the resonances.

The present uncertainties for the reaction rate of ^{22}Ne(p,γ)^{23}Na have a strong influence on the understanding of the neon-sodium cycle, which is assumed to take place at a temperature of $T = 0.1 - 0.5$ GK. Consequently, the improvement of the reaction rate by future measurements will have a strong impact on the calculation of astrophysical processes involving the neon-sodium cycle.

6.4. Non-Resonant Contribution

Based on the LUNA data, the S-factor $\tilde{S}^{440}$ has been calculated for the proton energy at $E_p^{lab} = 360\,\text{keV}$ with the yield of the $E_\gamma = 440\,\text{keV}$ peak. This peak also includes unknown contributions from higher level cascades next to DC → 440.

The cross-section component for the 440 → 0 transition obtained at LUNA can be compared with the results of Rolfs et al. [36] for DC → 440. Figure 6.4 shows a fit of the cross-section for the non-resonant DC → 440 process and the contribution of the DC → 2391 process to the 440 → 0 counting rate (through the assumed ∼ 33% branching of 2391 → 440) [36]. Additionally, the S-factor calculation based on the LUNA data has been inserted.

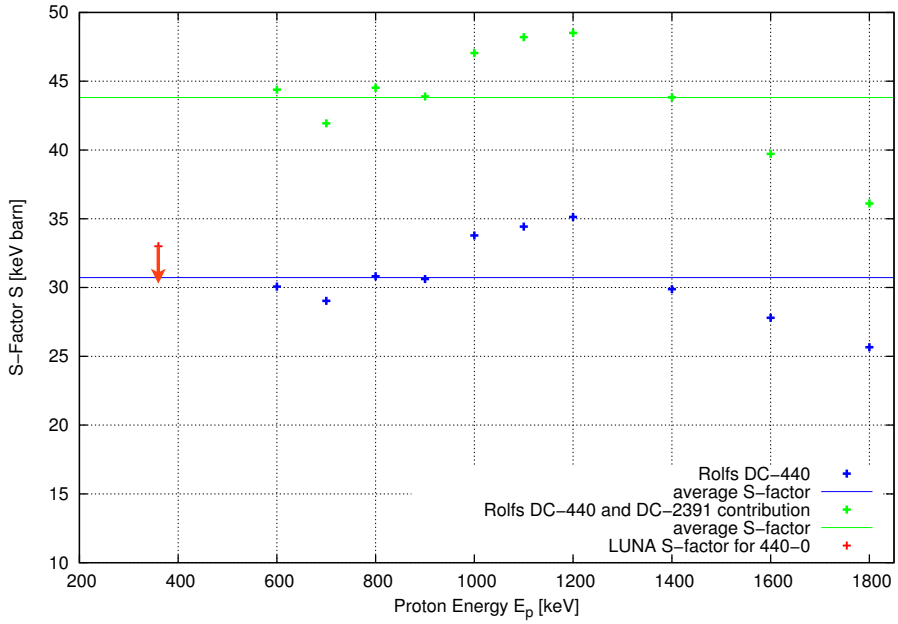

Figure 6.4.: Cross-section curve for DC → 440, contributions of DC → 2391 from [36] and cross-section values measured by LUNA.

The results for the S-factors are extracted in Table 6.3.

Experiment	Direct Capture Process	S-Factor
Rolfs	DC→440	31 keV barn
Rolfs	DC→440 + DC→2391 (33%)	44 keV barn
LUNA	DC→440 + unkown contribution	≤ 33 keV barn

Table 6.3.: S-factors for DC→440 determined by Rolfs et al. [36] and LUNA.

One can see, that this new upper limit from LUNA with $S \leq 33\,\text{keV barn}$ is lower than sum of the S-factor contribution of DC-440 and DC-2391 stated by [37].

6.5. Evaluation of Errors

During the data taking and the data analysis at LUNA II, multiple factors contributed to the errors of the final results. In the following, the most dominant sources of errors and possible solution are presented.

6.5.1. LUNA-Setup

The beam energy at LUNA has been calibrated with the ^{12}C(p,γ)^{23}Na-reaction. This reaction has a Q-value error of 0.3 keV which has a major influence on the error of the beam energy. A better determination of the Q-value would improve this beam energy error.

The pressure in the collimator between target chamber and the first pumping stage decreases in a way which is hard to measure. Therefore an effective length is assumed for the collimator to implement the effect of the pressure reduction. This effective length is assumed to have an error of 20%, which might difficult to be reduced by detailed pressure measurements without changing the pressure profile.

For the temperature in the target a value of $T = (308 \pm 15)$ K has been assumed. With a temperature sensors inside the target chamber, the relative error of 5% might be reduced.

6.5.2. Target Gas

The target gas from Linde is assumed to have a fraction of neon isotopes corresponds to the natural variation. This leads to an error of 8% for the fraction of the target isotope ^{22}Ne and has an direct impact on the effective stopping power ϵ_{eff} in the target gas. An analysis of the target gas by mass-spectroscopy should be strongly considered.

6.5.3. Beam-Heating

One of the most dominant errors is caused by the beam heating temperature. Based on [29], an error of 40% has to be assumed. The reduction of this error should be in center of research during the future beam heating studies at LUNA. The error of the beam heating as a strong impact on the position of interaction inside the target chamber and consequently also on the error of the detector efficiency.

6.5.4. Resonance Energy

The resonance energies taken from [8] have an error of $1 - 3$ keV which has an impact on the uncertainties of i.e. the resonance strength. Precise measurements with small energy steps should render more precisely the correct energy and error of the resonance.

6.5.5. Spectral Analysis

The γ-ray spectra show a strong beam-induced background for high energetic resonances. This background is caused by impurities in the gas, as well as oil from the pumps and implanted ions in the target wall. Changes in the setup should reduce this background components.

For the determination of higher energetic γ-transitions, the statistics could be optimized in rising the time of measurement. For this procedure, a balance between the amount of runs and the statistic of the spectra has to be needed.

A. Appendix

A.1. Spectra of ^{22}Ne(p,γ)^{23}Na Resonances

In the following attached figures, the complete spectra for the resonant runs at $E_{res}^{lab} = 159, 186, 256, 323, 334\,\text{keV}$ and the non-resonant run at $E_p^{lab} = 360\,\text{keV}$ in the energy range of $E_\gamma = 0-8000\,\text{keV}$ are displayed. The γ-ray transitions introduced in paragraph 5.1.1 are highlighted. Furthermore the beam-induced background (see paragraph 4.2.2) is marked. The peaks from the laboratory background have to be taken from Figure 4.3. The abbreviation SE stands for single escape.
Figure A.7 shows the spectrum of the resonant run $E_{res}^{lab} = 159\,\text{keV}$ with the region of interest centered at $E_\gamma = 1636\,\text{keV}$.

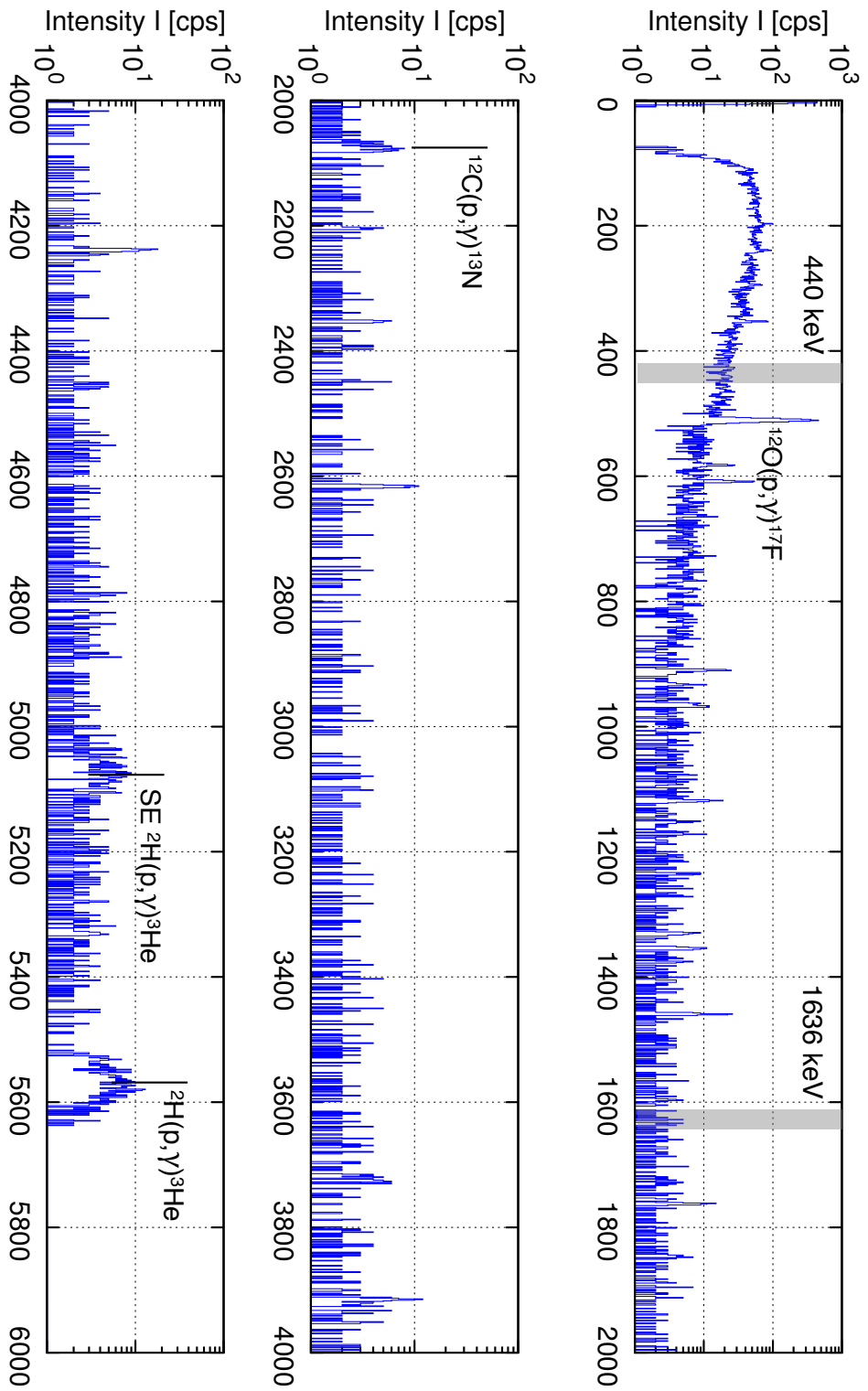

Figure A.1.: γ-ray spectrum of the resonance at $E_{res}^{lab} = 159\,\mathrm{keV}$ populated by $E_p^{lab} = 162\,\mathrm{keV}$.

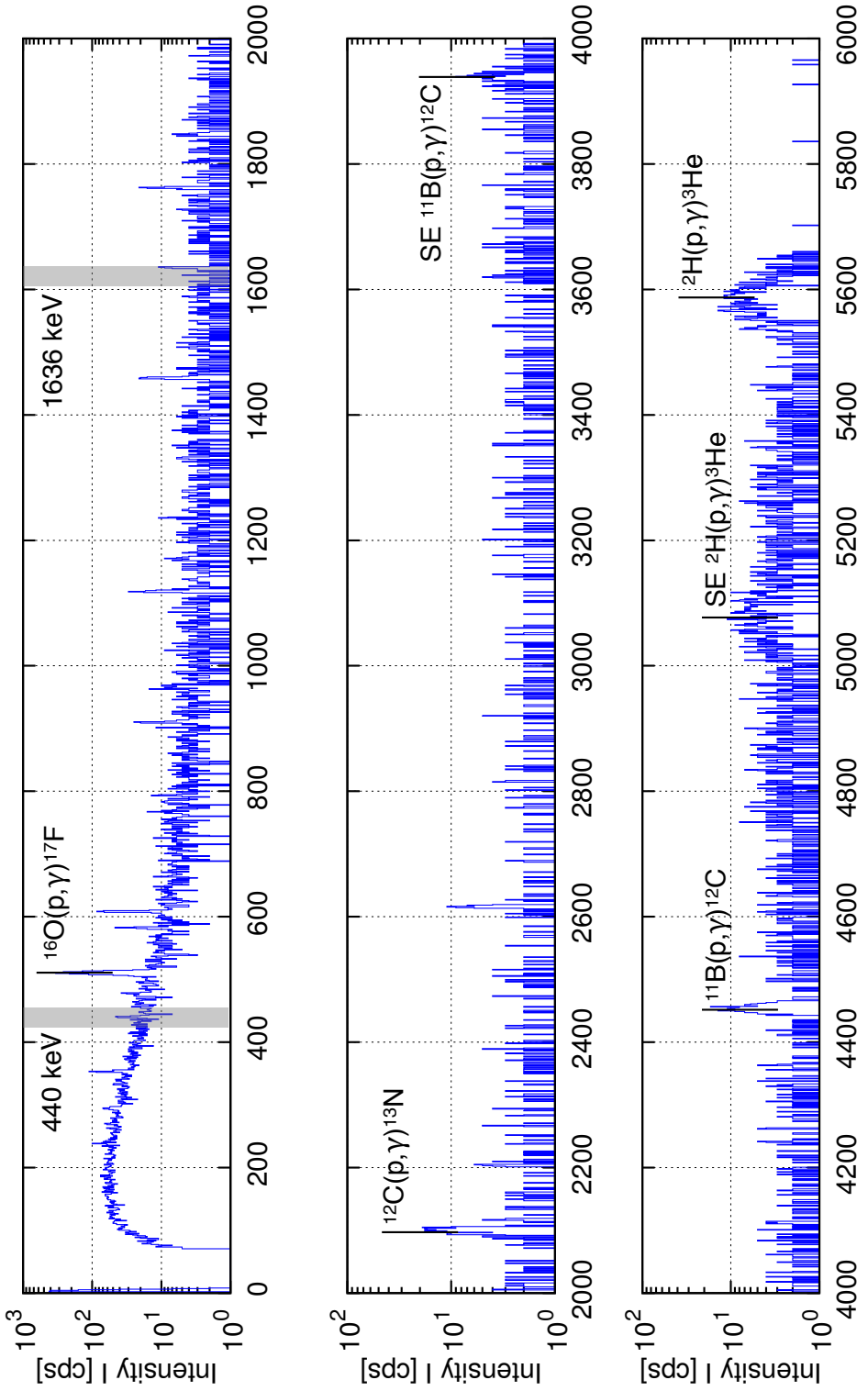

Figure A.2.: γ-ray spectrum of the resonance at $E_{res}^{lab} = 186\,\mathrm{keV}$ populated by $E_p^{lab} = 191\,\mathrm{keV}$.

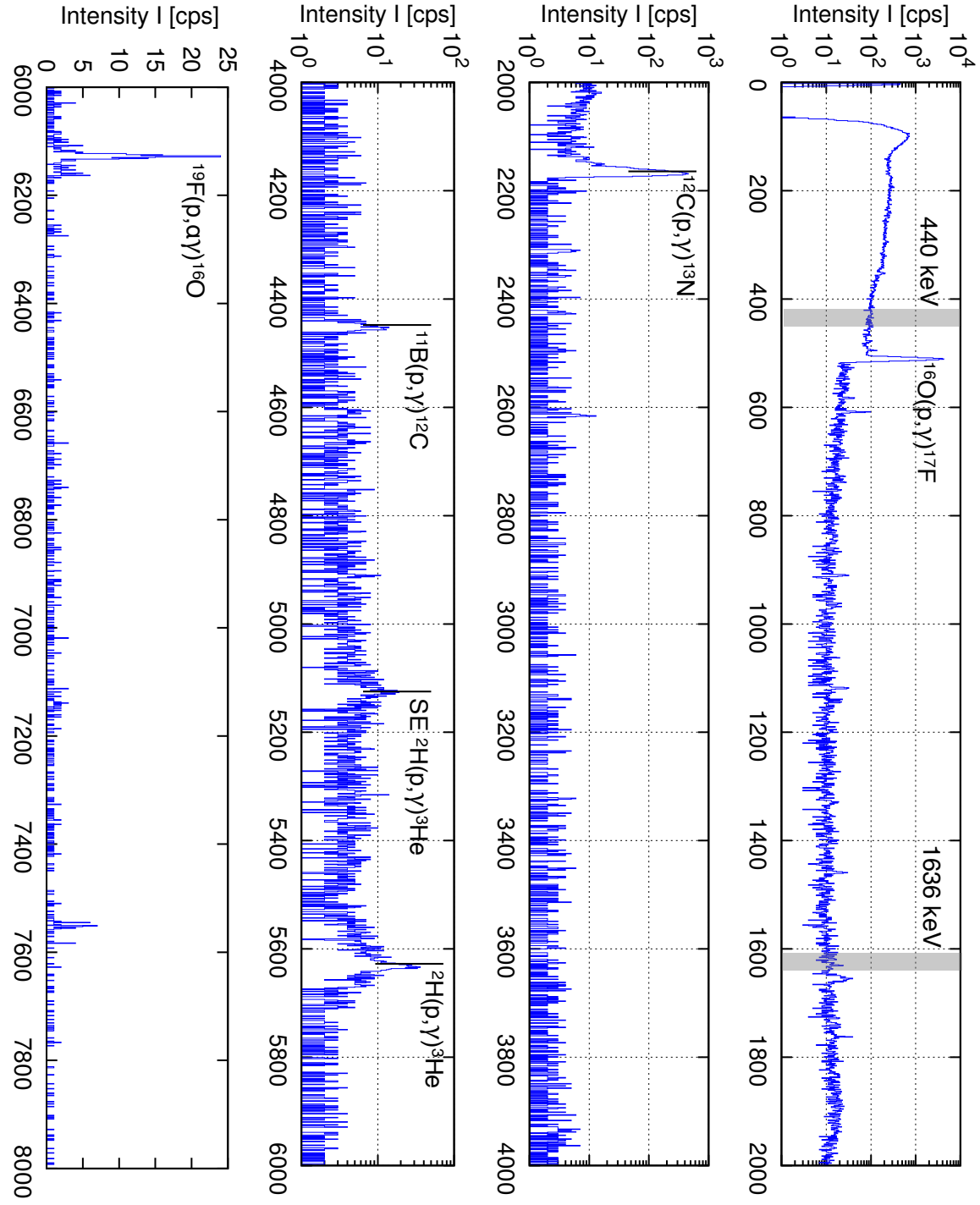

Figure A.3.: γ-ray spectrum of the resonance at $E_{res}^{lab} = 256\,\mathrm{keV}$ populated by $E_p^{lab} = 258\,\mathrm{keV}$.

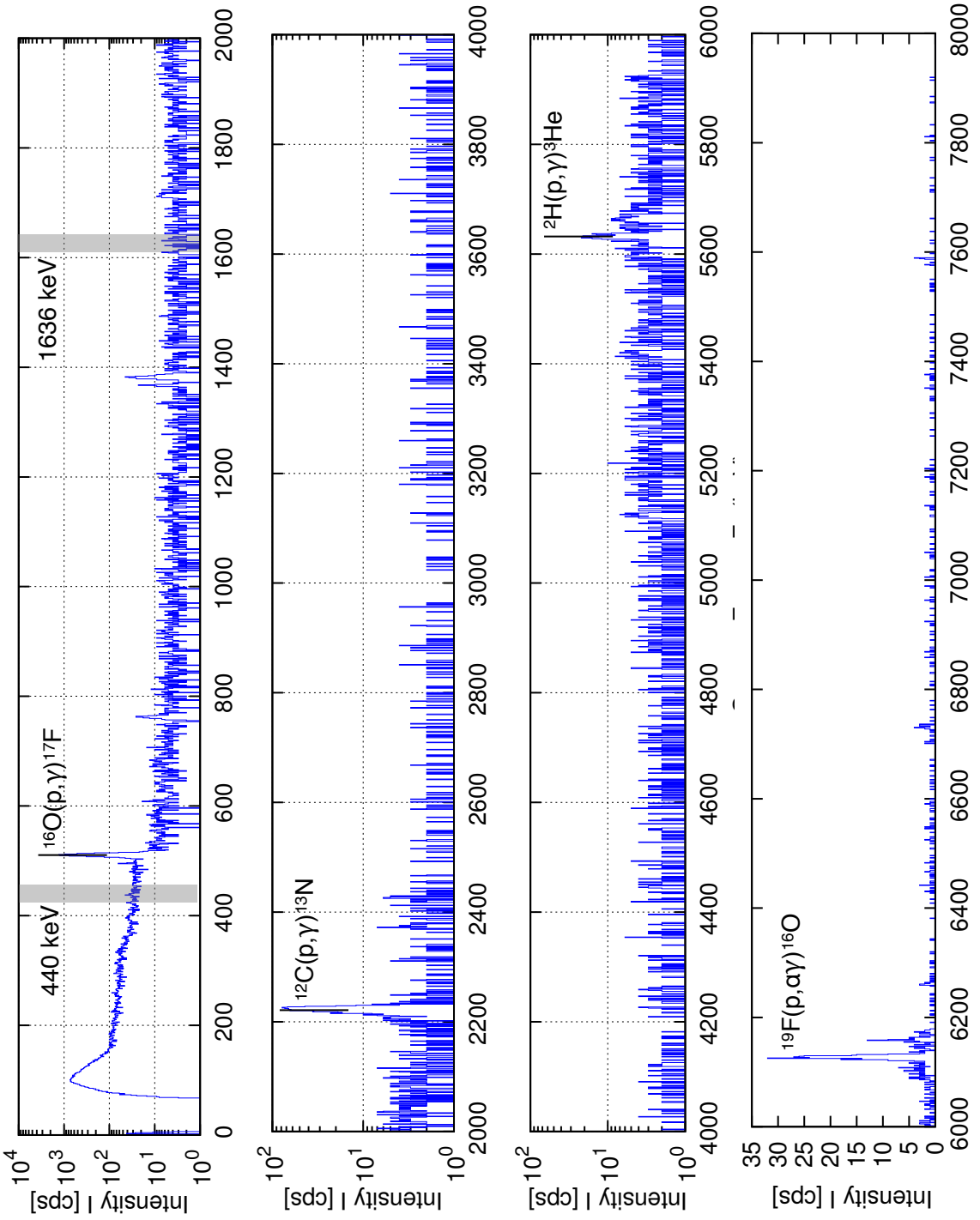

Figure A.4.: γ-ray spectrum of the resonance at $E_{res}^{lab} = 323\,\mathrm{keV}$ populated by $E_p^{lab} = 330\,\mathrm{keV}$.

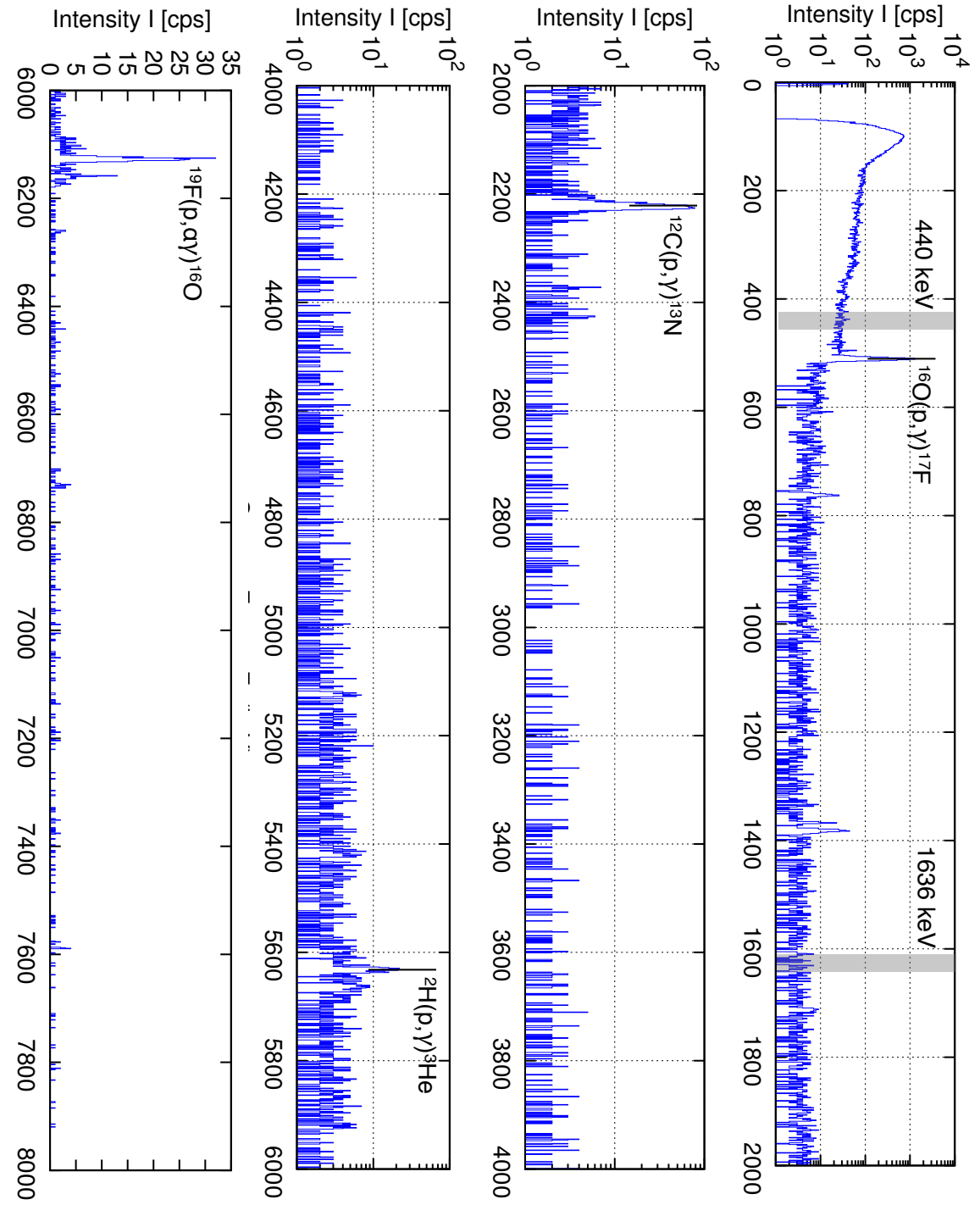

Figure A.5.: γ-ray spectrum of the resonance at $E_{res}^{lab} = 334\,\mathrm{keV}$ populated by $E_p^{lab} = 339\,\mathrm{keV}$.

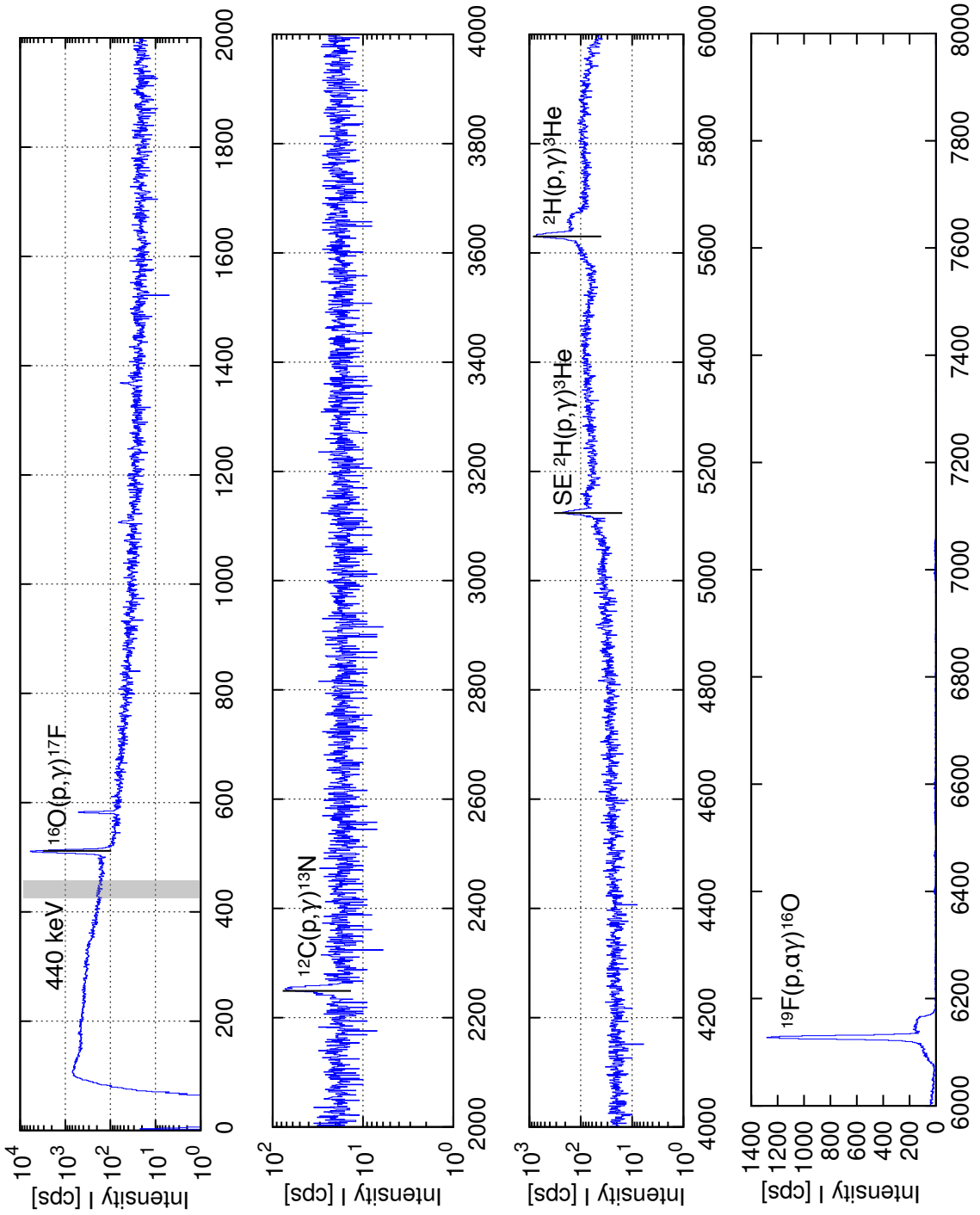

Figure A.6.: γ-ray spectrum of the non-resonant run $E_p^{lab} = 360$ keV.

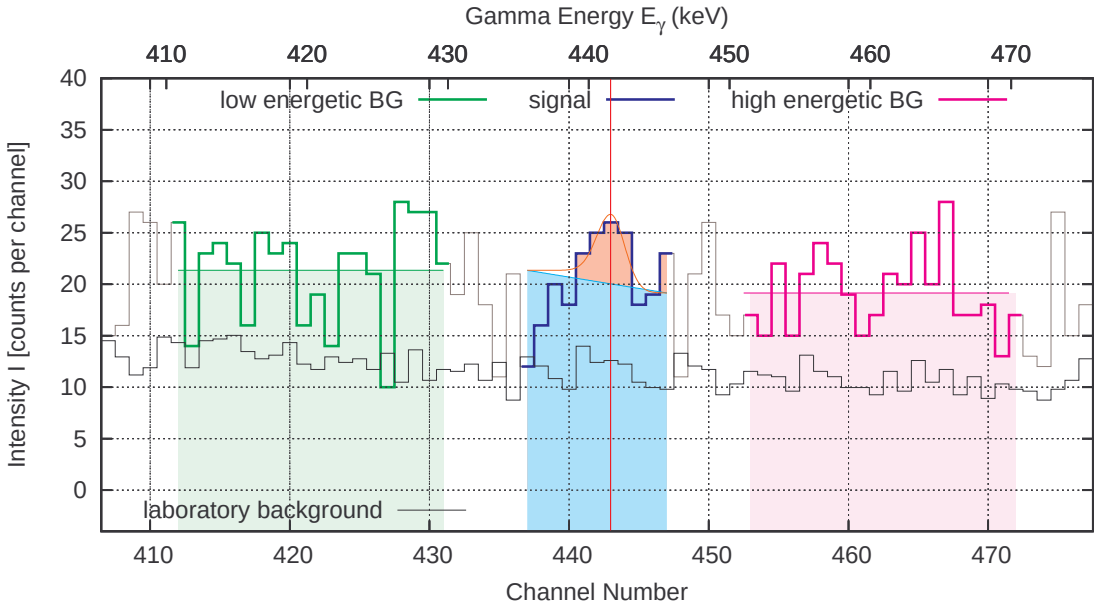

Figure A.7.: γ-spectrum of $E_{res}^{lab} = 159\,\mathrm{keV}$ with ROI centered at $E_\gamma = 1636\,\mathrm{keV}$.

A.2. Beam Heating Setup

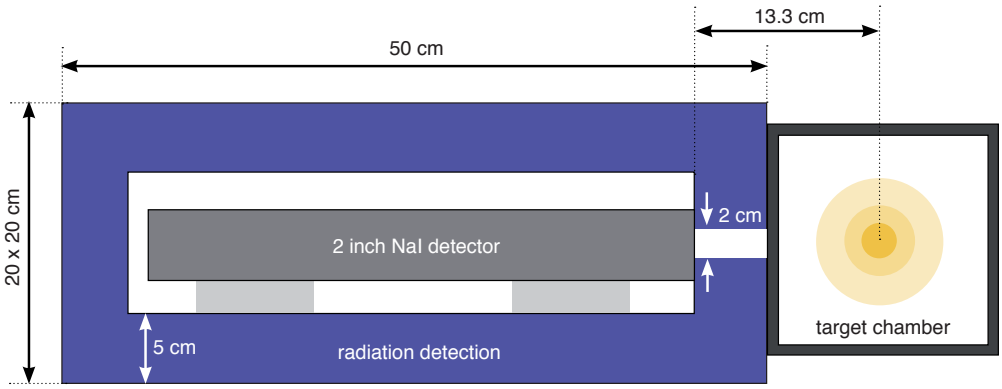

Figure A.8.: Beam Heating Setup at LUNA.

Bibliography

[1] Atomic Weights of the Elements: Review 2000 (IUPAC Technical Report). *Pure and Applied Chemistry*, 75(6):683–800, 2003.

[2] ENSDF. Evaluated Nuclear Structure Data File. ie.lbl.gov/databases/ensdfserve.html. 2006.

[3] M. Anders et al. Neutron flux induced by an α-beam incident on a deuterium gas target as a background for the study of the ^{2}H$(\alpha,\gamma)^{6}$Li reaction at LUNA. *The European Physical Journal A*, submitted.

[4] C. Angulo, M. Arnould, M. Rayet, et al. A compilation of charged-particle induced thermonuclear reaction rates. *Nuclear Physics A*, 656(1):3 – 183, 1999.

[5] G. Audi, A.H. Wapstra, and C. Thibault. The AME2003 atomic mass evaluation: (II). Tables, graphs and references. *Nuclear Physics A*, 729(1):337 – 676, 2003. The 2003 NUBASE and Atomic Mass Evaluations.

[6] R.B. Firestone. Nuclear Data Sheets for A = 21. *Nuclear Data Sheets*, 103(2):269 – 324, 2004. .

[7] R.B. Firestone. Nuclear Data Sheets for A = 22. *Nuclear Data Sheets*, 106(1):1 – 88, 2005.

[8] R.B. Firestone. Nuclear Data Sheets for A = 23. *Nuclear Data Sheets*, 108(1):1 – 78, 2007.

[9] A. Formicola, G. Imbriani, et al. The LUNA II 400kV accelerator. *Nuclear Instruments and Methods in Physics Research Section A: Accelerators, Spectrometers, Detectors and Associated Equipment*, 507(3):609 – 616, 2003.

[10] G. Gilmore. Practical Gamma-ray Spectrometry. *John Wiley & Sons Ltd*, 2008.

[11] J. Görres, H.W. Becker, L. Buchmann, C. Rolfs, P. Schmalbrock, H.P. Trautvetter, A. Vlieks, J.W. Hammer, and T.R. Donoghue. Proton-induced direct capture on ^{21}Ne and ^{22}Ne. *Nuclear Physics A*, 408(2):372 – 396, 1983.

[12] J. Görres, K.U. Kettner, H. Kräwinkel, and C. Rolfs. The influence of intense ion beams on gas target densities. *Nuclear Instruments and Methods*, 177(2-3):295 – 303, 1980.

[13] J. Görres, C. Rolfs, P. Schmalbrock, H.P. Trautvetter, and J. Keinonen. Search for low-energy resonances in ^{21}Ne(p,γ)^{22}Na and ^{22}Ne(p,γ)^{23}Na. *Nuclear Physics A*, 385(1):57 – 75, 1982.

[14] S. E. Hale, A. E. Champagne, C. Iliadis, V. Y. Hansper, D. C. Powell, and J. C. Blackmon. Investigation of the ^{22}Ne(p,γ)^{23}Na reaction via (^{3}He, d) spectroscopy. *Physical Review C*, 65:015801, Dec 2001.

[15] W. Hietzke. Influence of parity-dependent nuclear level densities on astrophysical reactions. *PhD Thesis, California State University, cited according to NACRE*, 1975.

[16] C. Iliadis. *Nuclear Physics of Stars.* 2007.

[17] C. Iliadis, R. Longland, A.E. Champagne, and A. Coc. Charged-particle thermonuclear reaction rates: III. Nuclear physics input. *Nuclear Physics A*, 841(1-4):251 – 322, 2010. The 2010 Evaluation of Monte Carlo based Thermonuclear Reaction Rates.

[18] C. Iliadis, R. Longland, A.E. Champagne, A. Coc, and R. Fitzgerald. Charged-particle thermonuclear reaction rates: II. Tables and graphs of reaction rates and probability density functions. *Nuclear Physics A*, 841(1-4):31 – 250, 2010. The 2010 Evaluation of Monte Carlo based Thermonuclear Reaction Rates.

[19] C. Iliadis and A. Sallaska. Nucleosynthesis Calculator. *http://starlib.physics.unc.edu/*, 2012.

[20] J. José and M. Hernanz and C. Iliadis. Nucleosynthesis in classical novae. *Nuclear Physics A*, 777(0):550 – 578, 2006. Special Issue on Nuclear Astrophysics.

[21] Jordi José, Margarita Hernanz, Enrique Garcia-Berro, and Pilar Gil-Pons. The Impact of the Chemical Stratification of White Dwarfs on the Classification of Classical Novae. *The Astrophysical Journal Letters*, 597(1):L41, 2003.

[22] A.S. Kachan, I.S. Kovtunenko, I.V. Kurguz, V.M. Mishchenko, and R.P. Slabospitsky. Resonance-like structure observed in ^{22}Ne(p, γ)^{23}Na reaction. *Izvestiâ Akademii nauk UdSSR. Seriâ fiziceskaâ*, 70(5):751–756, 2006.

[23] G. F. Knoll. *Radiation Detection and Measurement.* 2010.

[24] H. Kuchling. Taschenbuch der Physik. *Fachbuchverlag Leipzig*, 1991.

[25] K. Lodders. Solar System Abundances and Condensation Temperatures of the Elements. *The Astrophysical Journal*, 591(2):1220, 2003.

[26] H. P. Loens. Influence of parity-dependent nuclear level densities on astrophysical reactions. *Diploma Thesis, TU Darmstadt*, 2007.

[27] R. Longland, C. Iliadis, J. M. Cesaratto, A. E. Champagne, S. Daigle, J. R. Newton, and R. Fitzgerald. Resonance strength in ^{23}Na from the ^{22}Ne(p, γ)^{23}Na from depth profiling in aluminum. *Phys. Rev. C*, 81:055804, May 2010.

[28] R. Longland, C. Iliadis, A.E. Champagne, J.R. Newton, C. Ugalde, A. Coc, and R. Fitzgerald. Charged-particle thermonuclear reaction rates: I. Monte Carlo method and statistical distributions. *Nuclear Physics A*, 841(1-4):1 – 30, 2010. The 2010 Evaluation of Monte Carlo based Thermonuclear Reaction Rates.

[29] M. Marta et al. Study of beam heating effect in a gas target through Rutherford scattering. *Nuclear Instruments and Methods in Physics Research Section A: Accelerators, Spectrometers, Detectors and Associated Equipment*, 569(3):727 – 731, 2006.

[30] B. Meyer. sourceforge.net/u/mbrandle/nlog/. 2012.

[31] M.A. Meyer and J.J.A. Smit. The energy levels of ^{23}Na. *Nuclear Physics A*, 205(1):177 – 192, 1973.

[32] J.L. Osborne, C.A. Barnes, and others. Low-energy behavior of the $^{3}\mathrm{He}(\alpha,\gamma)^{7}\mathrm{Be}$ cross section. *Nuclear Physics A*, 419(1):115 – 132, 1984.

[33] M. Piiparinen, A. Anttila, and M. Viitasalo. A study of the excited states of ^{23}Na from the $^{22}\mathrm{Ne}(\mathrm{p},\gamma)^{23}\mathrm{Na}$ reaction. *Zeitschrift für Physik*, 247(5):400–407, 1971.

[34] A. M. Amthor R. H. Cyburt and others. The JINA REACLIB Database: Its Recent Updates and Impact on Type-I X-ray Bursts. *The Astrophysical Journal Supplement Series*, 189(1):240, 2010.

[35] C. Ritossa, E. Garcia-Berro, and Jr. I. Iben. On the Evolution of Stars That Form Electron-degenerate Cores Processed by Carbon Burning. II. Isotope Abundances and Thermal Pulses in a 10 M_{sun} Model with an ONe Core and Applications to Long-Period Variables, Classical Novae, and Accretion-induced Collapse. *Astrophysical Journal*, 460:489, March 1996.

[36] C. Rolfs, W.S. Rodney, Winkel. H., and M.H. Shapiro. Hydrogen burning of ^{20}Ne and ^{22}Ne in stars. *Nuclear Physics A*, 241(3):460–486, 1975.

[37] C. E. Rolfs and W.S. Rodney. *Cauldrons in the Cosmos.* 1988.

[38] W. M. Sparks S. Starrfield and J. W. Truran. Hydrodynamic models for novae with ejecta rich in oxygen, neon, and magnesium. *Astrophysical Journal Letters*, 303:L5–L9, 1986.

[39] S. Starrfield S. Sumner and others. The Effects of New Nuclear Reaction Rates and Opacities on Hydrodynamic Simulations of the Nova Outburst. *The Astrophysical Journal Supplement Series*, 127:485, 2000.

[40] J.J.A. Smit, M.A. Meyer, J.P.L. Reinecke, and D. Reitmann. A study of the ^{23}Na from the $^{22}\mathrm{Ne}(\mathrm{p},\gamma)^{23}\mathrm{Na}$ reaction in the energy region E_p = 1.1 to 2.0 MeV. *Nuclear Physics A*, 318(1-2):111 – 124, 1979.

[41] Z.B. Toit, P.R. Kock, J.H. Hough, and W.L. Mouton. Resonant absorption of the γ-radiation from the ^{23}Na from the $^{22}\mathrm{Ne}(\mathrm{p},\gamma)^{23}\mathrm{Na}$ reaction and the effect of rutherford scattering in the target on the width of the absorption curves. *Zeitschrift für Physik*, 255:97–102, 1972.

[42] Z.B. Toit, P.R. Kock, and W.L. Mouton. Resonance strengths, branching ratios and mean lifetimes of nuclear energy levels in ^{23}Na. *Zeitschrift für Physik*, 246:170–182, 1971.

[43] J. F. Ziegler. SRIM. The Stopping and Range of Ions in Matter. www.SRIM.org. 2008.

Declaration of authorship

"I, Marie-Luise Menzel, hereby declare:

that I have written this thesis without any help from others and without the use of documents and aids other than those stated above,

that I have mentioned all used sources and that I have cited them correctly according to established academic citation rules,

that this thesis in the present or any similar form has not been submitted at any other university in Germany or abroad."

Eigenständigkeitserklärung

"Hiermit versichere ich, Marie-Luise Menzel,

dass ich die vorliegende Arbeit ohne unzulässige Hilfe Dritter und ohne Benutzung anderer als der angegebenen Hilfsmittel angefertigt habe.

Die aus fremden Quellen direkt oder indirekt übernommenen Gedanken sind als solche kenntlich gemacht.

Die Arbeit wurde bisher weder im Inland noch im Ausland in gleicher oder ähnlicher Form einer anderen Prüfungsbehörde vorgelegt."

Acknowledgements

The journey is the reward.

In my opinion, human relations have at least the same values as scientific results. This is why I would like to take the opportunity to thank a lot of people I was sharing the time with during my diploma thesis.

In first place, I thank PD Dr. Daniel Bemmerer who was the supervisor of my diploma project and who offered me to work with the LUNA collaboration for the ^{22}Ne(p,γ)^{23}Na project. It was a great chance to work with the Italian-German collaboration and Daniel did a good job in getting me comfortable with all the mysteries of LUNA. He also encouraged me to enter new fields in accelerator and detector physics and supported my interests in theoretical astrophysics at GSI. For sure, I will remember for long time the funny group dinners in various Italian restaurants all over Assergi.

Next to Daniel, I would like to thank Prof Kai Zuber. We both share a great passion for astrophysics and it is always a pleasure to speak with him about the universe. He is really great in answering scientific questions, but I also also cherish him a lot as a mentor. I hope that we will continue our great universe-related coffee-breaks in future.

In the following, I want to say thanks to the LUNA group, in special to Francesca Cavanna and Rosanna Depalo I was working with. We spent several shifts and video-conferences together and I appreciated your unhesitating and dedicated returns to my questions as well as the working atmosphere. I wish you best luck and a lot of success in your future with our neon isotopes.

For the implementation of the new resonances in the thermonuclear reaction rate, Prof Christian Iliadis and Anne Sallaska from University of North Carolina at Chapel Hill permit to use their Nucleosynthesis Simulator. This was a very helpful tool to analyze the impact of our measurements in comparison to former studies.

Zoltan Elekes helped me a lot in getting introduced in the Geant4-routine of the LUNA experiment. Thanks a lot for that support.

Most of the diploma time, I spent at the Helmholtz-Zentrum Dresden-Rossendorf. During all that time, Konrad Schmidt was one of the best office mates I have ever met before. He was extremely helpful regarding my thousands of questions at the beginning (I just say ‘gnuplot‘ and ’spectral analysis’). He is a great optimist and I was really astonished about your talent for magic tricks! Another person, I thank is Michael Anders. We spent a lot

of time together talking about science and faithfully sharing opinions about the ups and downs of our work. Thank you very much for your support and the always encouraging smile! I wish you both having a successful PhD-time in Dresden.

The best introduction in the mechanical workshop ever, has been done by Andreas Hartmann. His patience is infinite and he is excellent in explaining and answering my questions. He was very, very helpful in fulfilling our wishes for new equipment at LUNA.

What would be the Institute for Radiation Physics without Andreas Wagner, Roland Schwengner, Arnd Junghans and the director Prof Thomas Cowan? I would like to thank for your support and interest in my research. A lot of students have been a big enrichment next to the work: Tobias Reinhardt, Mirco Dietz, Roland Hannaske, Marko Röder, Louis Wagner, Toni Kögler, Maik Butterling, Ralf Massaczyk, Stefan Reinicke and many more. In this place I would also thank my proof-reading team: including Jeremy Miles Johnson, who was so kind to make comments on my English in the diploma thesis and decorated the draft with several encouraging smilies and sketches. Furthermore, Falk Wunderlich who was really accurately in correcting the report.

During the diploma thesis, I spent two months as a summer student as GSI. Joern Knoll strongly supported me in joining the program and I had a big pleasure in working with the theory group of Gabriel Martinez-Piñedo. He and Lutz Huther introduced me in the nuclear network analysis and helped me in getting results for the neon-sodium-cycle in novae. I felt very comfortable in this research group and would like to thank again the entire group for welcoming me.

At the final period of my diploma thesis, I was looking for a perfect place to write down my results. Prof Kämpfer has been so kind to offer me a great working place in the theory department at the Technical University. It was a very nice gesture, I highly appreciated.

Looking in the past, it just seems like yesterday, that I started studying physics. I remember when I got infected by the enthusiasm about high energy physics of Prof Michael Kobel during one of his master classes during High School. Now, six years later, a great study time of physics has just passed extremely fast. I met so many awesome people and gained experiences, I am really grateful for.

All this work would not have been possible with the great support I got from my family. They are incredibly precious to me and I enjoy having them around. They always supported me very strongly during my studies and helped me in making all my big projects possible. I thank you with all my heart!